TRMM σ^o VEGETATION SIGNATURES AND OTHER STUDIES

by

James E.H. Dyal

A thesis submitted to the faculty of

Brigham Young University

in partial fulfillment of the requirements for the degree of

Master of Science

Department of Electrical and Computer Engineering

Brigham Young University

December 1999

BRIGHAM YOUNG UNIVERSITY

GRADUATE COMMITTEE APPROVAL

of a thesis submitted by

James E.H. Dyal

This thesis has been read by each member of the following graduate committee and by majority vote has been found to be satisfactory.

_____   _____
Date   Dr. David Long, Chair

_____   _____
Date   Dr. Brian Jeffs

_____   _____
Date   Dr. Mike Jensen

As chair of the candidate's graduate committee, I have read the thesis of James E.H. Dyal in its final form and have found that (1) its format, citations, and bibliographical style are consistent and acceptable and fulfill university and department style requirements; (2) its illustrative materials including figures, tables, and charts are in place; and (3) the final manuscript is satisfactory to the graduate committee and is ready for submission to the university library.

_____   _____
Date   Dr. David Long
                            Chair, Graduate Committee

Accepted for the Department

                            _____
                            Lee Swindlehurst
                            Graduate Coordinator

Accepted for the College

                            _____
                            Douglas M. Chabries
                            Dean, College of Engineering and Technology

ABSTRACT

TRMM σ^o VEGETATION SIGNATURES AND OTHER STUDIES

James E.H. Dyal

Department of Electrical and Computer Engineering

Master of Science

In November of 1997, the Tropical Rain Mapping Mission(TRMM) was launched with the intent of monitoring rainfall over the worlds equatorial regions. TRMM Precipitation Radar (TRMM PR) is one of five instruments on board the TRMM platform and operates much like a scatterometer. Although TRMM PR was designed to create three dimensional images of rainfall, TRMM PR also collects backscatter measurements from the surface of the earth. TRMM PR is different from a traditional scatterometer not only in the purpose of its design, but also in the incidence angle range it operates within. While scatterometers designed for wind retrieval operate in incidence angles above 20°, TRMM PR operates between nadir and 17°. This thesis is an application of TRMM PR data to land studies and an analysis of the relationship of Ku-band backscatter at low incidence angles with different tropical vegetation types.

In order to complete many of the vegetation studies in this thesis, it is necessary to optimize the Scatterometer Image Reconstruction with Filtering algorithm for use with TRMM PR data. As TRMM PR data has a relatively high nominal resolution,

optimized SIRF is able to improve resolution to 1.2 km. With the TRMM PR SIRF images, is it possible to make accurate vegetation and land studies.

Using TRMM SIRF images and raw TRMM PR 2A21 processed data, many different vegetation and land based studies are possible. In order to compare the TRMM PR data with NASA Scatterometer (NSCAT) data, various SIRF parameters are compared for different vegetation types. NSCAT and TRMM PR are complementary instruments, operating at the same frequency but each using a completely different incidence angle range. TRMM PR data was found to be less sensitive than NSCAT data to vegetation type. TRMM PR data is also used to analyze the σ^o/incidence angle relationship for different vegetation types, as well as the dependence of σ^o on the local time of day. These studies are a fascinating example of volume and surface scattering theory. Results are discussed for areas of similar vegetation type but different moisture content.

TRMM PR SIRF is also used to evaluate short-term urban growth. Several of the largest cities in Brazil are chosen and using TRMM PR data, SIRF images are created for April, 1998 and April, 1999. The observed differences of each city are compared with a control difference image in order to evaluate the validity of the observed difference. Although changes in the city can be detected using TRMM SIRF, the results are less than reliable due to the noisy TRMM PR σ^o measurements.

Contents

x

List of Tables

List of Figures

Chapter 1

Introduction

In November of 1997, the Tropical Rain Mapping Mission(TRMM) was launched with the intent of monitoring rainfall over the worlds equatorial regions. On board TRMM, the TRMM Precipitation Radar (TRMM PR) was designed much like modern scatterometers but uses a different incidence angle than what is effective for wind retrieval; the primary design objective of most scatterometers. Given the recent usage of scatterometers for land and vegetation studies, TRMM PR provides an excellent tool for obtaining a more complete understanding of radar interaction with different tropical vegetation types.

1.1 Motivation

The study of vegetation over the earth, especially over the equatorial regions, is important to global weather and climate models. Areas such as the vast equatorial rain forests greatly affect the weather in the tropics, the amount of moisture in the air, and the amount of oxygen produced. These factors have an effect on the global climate and weather models. For the purpose of studying the weather on a global level, many spaceborne satellites have been constructed to observe the earth. Scatterometers are of this group of satellites and were designed to study wind patterns over the oceans. Recently however, data collected by scatterometers has been used with resolution enhancement techniques for land and vegetation studies [1] [2] [3] [4]. Scatterometers are ideal for studies of this kind because they are relatively insensitive to cloud cover and precipitation and their rapid repeat coverage allows large scale phenomena to be observed on a global scale.

The first spaceborne scatterometer (SASS) was launched in 1978 aboard the remote sensing satellite Seasat. Although a power failure 90 days into the mission prevented the scatterometer from collecting enough data to make serious vegetation studies, enough was collected to verify that scatterometers were useful in land studies [3] [5]. In 1991 and 1995, the European Space Agency sponsored two fan beam scatterometers on board the remote sensing satellites ERS1 and ERS2. NASA Scatterometer (NSCAT) was launched in 1996 aboard the the Japanese spacecraft ADEOS. Before the NSCAT mission was cut short by a solar panel failure nine months into its mission, enough NSCAT data was collected to make a serious attempt at vegetation studies [2]. One of the factors that made NSCAT data so attractive to vegetation studies was NSCAT's higher nominal resolution when compared to older scatterometers.

The Tropical Rain Mapping Mission (TRMM) was launched in the November of 1997 as a joint mission between NASA and the National Space Development Agency (NASDA) of Japan. It was designed to monitor and study rainfall over the tropics. TRMM Precipitation Radar (TRMM PR), one of five instruments on board TRMM, is designed to create 3-D images of tropical rainfall and operates much like a scatterometer. TRMM PR presents some interesting opportunities for vegetation studies due to its higher nominal resolution and different incidence angle range. A vegetation study at such low incidence angles has not been completed prior to the launch of this mission. TRMM PR data allows accurate low incidence angle vegetation σ^o characterization and provides for a more complete understanding of radar interaction with different tropical vegetation types.

1.2 Contributions

The purpose of this thesis is make a complete study of the interaction between tropical vegetation types and low incidence Ku-band radar. This study is to be made using TRMM PR raw data and land images created using an resolution enhancing imaging algorithm known as the Scatterometer Image Reconstruction (SIR) algorithm. Outlined below are the contribution made by this thesis.

The first contribution is an optimization of the SIRF algorithm for use with

TRMM PR data. TRMM PR has the highest nominal resolution of any data set that has been used with the SIRF algorithm, which allows SIRF to reconstruct extremely accurate land images using TRMM data. TRMM PR however, is not a scatterometer, and has a different illumination pattern and much noisier σ^o measurements than prior data sets. For this purpose, SIRF is optimized in order to assure the greatest accuracy possible in the images and consequently the highest possible accuracy in the studies using the images.

The next contribution uses the SIRF algorithm to compare several different parameters over different vegetation types between TRMM PR data and NSCAT data. TRMM PR and NSCAT are complementary instruments as they operate using the same frequency (Ku-band) but totally different incidence angles: NSCAT using the upper incidence angles (20°- 70°) and TRMM PR using the lower angles (0°-17°). The differences in the normalized parameters for different vegetation types also introduce the idea of an instantaneous vegetation classfication algorithm using SIRF.

This thesis also provides an accurate characterization of the low incidence angle relationship between incidence angle and σ^o for different vegetation types. It explores the relationship between surface scattering and volume scattering as a function of canopy density. The results enclosed also provide data on the σ^o/incidence angle relationship for similar vegetation types at different latitudes. These contributions open the possibility to a moisture study using TRMM backscatter measurements.

A time study is completed to show the σ^o dependence on the local time of day at low incidence angle. This study is valuable for scatterometer calibration and interesting for the effects of moisture(dew) on the σ^o measurements.

The last contribution made by this thesis is a study done on urban growth in the tropical regions. This is important to a vegetation study as it shows the replacement of natural landcover with urban development. As a control for the study, the effects of noisy σ^o measurements on SIRF images are examined.

1.3   Overview

This thesis is organized as follows. Chapter 2 provides background on the Tropical Rain Mapping Mission (TRMM) and the TRMM Precipitation Radar (TRMM PR). The Scatterometer Image Reconstruction(SIR) algorithm, which creates resolution enhanced images from radar σ^o measurements, is also described; and a comparison between TRMM PR and scatterometers is given. In order to illustrate this comparison, the NASA Scatterometer (NSCAT) is also described.

Chapter 3 decribes in detail the optimization procedure of the SIRF algorithm for use with TRMM PR 2A21 data. The effect of the size and shape of the illumination area or footprint is considered, and statistical methods are used to determine initialization values and an iteration count from simulation data. The result of this optimization study is an algorithm that is able to enhance the resolution of TRMM PR σ^o images to four times the nominal resolution.

Chapter 4 uses SIRF images over different regions to evaluate normalized σ^o measurements in reference to different tropical vegetation types. This chapter compares the results achieved from this study from NSCAT σ^o measurements to TRMM PR measurements.

Chapter 5 explores the TRMM PR σ^o dependence upon incidence angle for different vegetation types. The difference between volume scattering signatures and surface scattering signatures is described and the conclusions drawn are applied to the TRMM PR study results. Differences in σ^o responses with respect to incidence angle are also compared between regions of different latitude coordinates but similar vegetation type.

Chapter 6 shows the results of a 24-hour time study on TRMM PR σ^o measurements. The TRMM PR σ^o dependence upon incidence angle is evaluated in order to verify if the local time of day affects ku-band low incidence backscatter. Chapter 6 is a continuation of the study documented in chapter 5.

Chapter 7 is an additional study using TRMM PR data that determines whether urban growth can be monitored using data of this type. Using SIRF, some of the larger cities in Brazil were imaged using 1998 data and again using 1999 data.

4

The resulting images from the two different years are compared. The effects of noise in the σ^o measurements on the SIRF images are considered.

Chapter 8 contains a final summary and conclusions along with suggestions for future work.

Chapter 2

Background

This chapter provides a brief introduction to the fundamentals of radar scattering theory and the relationship between landcover and the measurements taken by scatterometers (σ^o). Because this thesis has to do largely with the Tropical Rain Mapping Mission Precipitation Radar (TRMM PR), a brief desription of the function of TRMM PR is also given. The Scatterometer Image Reconstruction with Filtering (SIRF) algorithm, which creates resolution enhanced radar images from σ^o, is described in some detail. Finally a description of the NASA Scatterometer (NSCAT) is given as well as a comparison between a conventional scatterometer and the TRMM PR.

2.1 Overview of Scatterometry

A scatterometer is a radar that measures the scattering or reflective properties of a surface or volume. In order to do this, a scatterometer measures the amount of power that is reflected from a surface or a volume (backscatter) at a specific incidence angle (θ). The scattering property being measured using this definition is the normalized radar cross section (σ^o). The normalized cross section is the ratio of the power returned over the power transmitted. As in all monostatic radar systems, the power returned is governed by the monostatic radar equation. This equation relates the power transmitted, the power recieved and σ^o [6].

$$\sigma^o = \frac{(4\pi)^3 R^4 L P_r}{P_t G^2 \lambda^2 A_{eff}} \tag{2.1}$$

where P_s is the power returned, P_t is the power transmitted, G is the gain of the antenna, λ the wavelength, σ^o the normalized radar backscatter coefficient (or the normalized radar cross section), A the area of the target, and r the distance to the target.

The original intention behind the design of scatterometers was the remote measurement of near surface ocean winds. Scatterometers measure the backscatter from small surface waves called "cats paws" (centimeter scale capillary waves) and thereby determines near surface wind velocity [7]. The power reflected has direct relationship with the roughness of the surface. The greater the magnitude of the wind, the rougher the waves become and the larger the power reflected and the σ^o measurement [6].

Spaceborne scatterometers also collect σ^o measurements over land and the applications of the data collected from different satellites have recently been the focus of many diverse land, ice and vegetation studies. When using σ^o measurements in these terrestrial studies, the scattering phenomena becomes more complex. Factors that affect the measurement include vegetation type and density, soil type and moisture, terrain, the presence and different effects of ice or snow, and many others that are individual to their particular region. For example, the polar regions have a perrenial covering of ice and snow and have a different σ^o than do the desert regions of the Sahara or the tropical rain forests of the Amazon. When evaluating σ^o measurements over different land cover, the measurement is a function of both surface scattering and volume scattering. This phenomena is central to some sections of this thesis and will be discussed in greater detail later.

2.2 Scatterometry in Land and Ice studies

Although scatterometers were designed for ocean wind applications, many valuable land and ice studies have been completed using data collected by scatterometers such as ERS-1, ERS-2 and NSCAT. Examples of such studies include a study of the Canadian Boreal Forests using C-band σ^o measurements collected by ERS-1 [4]. Ice edge detection and ice classification has been achieved over the Arctic and

Antarctic polar regions using NSCAT data (Ku-band) [8] [9]. Using a combination of C-band data and Ku-band data, vegetation classification studies have been completed over the Amazon [2]. Scatterometers have proved useful in studies such as these because of their rapid repeat polar orbit. Scatterometers allow data to be collected on a global scale on a regular cycle.

2.3 Overview of the NASA Scatterometer and the Tropical Rain Mapping Mission Pricipitation Radar

Although NSCAT was designed specifically for ocean wind retrieval, many of the terrestrial studies mentioned earlier were made using NSCAT data. Until Seawinds was launched on Quickscat in June of 1999, NSCAT had been the most advanced scatterometer and had the highest resolution of any spaceborne scatterometer [10]. In comparison, TRMM PR is not a traditional scatterometer. It was designed to measure rainfall, something totally different than what other scatterometers are designed for. TRMM PR does fit the definition for scatterometer given above however, and data collected by this instrument is valuable for land and vegetation studies. TRMM PR will be described in greater detail below.

2.3.1 NSCAT

NASA Scatterometer(NSCAT) aboard the Japanese Advanced Earth Observation Satellite (ADEOS) was designed specifically to measure wind velocity over the ocean surface. NSCAT was launched in August 1996 and produced data from September 1996 to June 1997, when its mission was cut short by a satellite malfunction. NSCAT is dual polarized fan beam scatterometer, which means NSCAT uses 6 3m long slotted waveguide antennas to emit microwave pulses and to recieve the backscatter measurements. Two of these antennas emit both vertically polarized and horizontally polarized radar pulses. Each of these antenna scan a 600km long swath, the net effect of the scatterometer being two 600 km long swaths on either side of the satellite with a nadir coverage gap of 400km. Figure (2.1) shows the antenna and the swath coverage of NSCAT. NSCAT operates at Ku-band (13.995 Ghz) and

measures σ^o from incidence angles between 20°and 70°. NSCAT achieves a nominal resolution of 25 km, which is significantly higher than that of previous scatterometers. Even with the increased resolution, 25km resolution has limited applications in land studies. Resolution enhancement algorithms such as SIRF improve the usefulness of NSCAT data for non-ocean studies. The real advantage of using NSCAT data for land and ice applications is the rapid repeat coverage that NSCAT attains on a global basis. NSCAT has a polar orbit and covers 90% of the earth every two days [10].

2.3.2 TRMM

The Tropical Rain Mapping Mission (TRMM) was launched in October of 1997 with the design of observing precipitation and other regional weather phenomena over the tropics. TRMM is a joint mission between NASA and the National Space Development Agency (NASDA) of Japan. The TRMM Observatory carries five instruments. It includes the first spaceborne Precipitation Radar (PR), the TRMM Microwave Imager (TMI), a Visible and Infrared Scanner (VIRS), a Cloud and Earth Radiant Energy System (CERES - website), and a Lightning Imaging Sensor (LIS). Three of these five instruments (PR,TMI and VIRS) are known as the "rain package" and are used together to overcome the limitations that previous rain study instruments have met and provide greater accuracy than what a single instrument can offer. TRMM has an equatorial orbit ranging from 35°to -35°latitude and flies at an altiude of 350km. TRMM is expected to operate over a mission of three years.

This thesis primarily uses data collected by the TRMM PR. The Precipitation Radar is the first radar specifically designed to measure 3 dimensional rainfall distribution. This instrument has the advantage of being able to measure rainfall most accurately over land, where passive instruments have difficulty. The PR is an electronically scanning radar operating at 13.8 GHz with horizontal polarization. The PR has a nominal resolution at nadir of 4.2 km,the range resolution is 250 m and the scanning swath width is 220 km. Figure (2.2) shows the TRMM PR swath pattern. Because of the similarity of operating frequency, TRMM PR is a complementary instrument to NSCAT. TRMM PR operates at incidence angles between nadir and

10
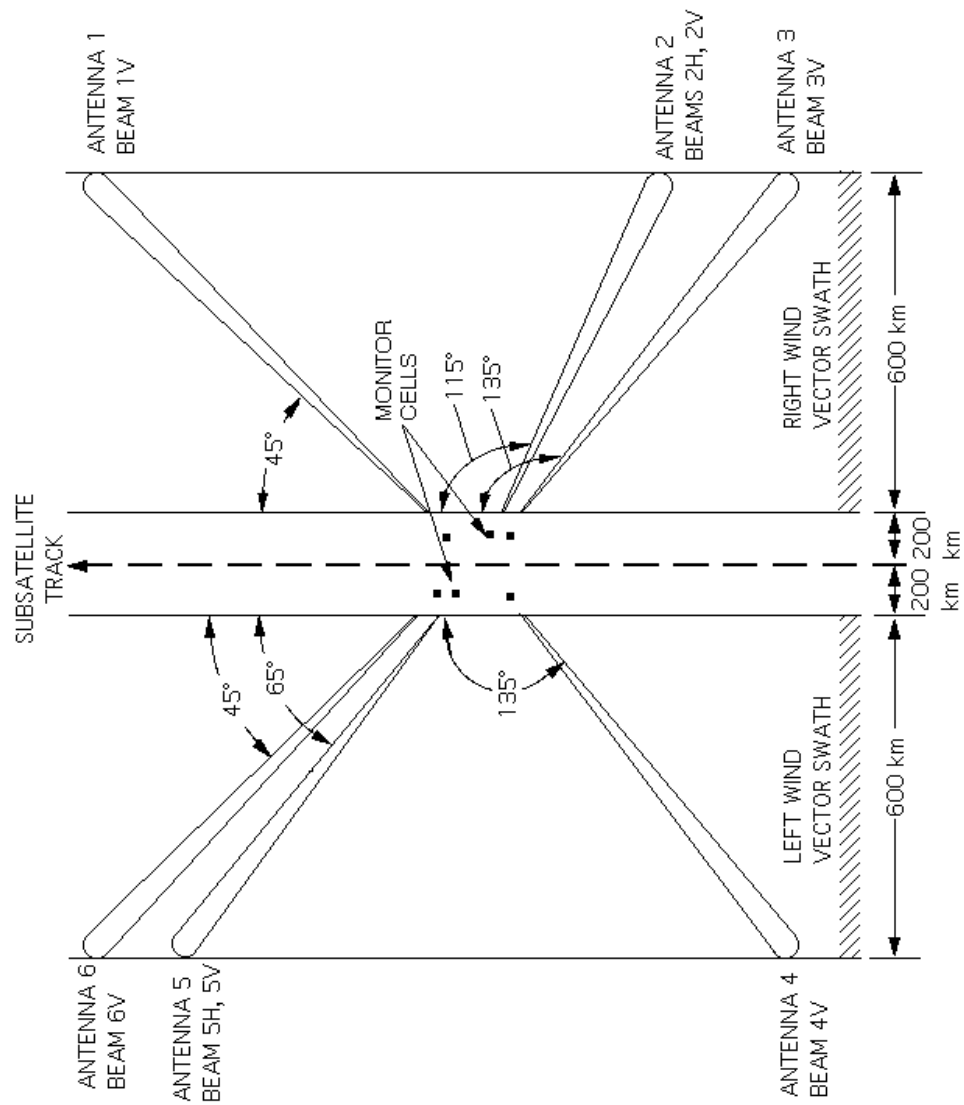
Figure 2.1: The swath pattern of the NASA Scatterometer

17°while NSCAT operates between 20°and 70°. It is this low incidence angle range of TRMM PR that seperates TRMM data from other data collected by previous scatterometers.

The data set provided by TRMM PR can be chosen from several different levels of processing. The data set used to complete the studies in this thesis is the TRMM PR 2A21 data set. The data can be obtained in HDF format on 8mm digital tapes from Goddard DAAT. When extracted, the 2A21 level of processing provides 6 different variables with each record: the UTC time in seconds, the latitude of each measurement, the longitude, the σ^o value, the incidence angle and a rain flag. The rain flag is obtained from the complementary combination of data collected by all three instruments in the "rain package".

Subsatellite Track

215 km

TRMM

17 deg

17deg
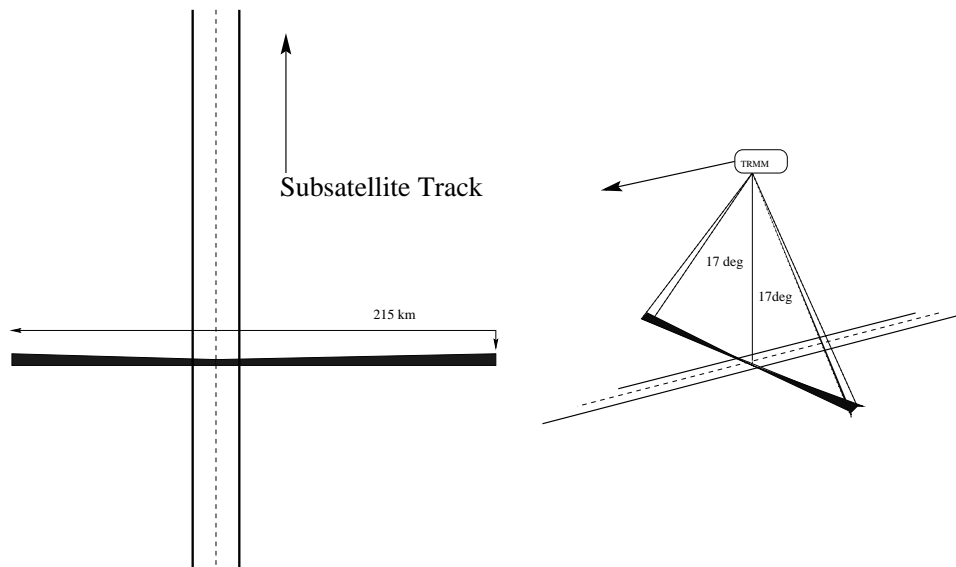
Figure 2.2: The swath pattern of the TRMM Precipitation Radar

2.4 The Scatterometer Image Reconstruction with Filtering algorithm(SIRF)

The Scatterometer Image Reconstruction with Filtering (SIRF) resolution enhancement algorithm is a multivariate nonlinear resolution enhancement algorithm based on modified algebraic reconstruction and maximum entropy techniques. This algorithm was originally developed for application to Seasat scatterometer (SASS) measurements [11] and has recently been optimized for application to NSCAT measurements [10] and for application to TRMM measurements.

Both NSCAT and TRMM PR measure the σ^o of the Earth's surface at several azimuth angles and over a variety of incidence angles at lower nominal resolution (25 km for NSCAT[7], 4-5 km for TRMM PR). Over a limited incidence angle (θ) range of [20°,55°] for NSCAT,[5°,17°] for TRMM ; σ^o (in dB) over land is an approximately linear function of θ, for NSCAT, this function is

$$\sigma^o(\theta) = \mathcal{A} + \mathcal{B}(\theta - 40°)$$

and for TRMM data

$$\sigma^o(\theta) = \mathcal{A} + \mathcal{B}(\theta - 11°)$$

where $\mathcal{A}$ and $\mathcal{B}$ are functions of surface characteristics, azimuth angle, and polarization. $\mathcal{A}$ is the σ^o value at a normalized incidence angle (40°for NSCAT, 11°for TRMM PR) and is termed the incidence angle normalized σ^o. $\mathcal{B}$ describes the dependence of σ^o on θ. The SIRF algorithm generates images of $\mathcal{A}$ and $\mathcal{B}$ on a high resolution grid from the NSCAT σ^o measurements using multiple satellite passes [11]. The $\mathcal{A}$ and $\mathcal{B}$ images are the primary SIRF product. Computation of the $\mathcal{A}$ and $\mathcal{B}$ images are described in detail in [11], and [10]. Examples of $\mathcal{A}$ images are shown in figure(2.3). These two images show the resolution enhancement of SIRF. The image to the left is a non-enhanced radar image and the image to the right has been resolution enhanced using SIRF.

nonenhanced   SIRF resolution enhanced
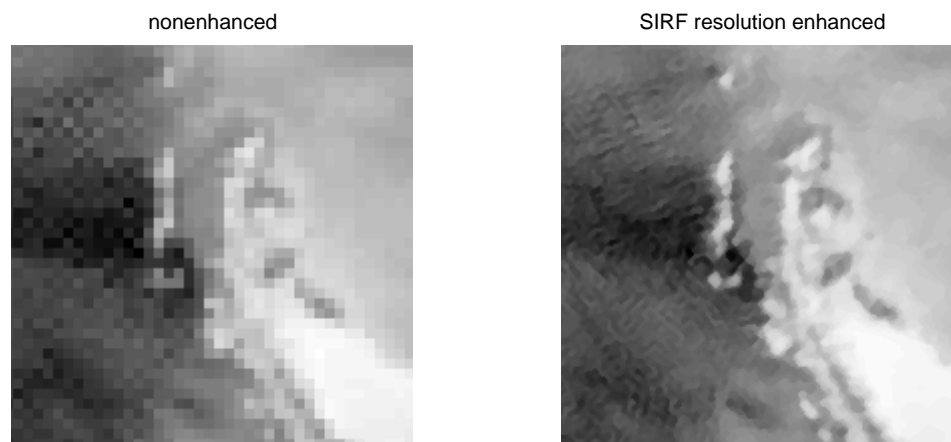
Figure 2.3: A comparison of a nonenhanced radar image and a SIRF resolution enhaced image. The region shown is part of the Antarctic penninsula

Chapter 3

Optimization of SIRF for TRMM

The Tropical Rain Mapping Mission (TRMM) is a joint mission between NASA and the National Space Development Agency (NASDA) of Japan designed to monitor and study tropical rainfall. TRMM has an equitorial orbit between 35°S and 35°N; its rapid repeat coverage making it ideal for the study of large scale tropical phenomena. TRMM was lauched in October of 1997 with five different instruments on board. TRMM Precipitation Radar (TRMM PR), one of these five instruments, is a radar designed to create 3-D images of rainfall. This real aperature phased array radar operates at 13.8 GHz with a swath width of 215 km around the nadir track of the satellite. The high nominal resolution at ground level of TRMM PR suggests that the measurements taken by TRMM could be useful for land studies. Resolution enhancement of images created with TRMM PR data can make the data even more useful. More background information about TRMM and TRMM PR is found in chapter 2.

The Scatterometer Image Reconstruction algorithm with Filtering (SIRF) was designed to enhance scatterometer data resolution by combining data collected over several passes of the scatterometer[11]. Combining the data from several passes is feasible under the assumption of low temporal variablility in σ^o during the observation period. This assumption is generally true for land regions. From an inital estimate, SIRF updates the estimates of σ^o until the value converges. Since SIRF was oringinally designed for SASS, the SIRF algorithm needs to optimized for use with TRMM data.

There were several considerations to made when optimizing SIRF for TRMM.

The radar footprint on the surface of the earth is different for TRMM than for scat-terometers in size, shape, and orientation. The antenna response pattern for TRMM was unknown and needed to be solved for. There are also several parameters of the SIRF algorithm that influence the effectiveness in resolution enhancement. Among these are the $\mathcal{A}$ and $\mathcal{B}$ initialization values, the update weighting coefficient B_{cc}, number of iterations, and data incidence angle sampling. This chapter describes the procedure used to optimize SIRF for TRMM. The first section gives a discussion about SIRF which goes into greater detatil than was given in chapter 2. The next section gives a discussion on the TRMM illumination area or footprint and the an-tenna response associated with that footprint. The third section covers the generation of simulated data and the truth images to be used later in the optimization process. SIRF initialization is examined in the fourth section; simulated SIRF images are created and the results from statistical correlation and error analyses are discussed. Finally, section 5 gives the conclusion drawn from this optimization.

3.1 Scatterometer Image Reconstruction algorithm

The Scatterometer Image Reconstruction (SIR) algorithm generates $\mathcal{A}$ and $\mathcal{B}$ estimates for an image pixel given a σ^o measurement and a corresponding incidence angle measurement. For the TRMM PR, σ^o is approximately a linear function of incidence angle θ between 5° and 17°. Limiting the function to these incidence angles, the relationship between σ^o, $\mathcal{A}$ and $\mathcal{B}$ is described as:

$$10 \log_{10} \sigma^o(\theta) = \mathcal{A} + \mathcal{B}(\theta - 40°) \tag{3.1}$$

where $\mathcal{A}$ and $\mathcal{B}$ are functions of surface characteristics, azimuth angle, and polarization. $\mathcal{A}$ is the σ^o value at 11° incidence and $\mathcal{B}$ describes the dependence of σ^o on θ. $\mathcal{A}$ and $\mathcal{B}$ provide valuable information about the surface. An angle of 11° is chosen as a mid-swath value, though any interior swath angle can be used [12].

SIRF is based on the spatial overlap of σ^o measurements from multiple passes of the satellite and on image reconstruction techniques. It is important for the imple-mentation of TRMM SIRF to have a correct understanding of the TRMM footprint

18

and antenna response pattern. This is part of the optimization process and will be discussed in great detail in the next section.

The Scatterometer Image Reconstruction (SIR) algorithm is closely related to Multiplicative Algebraic Reconstruction (MART) [10]. In MART, each measurement is compared to a forward projection for that value computed from the current estimate image. A multiplicative correction factor is then applied to each pixel covered by the measurement causing the forward projection to equal the measurement. Over multiple iterations, the correction factors ideally converge to a value of unity and the forward projection match the measurements. The problem with MART is that it has a limited noise tolerance. SIR is a modified version of MART that has been optimized to tolerate the noisy scatterometer measurements. Because TRMM measurements are unusually noisy, TRMM SIR must be optimized to achieve the most accurate results.

SIR obviously requires initial estimates for both $\mathcal{A}$ and $\mathcal{B}$. The better these estimates are, the quicker the convergence and the greater the accuracy of the images. in the kth iteration of the algorithm, the previous $\mathcal{B}$ estimate is used to normalize the σ^o measurements from which the $\mathcal{A}$ estimate is generated. Linear regression of the update terms then is used to compute a new estimate for $\mathcal{B}$ (a weighted average of the previous $\mathcal{B}$ estimate and the the new $\mathcal{B}$ estimate update). The multivariate SIR algorithm is given below [11].

We express the measurements z_j in dB so the forward projection f_j^k is computed in normal space while the $\mathcal{A}$ and $\mathcal{B}$ estimates are in log space, i.e.,

$$f_j^k = 10 \log_{10} \left[\frac{1}{q_j} \sum_{n=1}^{N} h_{jn} 10^{a_n^k/10} \right] \tag{3.2}$$

where q_j is defined in Eq. (3.4) and

$$p_i = \sum_{l=1}^{N} h_{li} \tag{3.3}$$

$$q_j = \sum_{l=1}^{M} h_{jl}. \tag{3.4}$$

Define d_{ij}^k as

$$d_{ij}^k = \left(\frac{z_j - b_i^k(\theta_j - 40°)}{f_j^k} \right)^w. \tag{3.5}$$

19

The case with $w = 1$ is unweighted MART while $w = 1/2$ is referred to as weighted MART and is used in SIRF. The $\mathcal{A}$ estimate update term, u_{ij}^k, is computed,

$$u_{ij}^k = \begin{cases} \left[\frac{1}{2} \frac{1}{f_j^k} \left(1 - \frac{1}{d_{ij}^k} \right) + \frac{1}{a_i^k d_{ij}^k} \right]^{-1} & d_{ij}^k \geq 1 \\ \left[\frac{1}{2} f_j^k \left(1 - d_{ij}^k \right) + a_i^k d_{ij}^k \right] & d_{ij}^k < 1 \end{cases} \tag{3.6}$$

with the $\mathcal{A}$ estimate, a_i^k, updated according to

$$a_i^{k+1} = \frac{1}{p_i} \sum_{j=1}^{N} h_{ji} u_{ij}^k. \tag{3.7}$$

To compute the $\mathcal{B}$ estimate, let

$$r_i = \sum_{j=1}^{N} h_{ji} \theta_j^2 \tag{3.8}$$

$$t_i = \sum_{j=1}^{N} h_{ji} \theta_j \tag{3.9}$$

and

$$\zeta_{ij}^k = u_{ij}^k + b_i^k (\theta_j - 40°). \tag{3.10}$$

Then, the linear regression of the $\mathcal{A}$ updates, u_{ij}^k, provides an update for $\mathcal{B}$,

$$c_i^k = \frac{1}{p_i r_i - t_i^2} \left(p_i \sum_{j=1}^{N} h_{ji} \theta_j \zeta_{ij}^k - t_i \sum_{j=1}^{N} h_{ji} \zeta_{ij}^k \right). \tag{3.11}$$

This update is only usable if the range of incidence angles (θ_j) used in Eq. (3.11) is sufficiently wide. Since a wider incidence angle range implies greater confidence in the $\mathcal{B}$ estimate update [11], the $\mathcal{B}$ estimate is updated using a weighted average of c_i^k and the previous $\mathcal{B}$ estimate. The weighting factor is a simple function of the variance of θ, i.e., let

$$x_i = \frac{p_i}{t_i^2} \sum_{j=1}^{N} h_{ji} \theta_j^2 - 1 \tag{3.12}$$

then the $\mathcal{B}$ estimate image is updated according to

$$b_i^{k+1} = \frac{1}{x_i + 1} \left(x_i c_i^k + b_i^k \right). \tag{3.13}$$

This system of equations is theoretically iterated over k until convergence. Typically, however, the iterations are terminated at near convergent conditions.

The image can be further improved by applying a 3x3 median filter to the images. This filter will preserve the edges but remove any small salt and pepper noise that might result. The image noise can also be reduced significantly by applying a hybrid linear-median filter to the $\mathcal{A}$ and $\mathcal{B}$ images at each iteration of the SIR algorithm. This hybrid filter checks the values of the image pixels within a 3x3 moving window. If the difference between the second highest and the second lowest values within the window is less than 0.25, then the center pixel is replaced with the average of the middle seven values within the window. If the difference is greater than 0.25, than the filter acts as a normal median filter. The SIR algorithm with the added filtering is called SIRF [10].

Sample TRMM SIR $\mathcal{A}$ and $\mathcal{B}$ images are shown in Figures (3.1) and (3.2). This particular image was created using one months worth of data and has a resolution of about 1 km per pixel (nominal resolution of TRMM is between 4-5 km).

3.1.1 A note on B acceleration

The original version of SIRF was developed for use with Seasat Scatterometer (SASS) data and the $\mathcal{B}$ updates were heavily damped in that version. In later versions of SIRF, most specifically the NSCAT version, the $\mathcal{B}$ updates were accelerated with an acceleration constant $\mathcal{B}_{acc}$. Equation (3.13) defines the update for $\mathcal{B}$ based on the linear regression of $\mathcal{A}$ update constants (c_i^k) and a weighting factor x_i determined by the variance of incidence angles [Eq. (3.12)] [10].

The $\mathcal{B}$ updates can further be acceperated by weighting Eq. (3.12) by the $\mathcal{B}$ acceleration constant, b_{acc}:

$$x_i = b_{acc} \left(\frac{p_i}{t_i^2} \sum_{j=1}^{N} h_{ji} \theta_j^2 - 1 \right) \qquad (3.14)$$

Acceleration of the $\mathcal{B}$ updates accelerates the convergence of the $\mathcal{B}$ values and consequently the $\mathcal{A}$ values. If the acceleration constant is chosen too high, the algorithm can go unstable. The acceleration constant for TRMM PR SIRF was approximated to be 50. SIRF needs to be optimized for this value of b_{acc}.
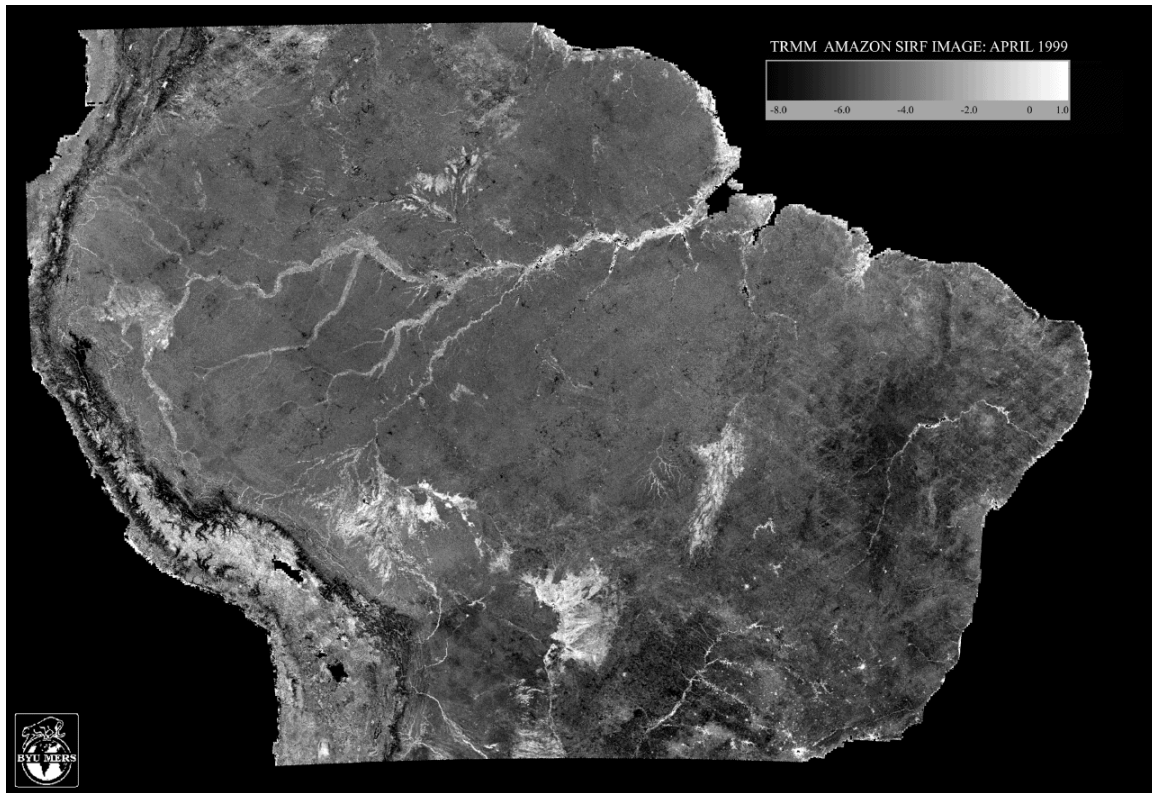
Figure 3.1: A sample TRMM PR SIR $\mathcal{A}$ image over the Amazon basin during April, 1999
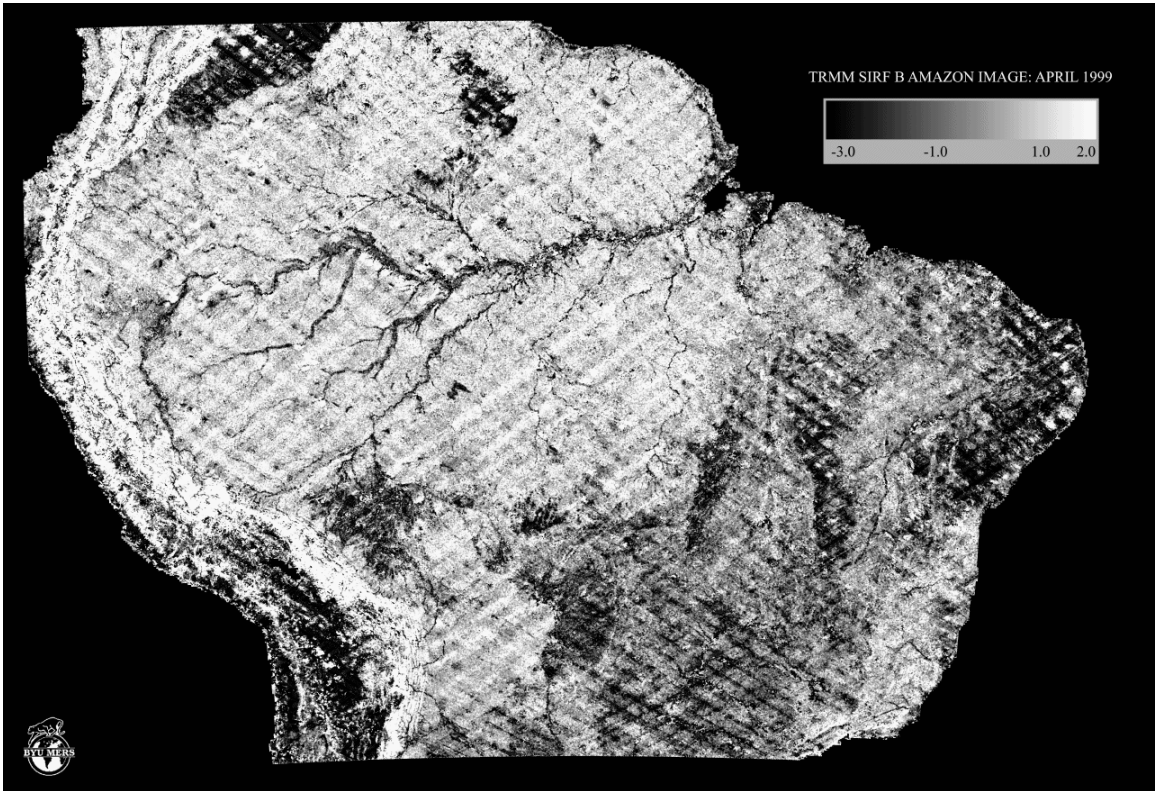
Figure 3.2: A sample TRMM PR SIR $\mathcal{B}$ image over the Amazon basin during April, 1999

3.2 TRMM footprint and Antenna Pattern

An understanding of cell geometry and swath pattern is needed for efficient and correct implementation of the SIRF algorithm using TRMM data. SIRF was originally written for a fan beam scatterometer that collected σ^o measurements. Cell geometry was determined by the fan beam geometry of the scatterometer and use of doppler filtering [10]. This resulted in a lengthened elliptical footprint. Although TRMM PR collects similar data, the antenna used is different and therefor the antenna response footprint will also be different. TRMM Precipatation Radar operates at incident angles between nadir and 17°. It is a scanning radar that scans from 17° incidence on one side of the spacecraft through nadir to 17° incidence on the other side. This creates a swath 215 km long perpendicular to the path of the spacecraft. As the sattelite travels forward, the radar transmits and measures σ^o values at specific incidence angles. Figure (3.3) illustrates the swath created by these individual measurements. The beamwidth of the TRMM PR is 0.71°. This yields an elliptical footprint that has a nominal resolution of 4.2 km in the along track direction and varies from 4.2 to 5 km in the cross-track direction. This elliptical TRMM cell is shown in Figure (3.4) overlaying the higher resolution grid of SIRF resolution elements.

The response pattern of an antenna is the strength of the signal that hits different parts of the illuminated area on the earth. The center of the footprint will typically have the highest response and the edges will typically receive the least incident energy. Refering once again to Figure (3.4), the value of σ^o measured by the scatterometer (denoted by ϱ_k where k is the measurement number is a weighted average of the individual SIRF resolution elements covered by the footprint [10].

$$\varrho_k = \sum_{c=L_k}^{R_k} \sum_{a=B_k}^{T_k} h(x,y;k)\sigma^o(x,y;k) \tag{3.15}$$

The weighting function $h()$ is the response pattern of the antenna. The detailed antenna response pattern for TRMM is unknown to this investigation. A technique called umphaliskepis was used to determine an approximation to the pattern. Several
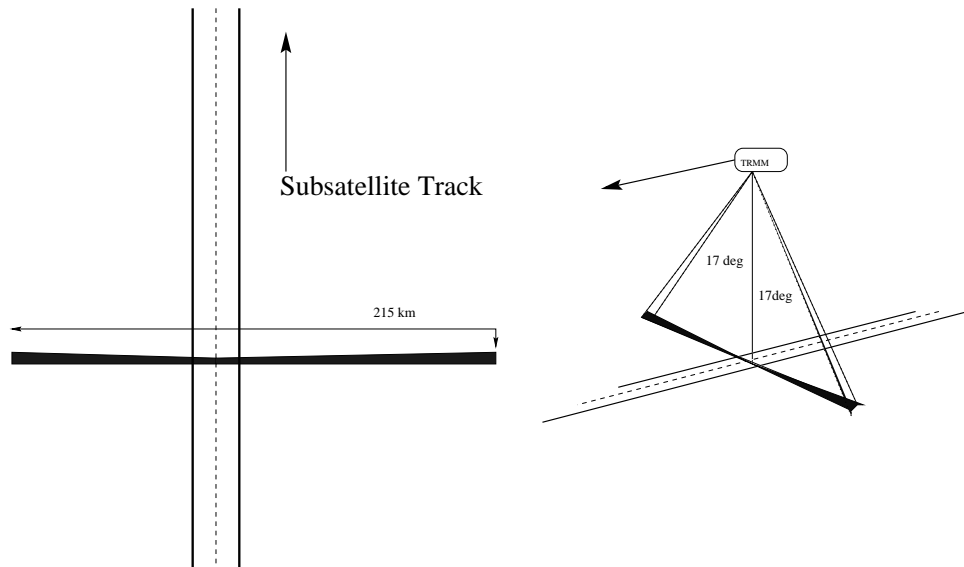
Figure 3.3: TRMM PR scanns a swath that is 4 km long in the along-track direction on the earth surface and 215 km long in the across-track direction
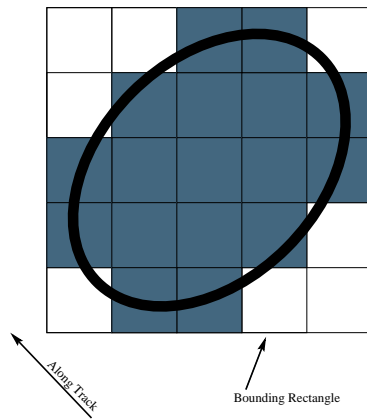
Figure 3.4: An integrated TRMM σ^o cell overlaying the higher resolution grid. Only the shaded cells have a non-zero h(x,y,k)

possibilities were determined, including a cosine roll off pattern, a cosine^2 roll-off pattern, cosine^3 roll-off pattern and a flat response over the illumination area. Using these possibilities for the weighting function, test images were constructed and the cosine squared roll-off pattern was subjectively chosen. Figure (3.5) shows the cosine squared antenna pattern over the elliptical footprint.
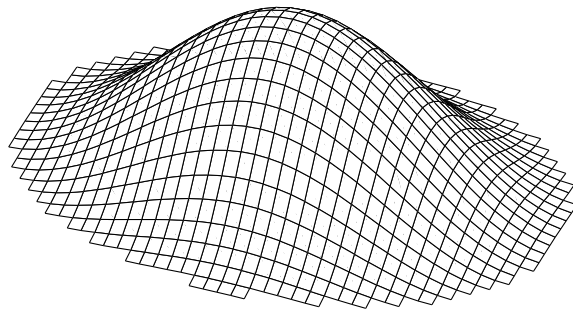
Figure 3.5: The assumed antenna response pattern for TRMM PR, a cosine squared function over the elliptical footprint.

3.3 Generating Simulation Data and Images

In order to be able to study and optimize many of the parameters used by SIRF such as the number of iterations, $\mathcal{A}_{init}$ and $\mathcal{B}_{init}$, it is necessary to run simulations of SIRF using known simuation data truth images. These synthetic images can be used with a truth image to correctly select optimum parameter values. This section discusses the creation of simulation data and of the synthetic truth images.

TRMM PR 2A21 data records contain geolocation, incidence angle, σ^o, UTC time in seconds, and a rain flag to designate which data might be tainted by rain. SIRF only uses the time count, σ^o and the incidence angle. Simulated data is generated using 30 days of actual TRMM data (1998 April) taken from over the Amazon Basin (latitude range 16°S to 8°S, longitude range 65°W to 70°W) combined with a synthetic truth image. Figure 3.6 shows the truth image. This image is a synthetic $\mathcal{A}$ image. For the purposes of the simulation, the $\mathcal{B}$ image is approximated as unity. The synthetic truth $\mathcal{A}$ image was designed to emulate some features that might naturally be encountered in actual scatterometer observations. Towards the bottom of the truth image, there is a darker area that simulates a river bed with characteristically low $\mathcal{A}$ values. Above that feature, there is a rectangular feature with gradually increasing σ^o. The lighter squares of decreasing size toward the upper left of the image tests the ability of SIRF to resolve smaller objects. The light round object towards the upper right is used to investigate the effect of the filter on round features. In the simulation, actual data provides the geolocation, the time variable and incidence angle information while σ^o is computed from the synthetic truth image.

The truth image is created at a higher resolution (approximately 1 km per pixel) than the nominal resolution of the TRMM PR (4-5 km). σ^o is computed from effective $\mathcal{A}$ values of the higher resolution element in the antenna footprint (see Figure (3.4)).

$$\varrho_k = \sum_{c=L_k}^{R_k} \sum_{a=B_k}^{T_k} h(x, y; k) \sigma^o(x, y; k) \tag{3.16}$$

where L_k, R_k, T_k and B_k define a bounding rectangle for the kth hexagonal σ^o measurement cell, h(x,y,k) is the weighting function or antenna response pattern for

the (x,y)th resolution element and the kth measurement; and $A_{truth}(x, y, k)$ is the $\mathcal{A}$ value for the (x,y)th SIRF resolution element. σ^o then is equal to this A_{eff} as there is no B_{eff} computed for this simulation. (see equation ??)

The simulations were designed originally to use the actual variance values of the scatterometry data to compute simulated noise. TRMM PR does not provide such data and so it is necessary to estimate the average variance and thus introduce noise. Two regions were selected, one over the Sahara (latitude range 24°N to 28 °N; longitude range 9°E to 12°E) and one over the Amazon Basin (latitude range 6°S to 10 °S; longitude range 50°W to 55°W), and data was extracted over a 30 day period (1998 April). It was assumed that this large a day range and data over two such opposite terrains would give an accurate average of the variance in TRMM PR measurements. Realistic simulated σ^o measurements can then be obtained by:

$$\sigma^o_{sim} = \sigma^o_{truth} + \mathcal{N}(0, xstd) \tag{3.17}$$

where $\mathcal{N}(0, xstd)$ is a zero mean normal distribution with standard devation of $xstd$ given by

$$xstd = \sigma^o_{truth} * K_p \tag{3.18}$$

where the K_p value used is determined as an average over the earth and is given by:

$$K_p = \frac{std(\mathcal{A}(i, j))}{\frac{1}{HW} \sum_{i=1}^{H} \sum_{j=1}^{W} \mathcal{A}(i, j)} \tag{3.19}$$

Figures (3.8) and (3.7) show plots of the mean σ^o as a function of incidence angle, the standard devation as a function od incidence angle and the resulting K_p value as a function of incidence angle for the regions in the Sahara and the Amazon, respectively. At the SIRF reference angle of 11°, the value of K_p was chosen to be equal to 1. This effectively makes the power in the noise equal to the power in the actual measurements.
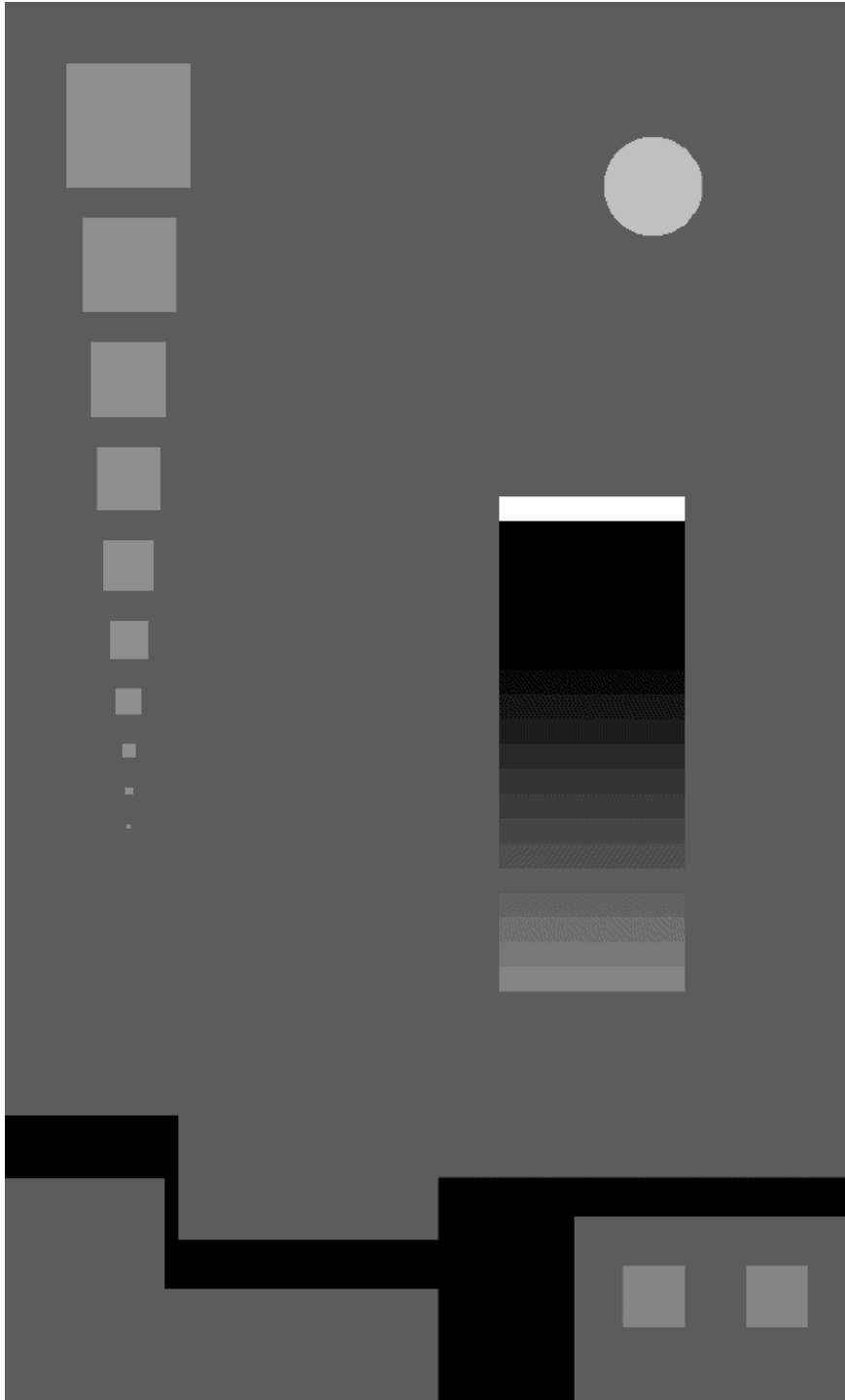
Figure 3.6: Synthetic truth $\mathcal{A}$ image.
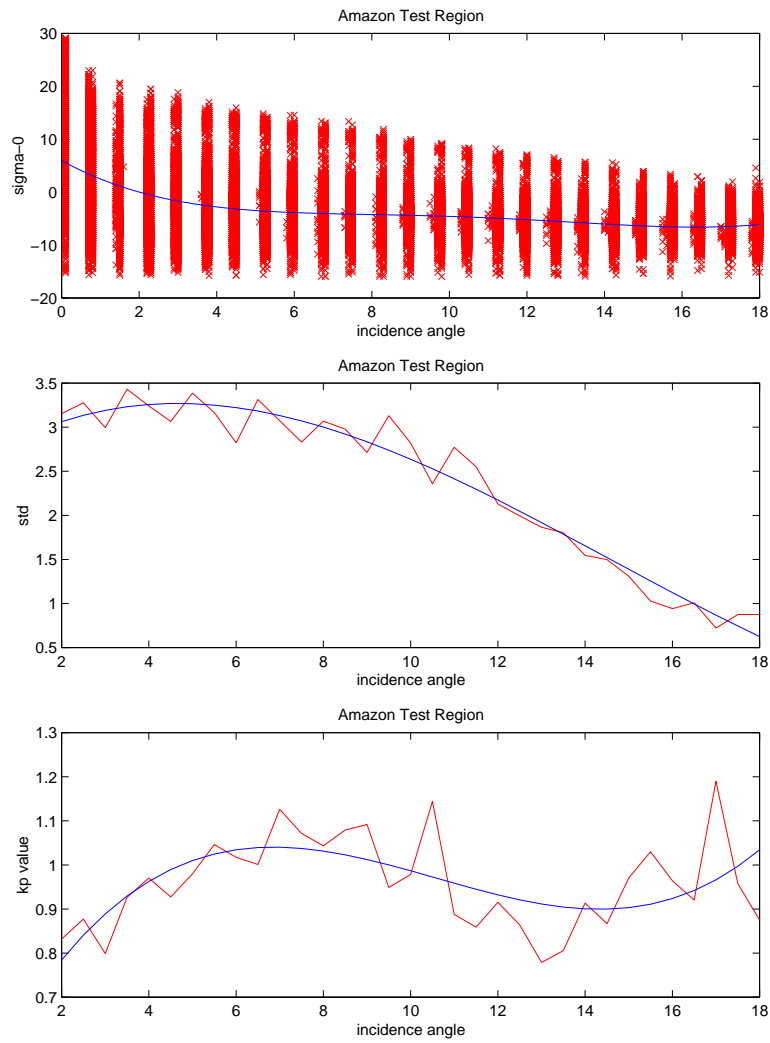
Figure 3.7: Data taken over the Amazon in April, 1998 was analysed to give the mean σ^o value, the stardard deviation and the Kp value, all as a function of incidence angle.
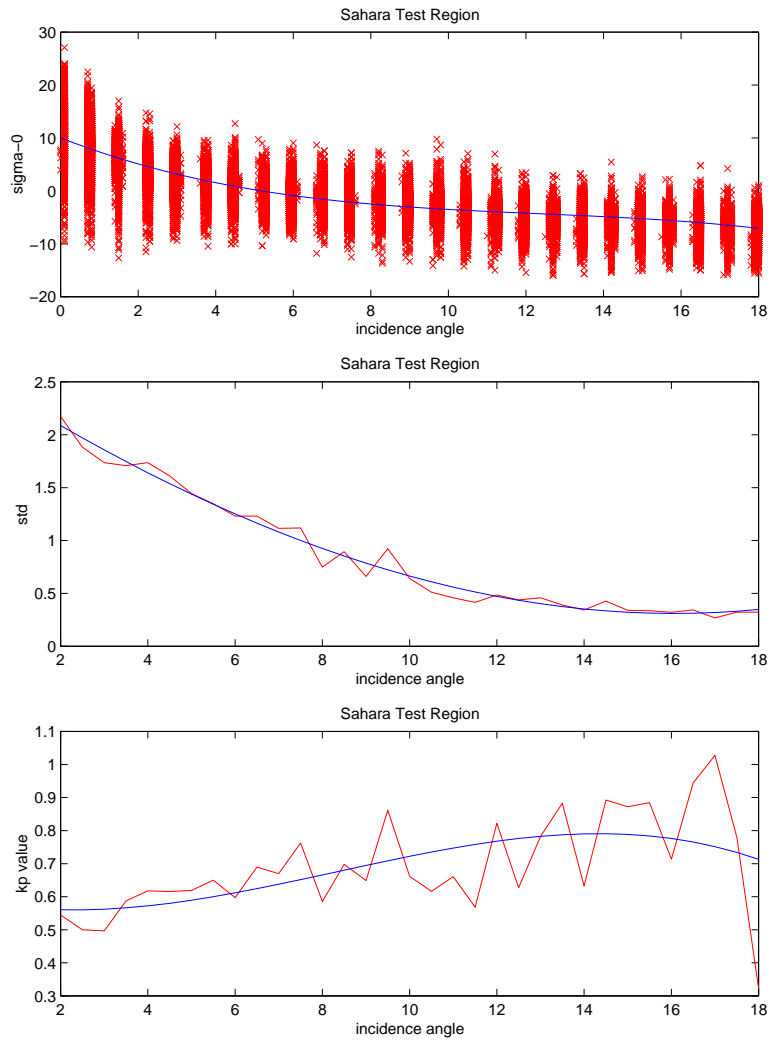
Figure 3.8: Data taken over the Sahara in April, 1998 was analyzed to give the mean σ^o value, the stardard deviation and the K_p value, all as a function of incidence angle.

3.4 SIRF Initial Values and Statisitical Analyses

SIRF requires initial $\mathcal{A}$ and $\mathcal{B}$ values. The algorithm iteratively updates the estimate by comparing the previous estimate with new data values. If a poor initial value is used, the $\mathcal{A}$ and $\mathcal{B}$ values may not converge sufficiently in a reasonable number of iterations and may not provide acceptable accuracy. $\mathcal{A}_{init}$ and $\mathcal{B}_{init}$ can be thought of as global averages of these two values. This section will describe how the number of iterations and the values of $\mathcal{A}_{init}$ and $\mathcal{B}_{init}$ were chosen using a statistical analysis of the simulated images.

To study the effects of different $\mathcal{A}$ and $\mathcal{B}$ initialization values, simulated data with added noise was used to produce enhanced resolution SIRF images. Simulated data was generated using the above described process for small region over the Amazon for the month of April 1998. The σ^o values used in the data were taken from the truth image shown in Figure (3.6) and the other parameters used by SIRF were extracted from actual TRMM data. This data was used to create thirty-five different sets of images, each with a different combination of $\mathcal{A}_{init}$ and $\mathcal{B}_{init}$ values. SIRF was modified for this test to output a different file for every iteration so that the different SIRF results could be compared as a function of iteration number. The $\mathcal{A}_{init}$ values used vary from -7.2 dB to -3.2 dB while the $\mathcal{B}_{init}$ value is set to various values in the range of -5 dB to 0.5 dB. The SIRF algorithm is allowed to progress to 75 iterations.

Three different metrics were used to compare the effect of the different parameter values on the SIRF algorithm: mean error, rms error and the correlation coefficient. Each different image created is compared to the truth image pixel by pixel and the mean error, the rms error and the correlation coefficient are computed for the image.

$$Err_{mean} = \frac{1}{HW} \sum_{i=1}^{H} \sum_{j=1}^{W} \mathcal{A}(i,j) - \mathcal{A}_{truth}(i,j) \tag{3.20}$$

$$Err_{rms} = \frac{1}{HW} \sqrt[2]{\sum_{i=1}^{H} \sum_{j=1}^{W} (\mathcal{A}(\rangle, |) - \mathcal{A}_{\sqcup \nabla \sqcap \sqcup \langle}(\rangle, |))^{\in}} \tag{3.21}$$

$$corrco =$$

$$\frac{\sum\limits_{i=1}^{H}\sum\limits_{j=1}^{W}(\mathcal{A}_{truth}(i,j) - \frac{1}{HW}\sum\limits_{i=1}^{H}\sum\limits_{j=1}^{W}\mathcal{A}_{truth}(i,j))(\mathcal{A}(i,j) - \frac{1}{HW}\sum\limits_{i=1}^{H}\sum\limits_{j=1}^{W}\mathcal{A}(i,j))}{\sqrt[2]{\sum\limits_{i=1}^{H}\sum\limits_{j=1}^{W}(\mathcal{A}_{truth}(i,j) - \frac{1}{HW}\sum\limits_{i=1}^{H}\sum\limits_{j=1}^{W}\mathcal{A}_{truth}(i,j))^2}\sqrt[2]{\sum\limits_{i=1}^{H}\sum\limits_{j=1}^{W}(\mathcal{A}(i,j) - \frac{1}{HW}\sum\limits_{i=1}^{H}\sum\limits_{j=1}^{W}\mathcal{A}(i,j))^2}}$$

$$(3.22)$$

These values are plotted with repect to the $\mathcal{A}_{init}$, $\mathcal{B}_{init}$ values as a function of iteration number and are shown in Figures (3.9) through (3.16). These plots show the results for each $\mathcal{A}_{init}$ value tested and one individual $\mathcal{B}_{init}$ value as a function of iteration number. It should be noted that for each case, the error plots reach a minimum and the correlation plots reach a miximum between 5 and 10 iterations. After this point, the error in the SIRF images increases do to an amplification of the inherent noise in TRMM data. This is the effect of the unusually high K_p of TRMM data. The SIRF algorithm improves the resolution and quality of an image until the noise amplification starts to degrade the image.

3.5   Summary and Conclusions

The Scatterometer Image Reconstrcution with Filtering algorithm allows us to effectively reconstruct high resolution images from intrinsically lower resolution TRMM Precipatation Radar data. These images are useful for non-oceanic studies.

Several parameters affect the accuracy and quality of the images created by SIRF. The antenna footprint size and orientation, the antenna response, the $\mathcal{A}$ and $\mathcal{B}$ initialization values and the number of iterations all affect the quality of the images and are optimized to ensure the highest quality TRMM SIRF images.

Nonhomogeneous sythetic images were created to study the effect of $\mathcal{A}$ and $\mathcal{B}$ initialization values on the error and correlation properties between SIRF images and their truth counterparts. The statistical metrics improved quickly and reached an optimum value between the fifth and nineth iteration. After this number of iterations, the statistical metrics degrade due to the high K_p value inherent in TRMM data.

It was determined from these studies that the optimum $\mathcal{A}_{init}$ value is -5.2dB, the optimum $\mathcal{B}_{init}$ value is -.7dB, and the number of SIRF iterations at which the images reach the closest match to the truth image is 8.

Figure 3.9: Mean error, RMS error and Correlation Coefficient as a function of iteration number for $\mathcal{B}_{init}$ value = 3.0 dB, $\mathcal{A}_{init}$ = -3.2,-4.2, -5.2, -6.2 and -7.2 dB

Figure 3.10: Mean error, RMS error and Correlation Coefficient as a function of iteration number for $\mathcal{B}_{init}$ value = 3.0 dB, $\mathcal{A}_{init}$ = -3.2,-4.2, -5.2, -6.2 and -7.2 dB

Figure 3.11: Mean error, RMS error and Correlation Coefficient as a function of iteration number for $\mathcal{B}_{init}$ value = 3.0 dB, $\mathcal{A}_{init}$ = -3.2,-4.2, -5.2, -6.2 and -7.2 dB

Figure 3.12: Mean error, RMS error and Correlation Coefficient as a function of iteration number for $\mathcal{B}_{init}$ value = 3.0 dB, $\mathcal{A}_{init}$ = -3.2,-4.2, -5.2, -6.2 and -7.2 dB
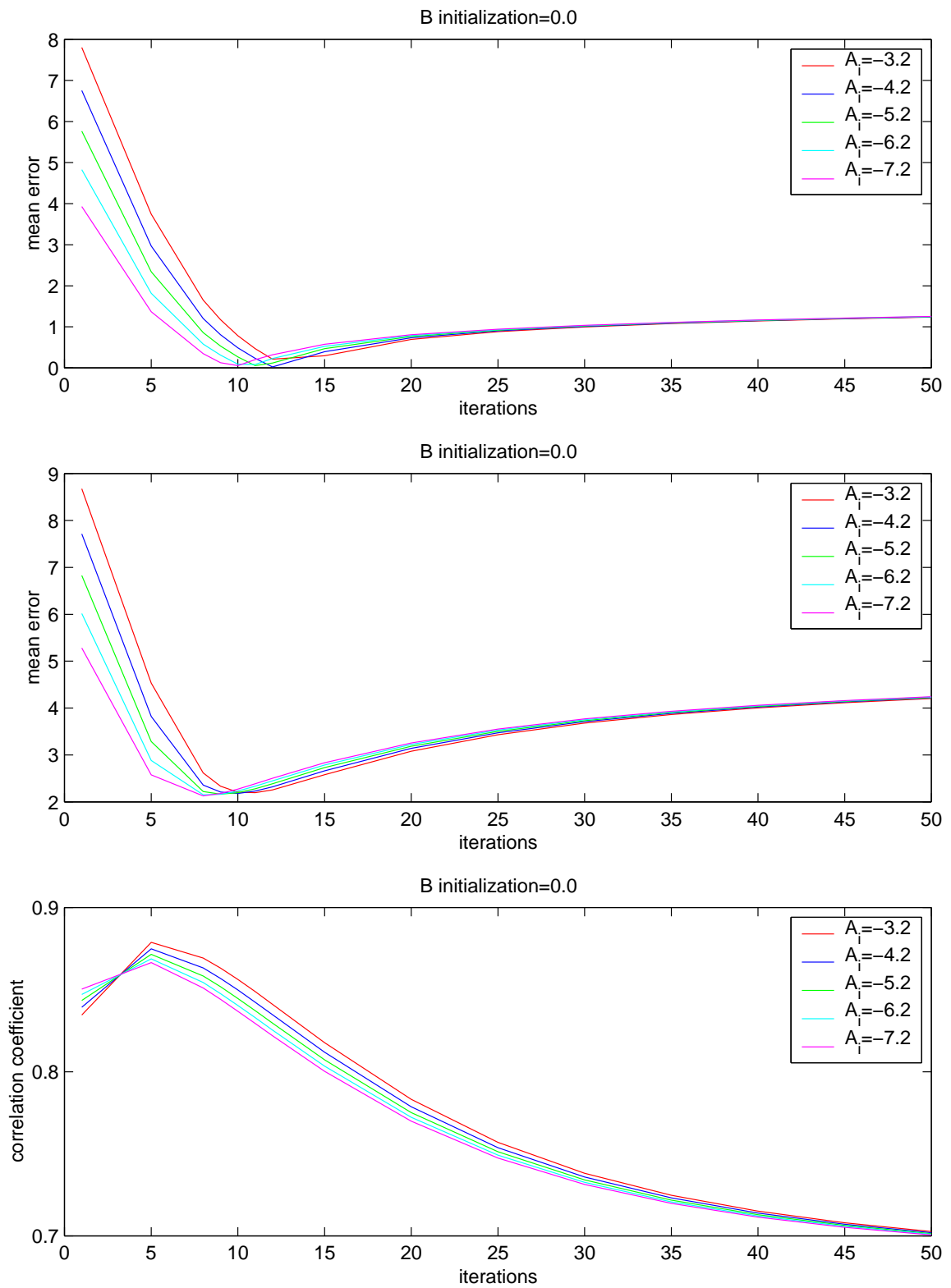
Figure 3.13: Mean error, RMS error and Correlation Coefficient as a function of iteration number for $\mathcal{B}_{init}$ value = 3.0 dB, $\mathcal{A}_{init}$ = -3.2,-4.2, -5.2, -6.2 and -7.2 dB
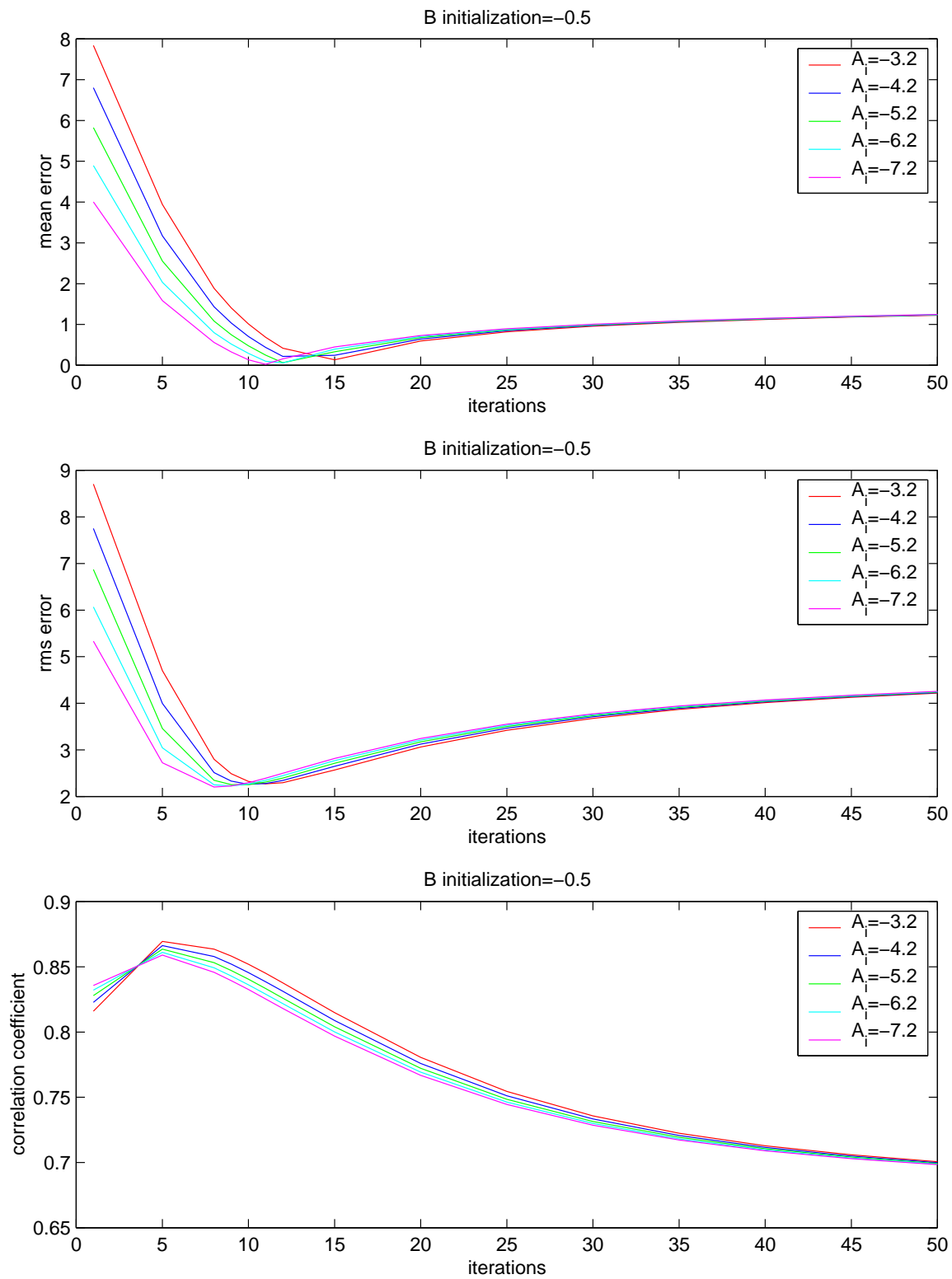
Figure 3.14: Mean error, RMS error and Correlation Coefficient as a function of iteration number for $\mathcal{B}_{init}$ value = 3.0 dB, $\mathcal{A}_{init}$ = -3.2,-4.2, -5.2, -6.2 and -7.2 dB
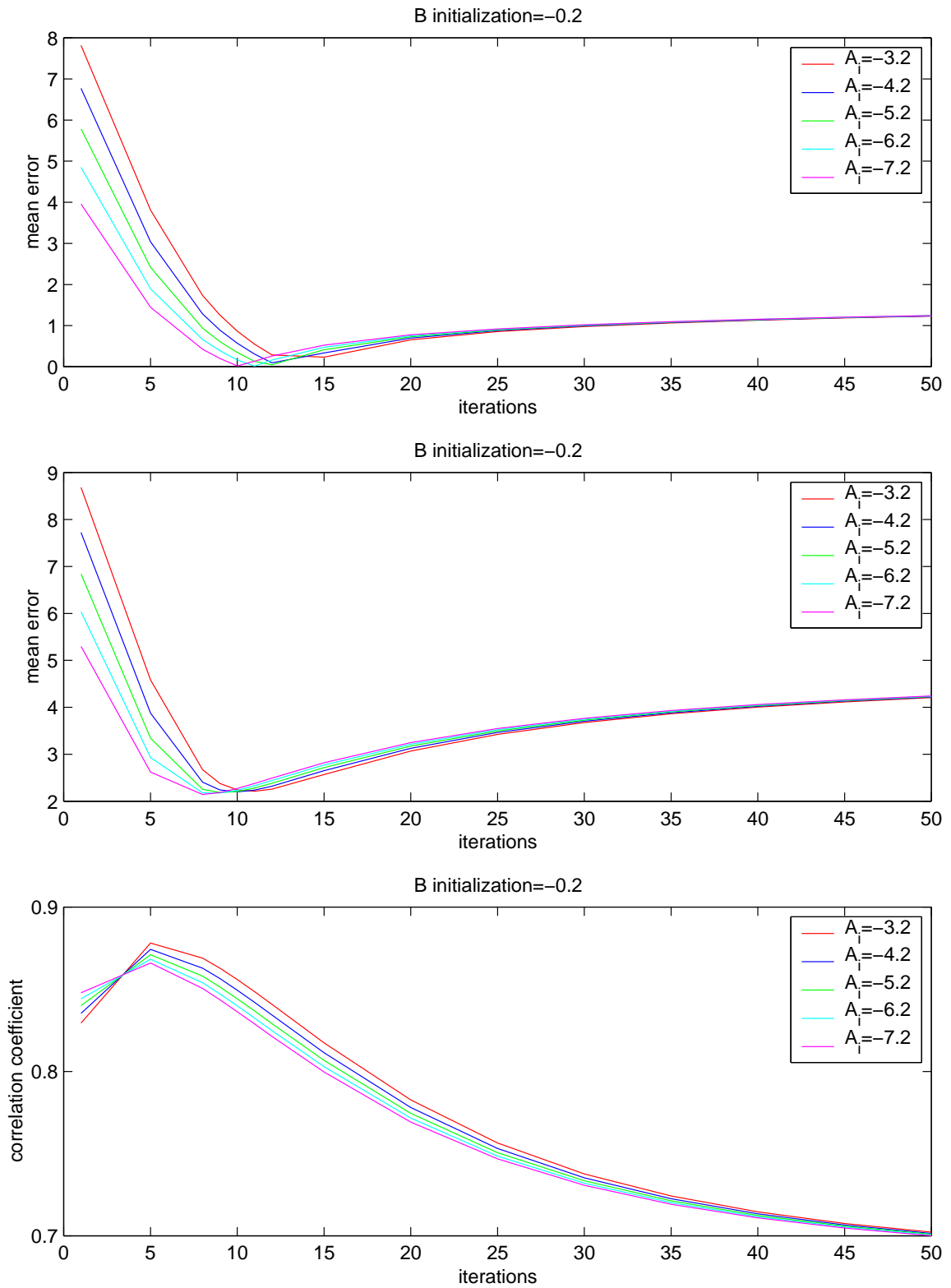
Figure 3.15: Mean error, RMS error and Correlation Coefficient as a function of iteration number for $\mathcal{B}_{init}$ value = 3.0 dB, $\mathcal{A}_{init}$ = -3.2,-4.2, -5.2, -6.2 and -7.2 dB
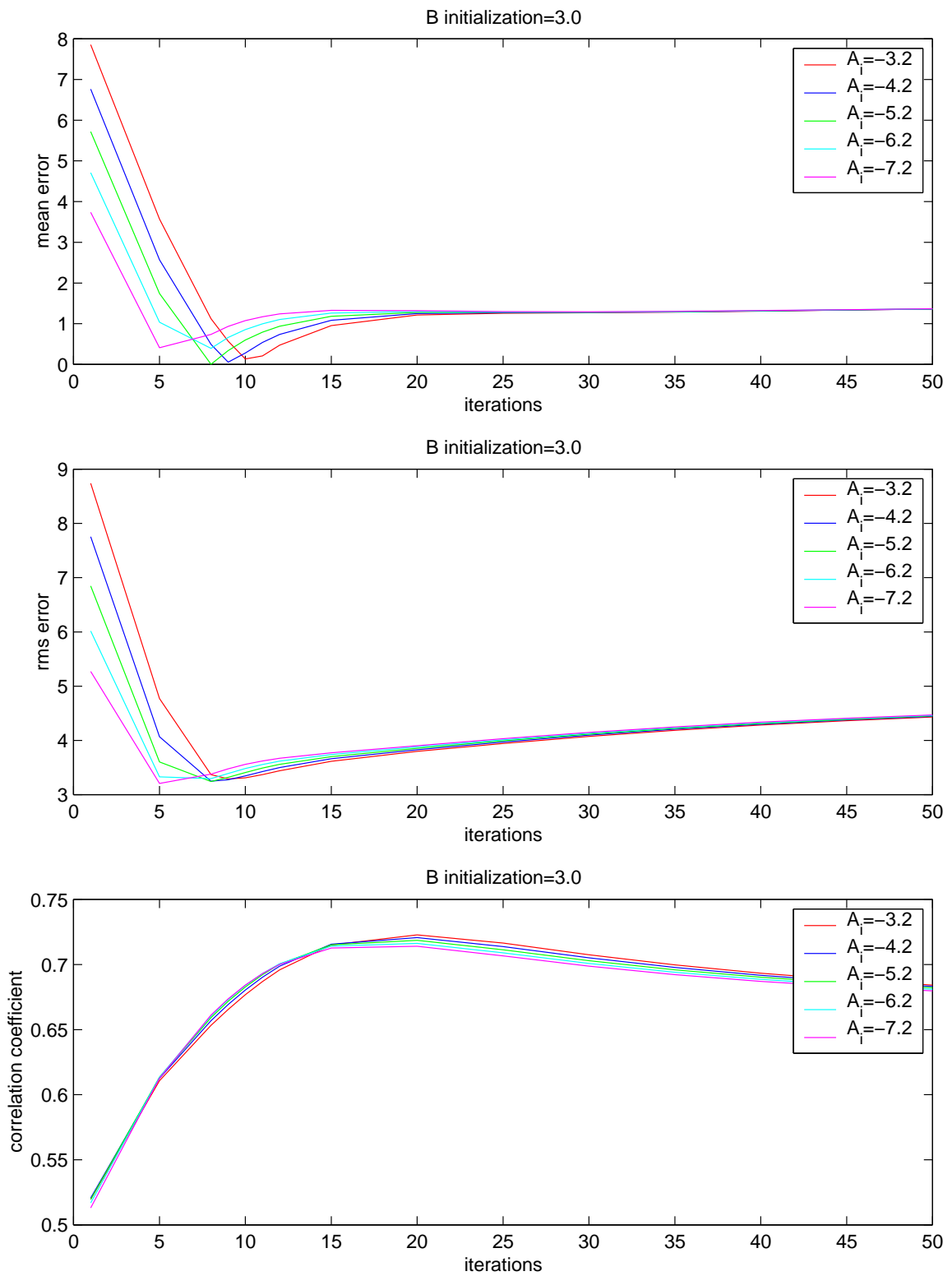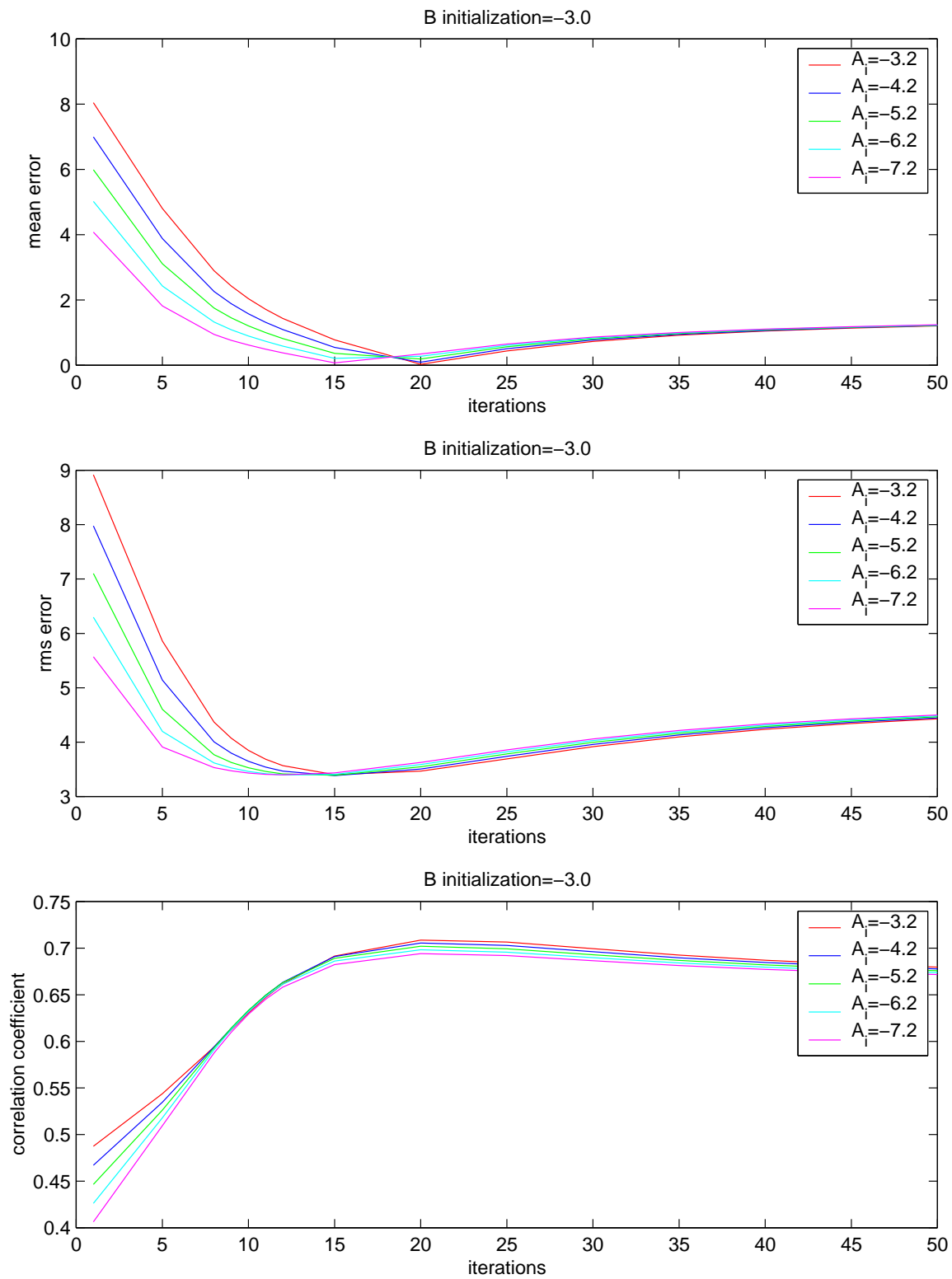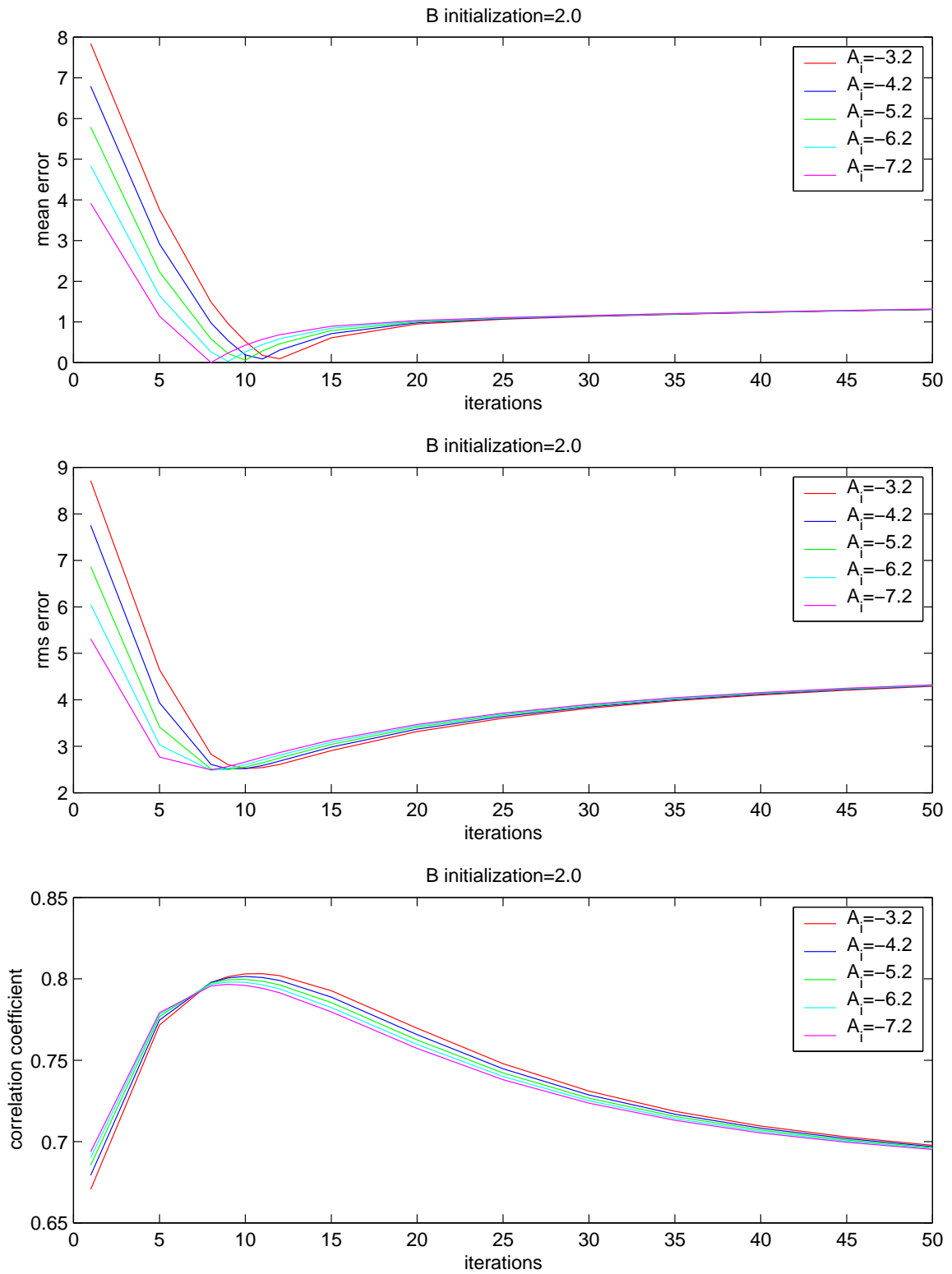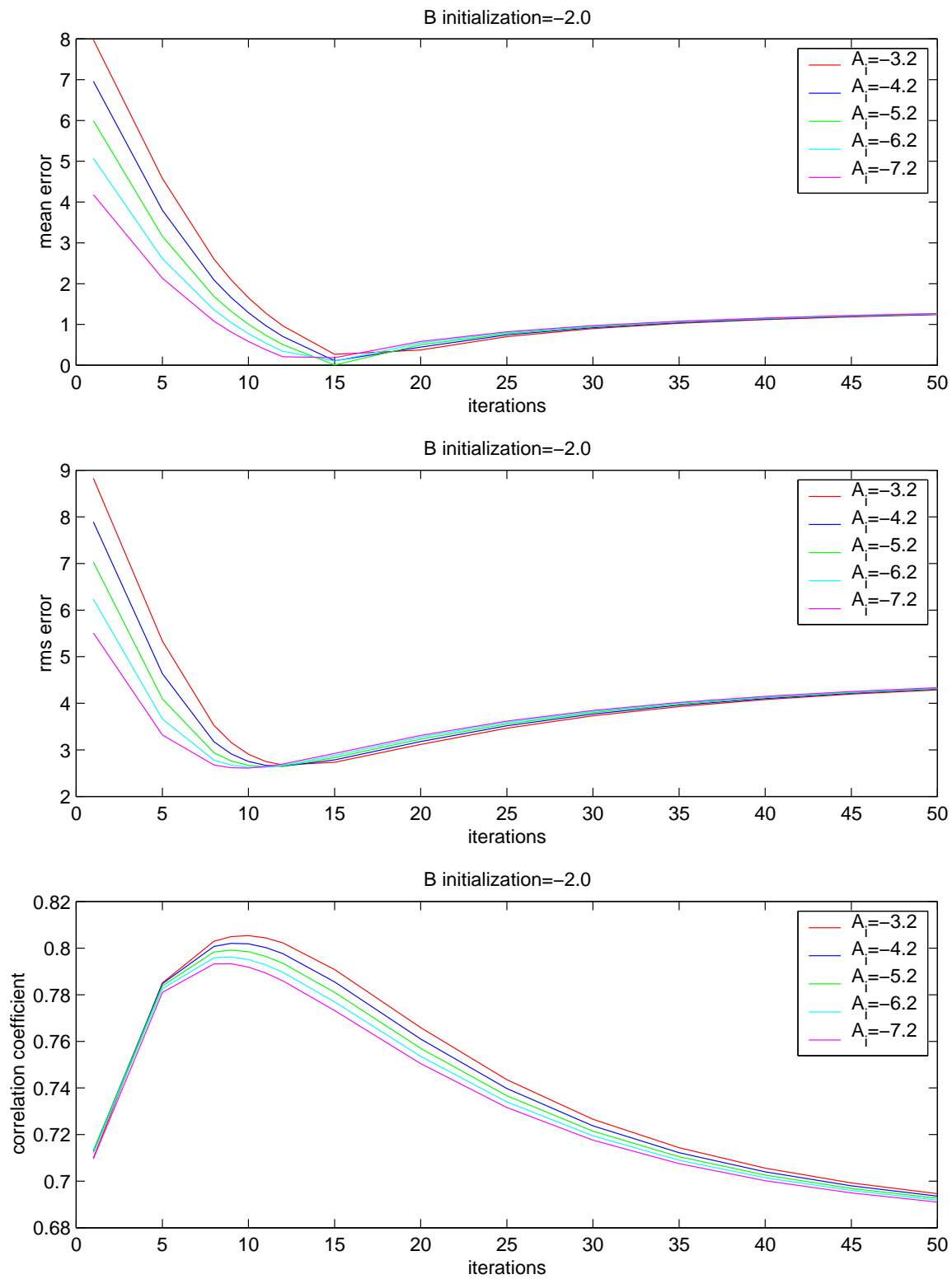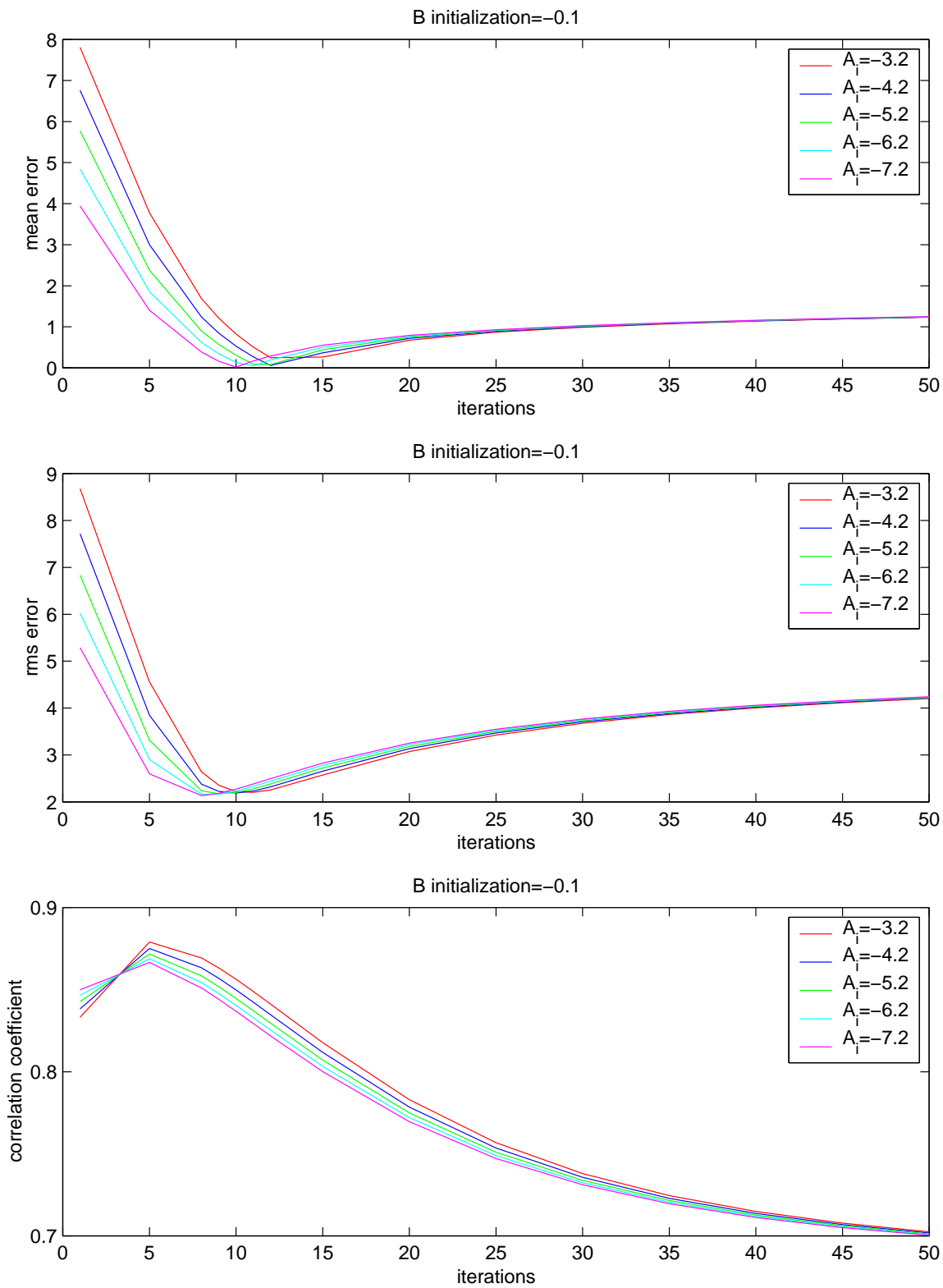
Figure 3.16: Mean error, RMS error and Correlation Coefficient as a function of iteration number for $\mathcal{B}_{init}$ value = 3.0 dB, $\mathcal{A}_{init}$ = -3.2,-4.2, -5.2, -6.2 and -7.2 dB

Chapter 4

Ku-Band Backscatter Signatures Over Tropical Vegetation Types

The study of vegetation over the earth, esspecially over the equatorial regions, is important to global weather and climate models. Areas such as the vast equatorial rain forests greatly affect the weather in the tropics, the amount of moisture in the air and the amount of oxygen produced. These factors have an effect on the global climate and weather models. For the purpose of studying the weather on a global level, many spaceborne satellites have been constructed to observe the earth. Scatterometers are of this group of satellites and were designed to study wind patterns over the ocean. This chapter shows that these scatterometers and other similar satellites can also be used to study the landcover and vegetation on a global or regional scale. This report compares the backscatter at Ku-band for different types of tropical vegetation. This comparison is made with images created using the Scatterometer Image Reconstruction with Filtering(SIRF) algorithm developed at Brigham Young University. Both NSCAT data and TRMM PR data is used in the creation of these images. NSCAT was chosen because TRMM PR and NSCAT have similar operating frequencies (13.8 and 13.995 Ghz, respectively) but are complementary to each other in incidence angle range. TRMM collects backscatter measurements between nadir and 17°; NSCAT collects measurements between 20°and 70°. Chapter 2 of this thesis provides a complete background SIRF, TRMM PR and NSCAT.

4.1   Training Regions

In order to accurately compare the σ^o from different vegetation types over the Amazon, it is imperative to be able to choose "truth" regions where the land cover

type is known. There are several available vegetation "truth" maps. The one used for this study is the Matthews Global Vegetation, Land Use, and Seasonal Albedo data set from the National Oceanic and Atmospheric Administration (NOAA) [13]. The Matthew vegetation map has a spatial resolution of 1 degree. This is considerably lower than other available sources but Matthews data is derived from approximately 100 published sources complimented by satellite data. Other vegetation maps rely primarily on only one source.

In the Amazon region, there are six main vegetation types documented by Matthews. This study focuses primarily on these six types. Figure(4.1) shows the Matthews vegetation index image for the Amazon region. The six vegetation types are as follows:

- 1. Tropical evergreen rainforest, mangrove forest

- 9. Tropical/subtropical drought-deciduous forest

- 12. Xeromorphic forest/woodlands

- 23. Tall/medium/short grassland with 10-40% woody tree cover

- 24. Tall/medium/short grassland with < 10% woody tree cover or tuft-plant cover

- 25. Tall/medium/short/grassland with shrub cover

Six different areas in the Amazon were chosen so that study could be made of each of these different types of vegetation. Table(4.1) gives the coordinates for these regions and Figure(4.1) shows where they are located in reference to the map.

4.2   Method

Once the regions for study have been selected using the Matthews Vegetation Map, it is necessary to extract the same areas from both NSCAT and TRMM images and compare the data. This method is not without limitations. NSCAT and TRMM images have different resolutions and were created over different time periods. This

44

Region	Upper Right corner:Lat,Lon	Lower Left Corner:Lat,Lon	Veg Type
region 1	-8.5 , -60.5	-3.5 , -55.5	Type 1
region 2	-24.5 , -51.5	-21.5 , -48.5	Type 9
region 3	-11.5 , -41.5	-8.5 , -38.5	Type 12
region 4	-16.5 , -56.5	-13.5 , -55.5	Type 23
region 5	-6.5 , -44.5	-4.5 , -41.5	Type 24
region 6	-22.5 , -55.5	-21.5 , -53.5	Type 25

Table 4.1: Vegetation Training Region Coordinates and Descriptions

study assumes a low temporal variability between the time periods that the two satellites were in operation.

NSCAT Amazon images were created from data taken during Julian Days (JD) 98-111, 1997. SIRF for NSCAT enhances resolution from 25 km to roughly 5 km and creates $\mathcal{A}$ and $\mathcal{B}$ images for both vertically-polarized and horizontally-polarized σ^o measurements. TRMM was not yet in operation when the NSCAT data was taken but assuming that the seasonal response of the region will be similar from year to year, the TRMM images were created using data collected over the month of April, 1998. SIRF for TRMM enhances the resolution to roughly 1 km. This indicates that if comparisons are to be made between TRMM images and NSCAT images, the data collected by TRMM needs to be spatially averaged. Figures (4.2), (4.3) and (4.4) show the NSCAT V-Pol $\mathcal{A}$ image, the NSCAT H-Pol $\mathcal{A}$ image and the TRMM image created for this study.

Seven different parameters of the Ku-band σ^o are studied using these images. There are five different variables readily at hand from the SIRF products: NSCAT $\mathcal{A}$H, NSCAT $\mathcal{B}$H, NSCAT $\mathcal{A}$V, NSCAT $\mathcal{B}$V, and TRMM $\mathcal{A}$H. Two other variables that have been found useful in polar ice studies and may prove useful in vegetation studies are known as the copol ratios. Copol $\mathcal{A}$ is equal to (NSCAT $\mathcal{A}$V - NSCAT$\mathcal{A}$H) . Copol $\mathcal{B}$ is equal to (NSCAT $\mathcal{B}$V - NSCAT $\mathcal{B}$H) . These two variables are only used with NSCAT data. These seven variables are compared using one or two dimensional histograms to determine how similar/dissimilar the response is between vegetation
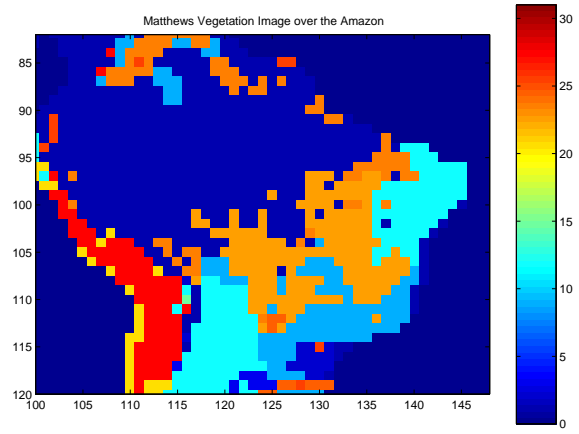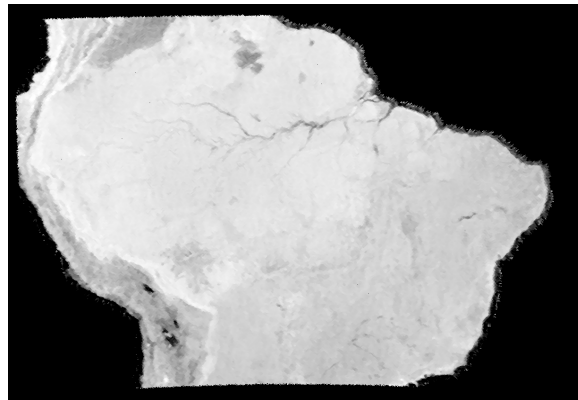
Figure 4.1: Matthews Vegetation Map for the Amazon

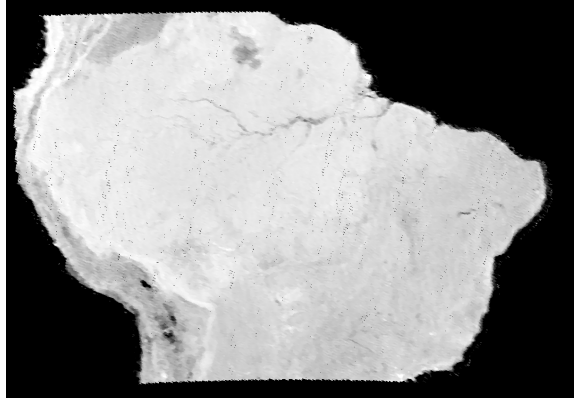Figure 4.2: A sample V-pol NSCAT SIRF image over the Amazon basin during April,1997

Figure 4.3: A sample H-pol NSCAT SIRF image over the Amazon basin during April,1997
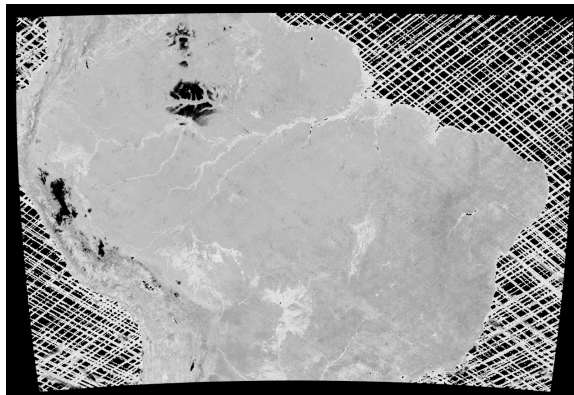
Figure 4.4: A sample TRMM PR SIR image over the Amazon basin during April,1998

types.

4.3   Results

The results of this study are interesting and open the doors to the possibility of vegetation classification using a multivariate method. The first study completed with this data was to create two dimensional histograms using the data collected from each vegetation type. The obvious variable comparisons (the two axis of the histogram) were to compare TRMM $\mathcal{A}$H with NSCAT $\mathcal{A}$H and to compare TRMM $\mathcal{A}$H with NSCAT $\mathcal{A}$V. The results from these comparisons are shown in Figures (4.7) through (4.8) and (4.5) through (4.6), respectively. A close examination of these histograms shows that it may be possible to differentiate between certain vegetation types with only two variables. For example, an examination of Figure (4.5) and Figure (4.6) shows that using only NSCAT $\mathcal{A}$V and TRMM $\mathcal{A}$H, it would be a simple problem to classify the evergreen rain forest from the grassland. Other classifications are more difficult (differentation between some types is impossible), but may still be possible.

The study was extended to evaluate which of the seven variables used in this study would be valuable in classification of different vegetation types. Figures (4.9) through (4.14) show one dimensional plots showing a scaled probability density of the different vegetation types for each of the seven variables. An examination of these would show that several of them are rather useless for vegetation differentation; for example, neither copol ratio can be used sucessfully to classify any type of vegetation. Figure(4.11), a plot using NSCAT $\mathcal{A}$V, shows an excellent distribution between type except for deciduous forest and shrubland, which occupy the same space. Xeromorphic forest and grassland with 10-40% tree cover appear too close in their distribution too be uniquely determined. In Figure (4.10), a plot of $\mathcal{B}$H shows that these two difficulties in classification types can be overcome using an additional variable. Tables (4.2) through (4.6) show for each different variable used, the means and variances of the distributions for each vegetation type. This information maight eventually be helpful in determining an algorithm that can uniquely classify the vegetation types using all five useful variables.

4.4 Summary and Conclusions

In this study, TRMM and NSCAT Amazon images were used to complete a study of Ku-band backscatter from different vegetation types. It was discovered through the course of this study that many vegetation types could be uniquely determined using only two variables: NSCAT $\mathcal{A}$V and TRMM $\mathcal{A}$H. The study was extended to seven possible variables and has shown that it may be possible to uniquely distinguish each vegetation type within an acceptable limit of error using a multivariate algorithm. That is the work of a future study and was not attempted here.
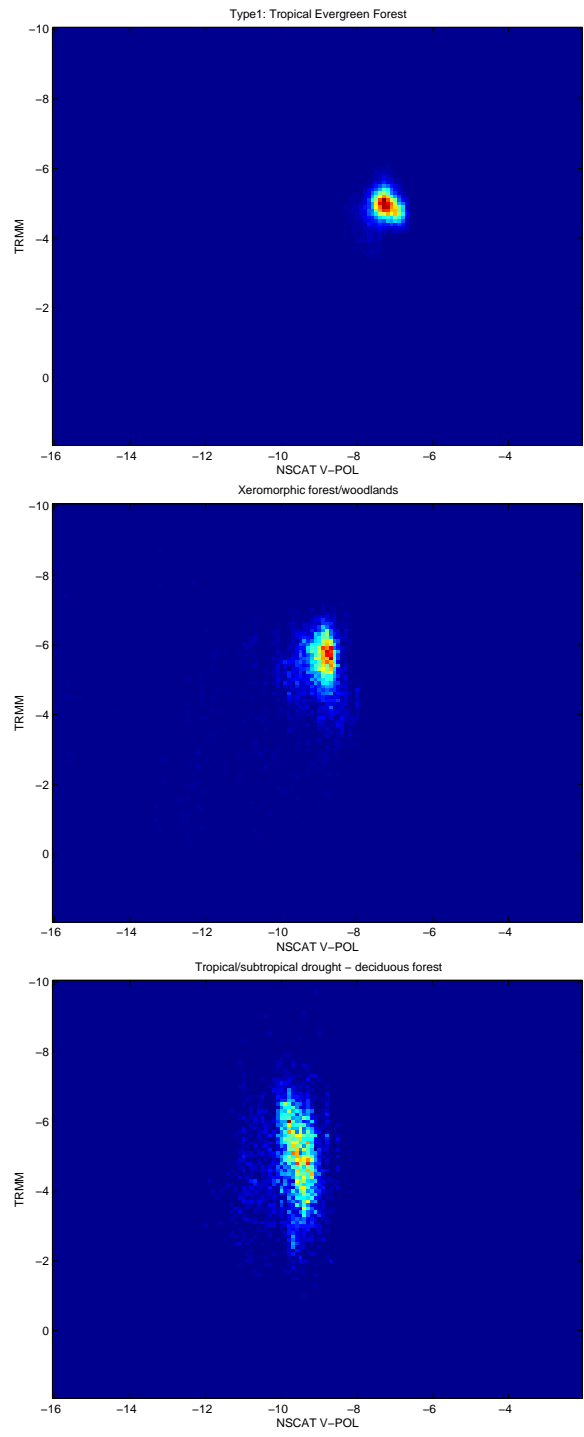
Figure 4.5: A Histogram of TRMM, NSCAT V-pol measurements for Matthews Vegetation Types 1,9,12
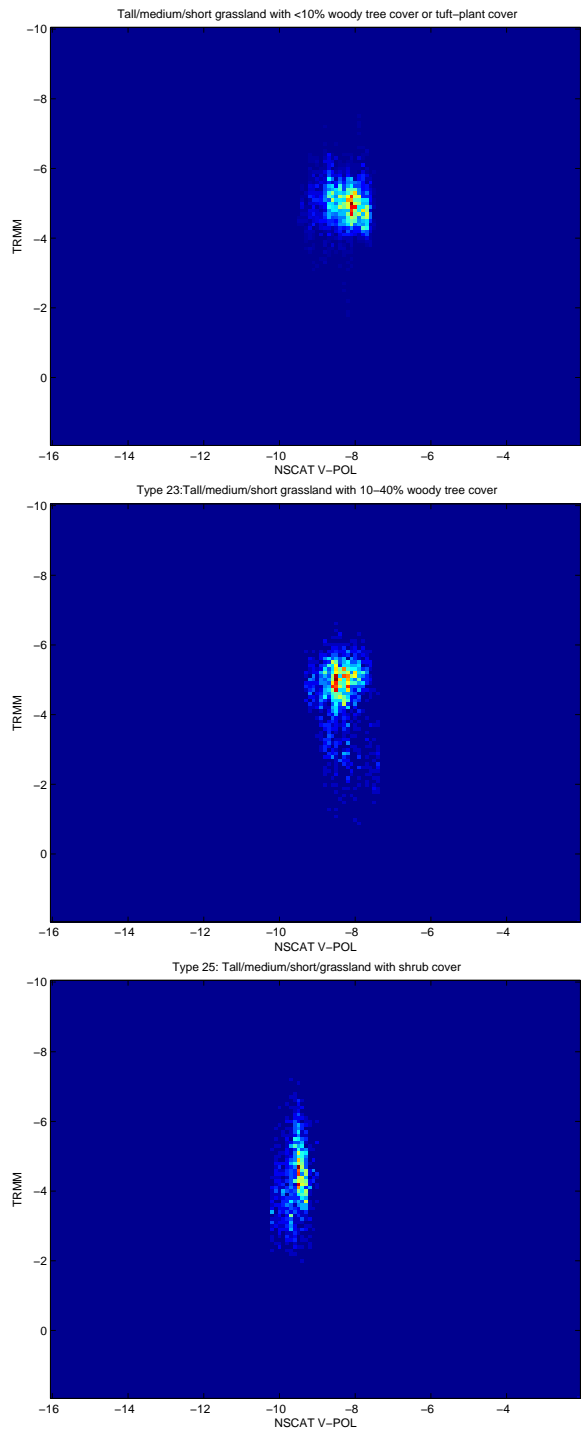
Figure 4.6: A Histogram of TRMM, NSCAT V-pol measurements for Matthews Vegetation Types 23,24,25
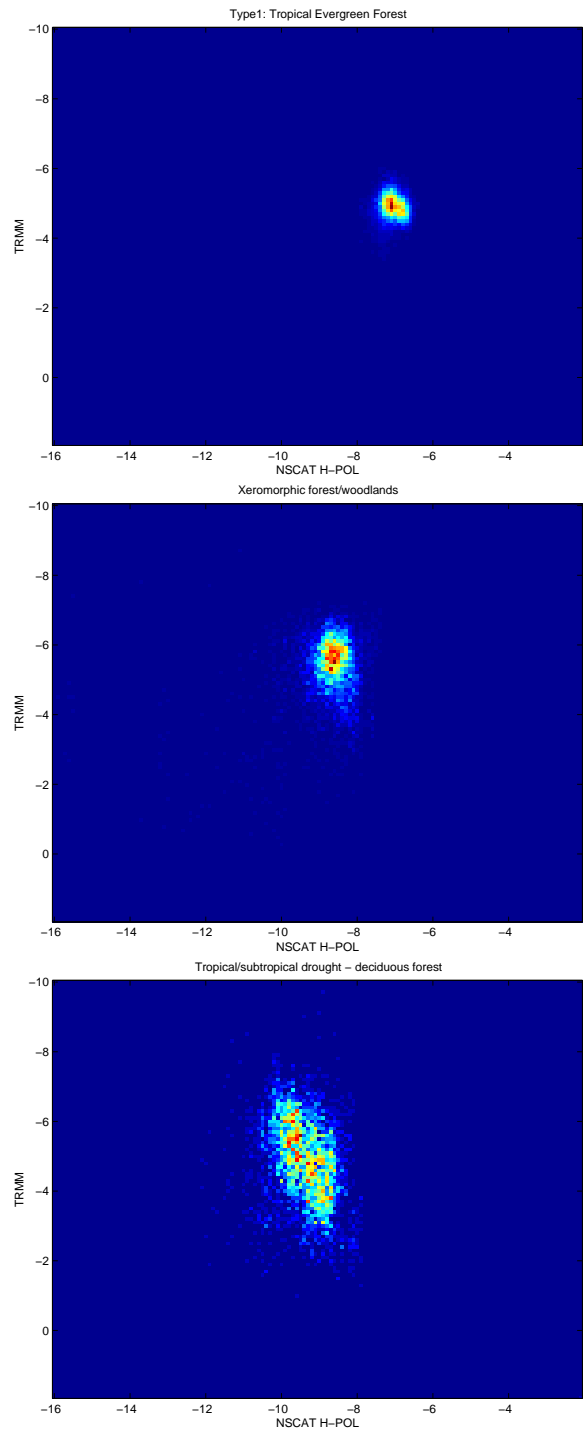
Figure 4.7: A Histogram of TRMM, NSCAT H-pol measurements for Matthews Vegetation Types 1,9,12
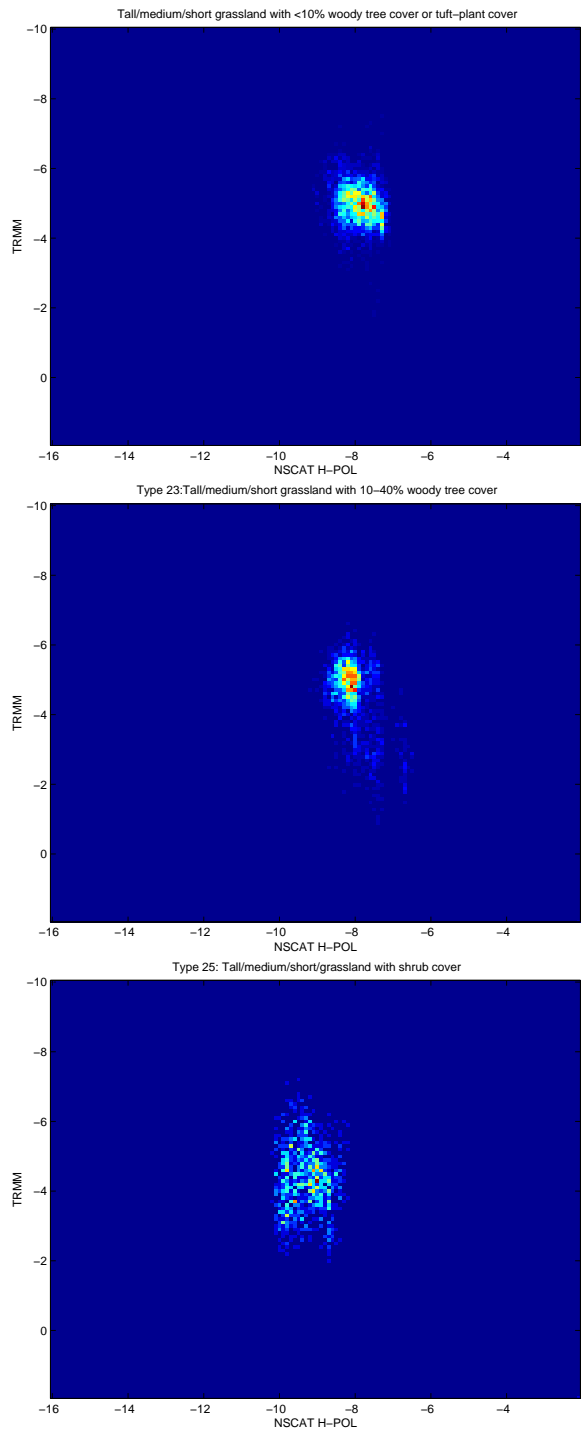
Figure 4.8: A Histogram of TRMM, NSCAT H-pol measurements for Matthews Vegetation Types 23,24,25

Vegetation Type	Mean Value	Variance
Type 1	-0.1173	9.4709e-05
Type 9	-0.1168	1.3737e-04
Type 12	-0.0909	2.5957e-04
Type 23	-0.1234	1.0897e-04
Type 24	-0.1206	7.1367e-05
Type 25	-0.1229	2.6551e-04

Table 4.2: Mean And Variance over NSCAT $\mathcal{B}$V for different vegetation types
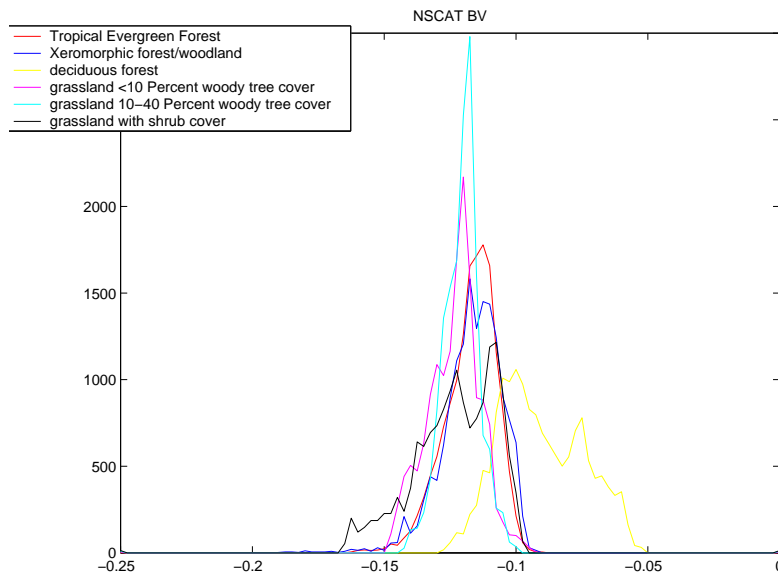
Figure 4.9: Histogram of different vegetation types over NSCAT $\mathcal{B}$V

Vegetation Type	Mean Value	Variance
Type 1	-0.1064	3.353e-04
Type 9	-0.1137	2.8272e-04
Type 12	-0.0932	3.8013e-04
Type 23	-0.1159	2.3941e-04
Type 24	-0.1298	1.9711e-04
Type 25	-0.1426	1.8424e-04

Table 4.3: Mean And Variance over NSCAT $\mathcal{B}$H for different vegetation types
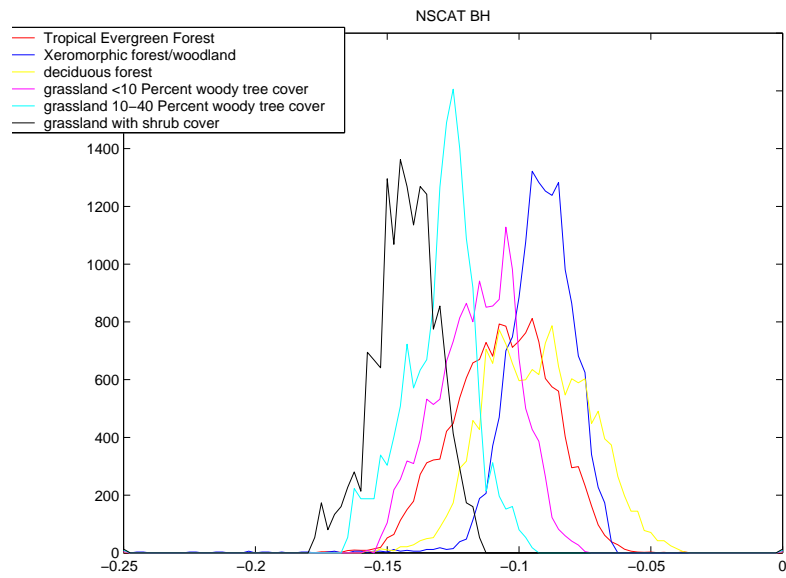
Figure 4.10: Histogram of different vegetation types over NSCAT $\mathcal{B}$H

Vegetation Type	Mean Value	Variance
Type 1	-7.2473	0.1013
Type 9	-8.9953	0.3978
Type 12	-9.5974	0.2247
Type 23	-8.2096	0.1776
Type 24	-8.3268	0.1600
Type 25	-9.5067	0.1072

Table 4.4: Mean And Variance over NSCAT $\mathcal{A}$V for different vegetation types
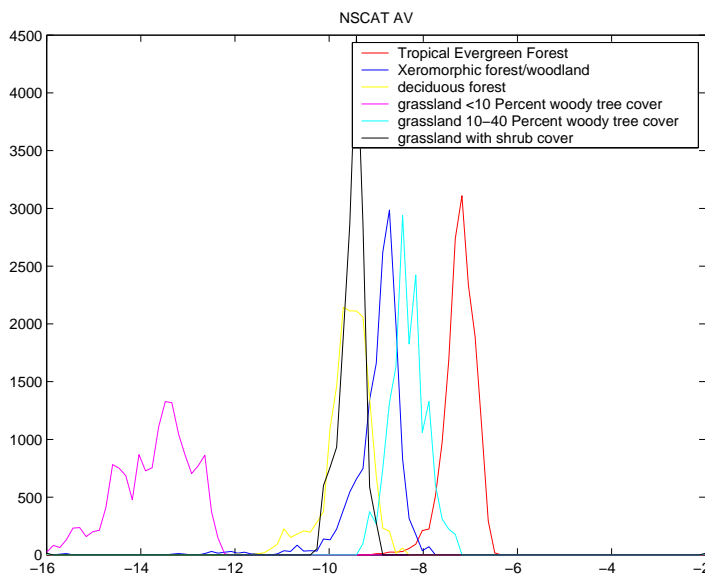
Figure 4.11: Histogram of different vegetation types over NSCAT $\mathcal{A}$V

Vegetation Type	Mean Value	Variance
Type 1	-7.0316	0.0794
Type 9	-8.6440	0.3858
Type 12	-9.3402	0.3517
Type 23	-7.8300	0.1536
Type 24	-8.0064	0.1806
Type 25	-9.2392	0.2517

Table 4.5: Mean And Variance over NSCAT $\mathcal{A}$H for different vegetation types
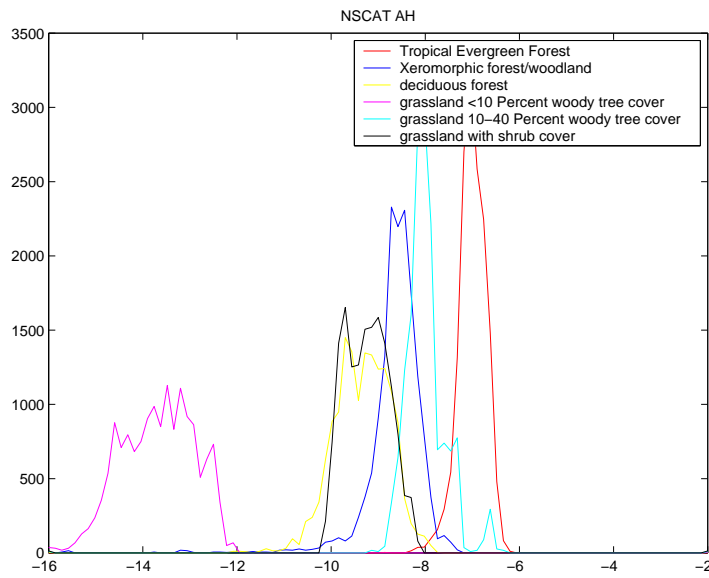
Figure 4.12: Histogram of different vegetation types over NSCAT $\mathcal{A}$H

Vegetation Type	Mean Value	Variance
Type 1	-4.8846	0.1920
Type 9	-5.3788	0.6801
Type 12	-4.8824	1.2695
Type 23	-4.9716	0.2843
Type 24	-4.6500	0.7891
Type 25	-4.3656	0.8241

Table 4.6: Mean And Variance over TRMM $\mathcal{A}$H for different vegetation types
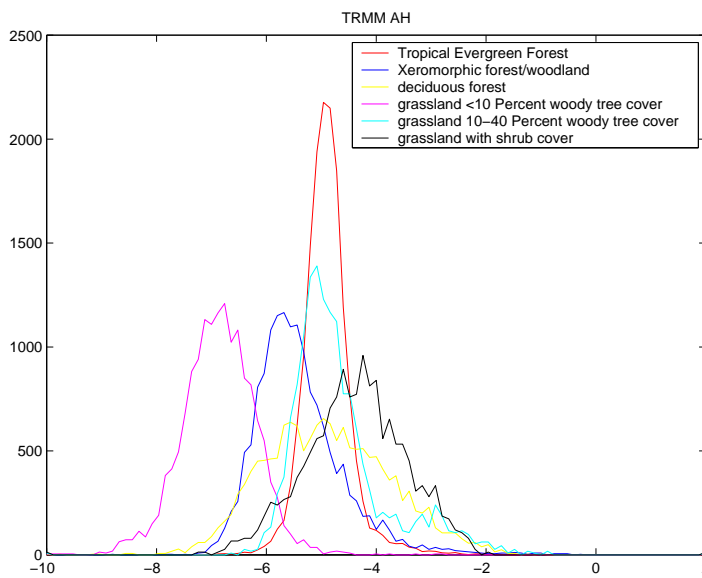
Figure 4.13: Histogram of different vegetation types over TRMM $\mathcal{A}$H
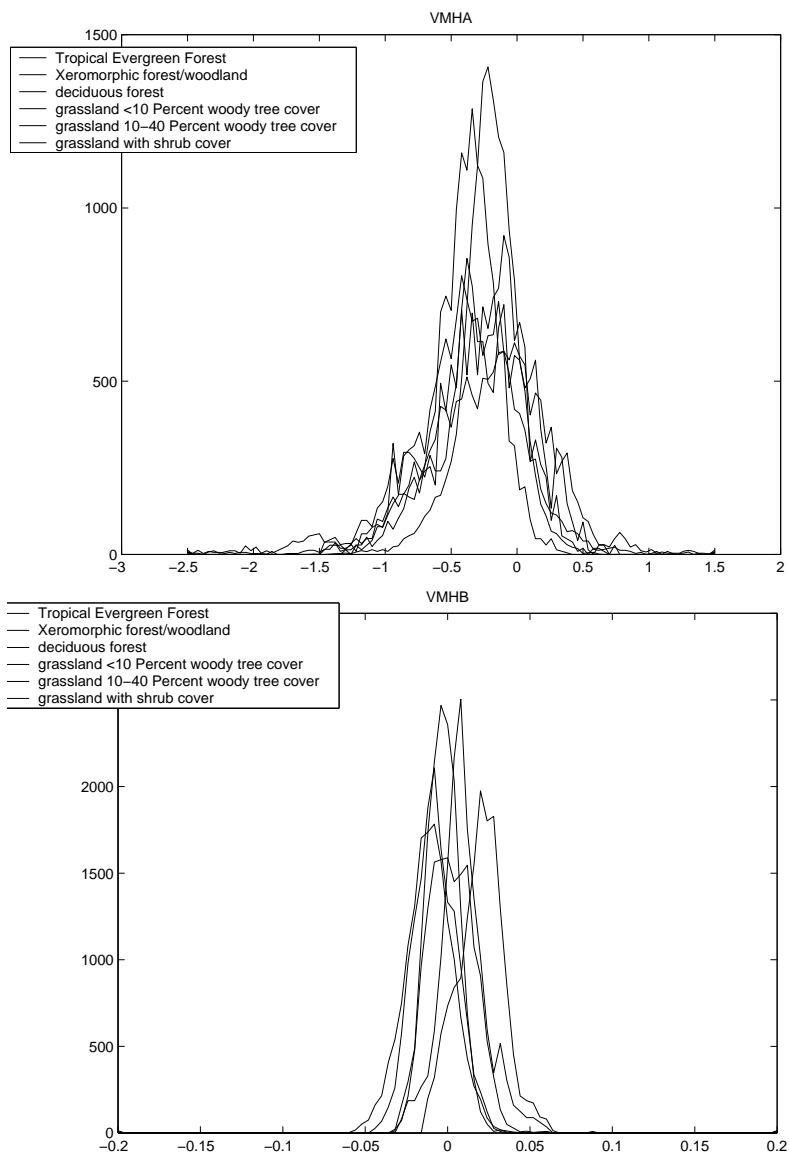
Figure 4.14: Histogram of different vegetation types over COPOL $\mathcal{A}$ and COPOL $\mathcal{B}$

Chapter 5

Tropical Vegetation σ^o vs Incidence Angle Signatures

In this chapter, TRMM PR data is extracted for twelve different areas that correspond to twelve different tropical vegetation types over the month of April, 1999. This data is used to compare the σ^o versus incidence angle relationships for different vegetation types. The differences between volume scattering and surface scattering are discussed in this chapter and conclusions drawn are applied to the TRMM PR study results. Differences in σ^o responses with respect to incidence angle are also compared between regions of different latitude coordinates but similar vegetation type.

5.1 Vegetation and Backscatter

This chapter examines the relationship of σ^o and incidence angle for several different tropical vegetation types. Each vegetation type is labeled with one or two letters. The first letter identifies the type of vegetation that is dominant in the areas while the second letter describes the shape of the land that the vegeation covers. For example, the label "Dm" describes dense tropical evergreen rain forest in a mountainous region: the "D" describes the rain forest and the "m" decribes the mountains. This is important when considering the individual backscatter measurements from a particular region. Backscatter measurement consists of components from volume scattering from the vegetation and surface scattering from the land surface. This will be described in greater detail later in the report as it is valuable to understand the interaction of radar with different vegetation types and the radar backscatter that can be expected at different incident angles.

5.2 Procedure

The intent of this study is to compare the σ^o and incidence angle relationships for several different tropical vegetation types over South America. In order to make this study practical, small areas were chosen for data extraction. With such a small area however, it is important to have as accurate of truth data as possible. For this reason, a higher resolution vegetation map created in 1993 by the Republic of Brazil was chosen rather than lower resolution vegetation maps such as Matthews Vegetation Index or AVHRR vegetation maps. This decision limits the study to the vegetation types found within the boundaries of Brazil but also lends greater confidence to the accuracy of the data and therefore the study.

5.2.1 Vegetation Types and Regions

Using the vegetation map provided by the Republic of Brazil, twelve dominant vegetation types were chosen for this study. Although the map used 24 different classifications for vegetation, those that aren't included in this report were either outside the range of coverage of TRMM or were sparsely represented on the map. The twelve different vegetation types are listed below in Portuguese with rough English translations in parentheses.

- As - Floresta Ombrofila Aberta - Submontana (Open Rain Forest - Hills)

- C - Floresta Estacional Decidual (Decidual Forest)

- Db - Floresta Ombrofila Densa - Terra Biaxis (Dense Rain Forest - Flatland)

- Dm - Floresta Ombrofila Densa - Montana (Dense Rain Forest - Mountains)

- Ds - Floresta Ombrofila Densa - Submontana (Dense Rain Forest - Hills)

- Ea - Estepe - Arborea Aberta (Grassland - little tree cover)

- Ed - Estepe - Arborea Densa (Grassland - heavier tree cover)

- F - Floresta Estacional Semidecidual (Mixed Forest - Evergreen Broadleaf and Deciduous)

- Ld - Vegetacao Lenhosa Oligotrofica

- M - Floresta Ombrofila Mista (Rain Forest - wetlands)

- S - Savana (Savana)

- Sa - Savana - Arborea Aberta (Savana - little tree cover)

The coordinates for the regions chosen from the vegetation map are given in Table (6.1). TRMM PR 2A21 data was extracted over these regions over the month of April, 1999. TRMM PR 2A21 data provides six different measurements for each record, including time, sigma-0, incidence angle, latitude and longitude. It also includes a rain flag that is determined by all five instruments on board TRMM. For the purposes of this study, the rain flag is used to identify which records might be tainted by rain so they can be ignored. This study primarily uses the σ^o and incidence angle data and plot the two values against each other for each record. Using all the data extracted for a region, a relationship between σ^o and incidence angle for a particular vegetation type is determined.

5.2.2 Latitudinal Differences in Vegetation

Data was also extracted for five additional regions in order to make a comparison of similar vegetation at different latitudes. The coordinates for these five regions, as well as the vegetation type, are listed in Table (5.2). It was impossible to compare all twelve major vegetation types because vegetation in the tropics is largely stratified according to latitude. The five regions and vegetation types in Table (5.2) are the only major types over all the different latitudes.

Vegetation Type	Symbol	Region Latitude	Region Longitude
Floresta Ombrofila Aberta	**As**	-5.0	-56.0
Floresta Estacional Decidual	**C**	-15.0	-42.0
Floresta Ombrofila Densa - Terras Baixas	**Db**	-8.0	-68.0
Floresta Ombrofila Densa - Montana	**Dm**	3.0	-64.0
Floresta Ombrofila Densa - SubMontana	**Ds**	0.0	-47.0
Estepe Densa	**Ea**	-10.0	-40.0
Estepe Aberta	**Ed**	-8.0	-41.0
Floresta Estacional Semidecidual	**F**	-23.0	-52.0
Vegetacao Lenhosa	**Ld**	0.0	-69.0
Floresta Ombrofila Mista	**M**	-27.0	-53.0
Savana	**S**	-21.0	-56.0
Savana - Arbrea Aberta	**Sa**	-16.0	-47.0

Table 5.1: Vegetation region coordinates.

Vegetation Type	Symbol	Region 1 Latitude	Region 2 Latitude
Floresta Ombrofila Aberta	**As**	-5.0	-15.0
Floresta Estacional Decidual	**C**	-15.0	-5.0
Floresta Ombrofila Densa - SubMontana	**Ds**	0.0	-6.0
Estepe Densa	**Ea**	-10.0	-3.0
Savana	**S**	-21.0	-11.0
Savana - Arbrea Aberta	**Sa**	-16.0	-6.0

Table 5.2: Region coordinates for latitudinal difference study.

5.3 Results

The results from the above two studies are shown in Figures (5.2) through (5.21). Figures (5.2) through (5.12) show the relationship between σ^o and incidence for the different vegetation types. Figure (5.13) shows a comparison plot of the same. Figures (5.16) through (5.21) show the results of the latitudinal difference study.

5.3.1 Discussion of Results

Figure (5.13) is a plot of σ^o versus incidence angles for the twelve different vegetation types. For the purpose of this discussion, the incidence angles are classfied

into three different intervals: nadir, near-nadir (0-2 degrees), and the remaining range of incidence angles (2-17 degrees). The first interval is shown in Figure (5.14). It can be seen quite clearly that different vegetation types on the average, have differing σ^o values at nadir. Vegetation types with less of a canopy have a higher backscatter measurement than other vegetation types. Figure (5.15) shows the second incidence angle range. What is most intriguing about this range is the rate that the σ^o values decreases as the incidence angle increases. The last interval shows how σ^o behaves as the incidence angle advances from the near-nadir range. It is shown that while some vegetation types level off at a particular value of σ^o, the vegetation types with less of a canopy seem to continue to decrease as the incidence angle increases. This section endeavors to explain these phenomena. The backscatter measurement over vegetation is dependent upon many different variables but can be expressed as a function of just three: surface scattering, volume scattering and what can be described as interaction scattering.

$$\sigma^o(\theta, \phi) = [1 - C(\theta, \phi)] * \sigma^o_{bare} + C(\theta, \phi) * \sigma^o_{can} + [1 - C(\theta, \phi)] * \sigma^o_{int}(\theta, \phi) \qquad (5.1)$$

In equation (6.1), $C(\theta,\phi)$ is the fraction of the illuminated area that is vegetation covered. When this fraction approaches unity, the measured σ^o approaches σ^o_{can}. The σ^o_{bare} and σ^o_{int} represent the backscatter coefficient of the exposed surface and that of the interaction between vegetation and the surface. Figure (5.1) demonstrates these three components. The latter of these components, interaction scattering, is difficult to quantify and not essential to the present discussion so will be ignored. The difference between surface scattering and volume scattering however, will be reviewed with the hope of application towards the results of the TRMM data study. It was for this reason that the regions were labeled with two different letters - one describing the vegetation and the other describing the surface.

- Surface Scattering: Surface scattering as a function of incidence angle is highly dependent upon two factors: the roughness of the surface and the dielectric constant. The roughness of the surface is measured in comparison to the wavelength (λ). For a smooth surface (in comparison to λ), the backscatter measurement is

high at nadir and rapidly decreases with incidence angle. As the surface roughness increases, the backscatter response is not as peaked at nadir and decreases much less quickly with an increase in incidence angle. Most land surfaces can be described as medium to rough surfaces. The dielectric constant in land is dependent largely of the soil moisture content and less on the soil composition. As the moisture content of the land increases, so does the backscatter measurement.

- Volume Scattering: Volume scattering is caused mainly by dielectric discontinuities within a volume. Since this discontinuities are random, the backscatter is isotopic for a pure volume scatterer. As a function of incidence angle, volume scattering should yield a relatively uniform response for most mediums. For the incidence angle range of TRMM PR, the volume scattering should yield a completely uniform response with respect to incidence angle.

With a review of the effects of volume scattering and surface scattering, the results obtained by the study of TRMM PR data for different vegetation types are much clearer. In Figure (5.14) , the near nadir σ^o values for different vegetation types are shown. At nadir, σ^o is a just as much a factor of surface scattering as volume scattering, no matter what the vegetation type. This is because at nadir, the incident signal is in most cases normal to the surface beneath the vegetation canopy. This will result in a large spectral reflection. This is true only when the surface beneath the canopy is relatively flat. Standing water under the vegetation canopy would provide a strong spectral response at incidence angles near nadir because of the surface type. Other factors which affect the spectral response are the electrical properties of the surface. Assuming the surface in the regions studied to be relatively flat unless otherwise indicated ('m' indicates a mountainous region), the differences observed between vegetation type can therefore be attributed almost completely to the average dielectric constant of the vegetation canopy and also of the surface. These constants are most affected by the amount of soil moisture for less canopied areas and the amount of moisture in the foliage for more canopied areas. It can only be assumed that

the moisture content in the regions that display a higher nadir σ^o measurement, and for other areas covered by these types of vegetation, contain a higher moisture content. Reviewing the phenomena displayed in intervals two and three, it is obvious that different vegetation types exhibit either surface scattering characterisitcs or volume scattering characteristics. The backscatter value from dense tropical rain forest (Dm) falls quickly from its value at nadir to a value that is maintained as incidence angle increases. These characteristics are due to a dominant level of volume scattering. The value $C(\theta,\phi)$ used in Equation (6.1) for this vegetation type is close to unity. On the other extreme, the backscatter value from a region of Savana falls from it value at nadir and decreases at almost a constant slope as incidence angle increases. This is highly characteristic of surface scattering. The other vegetation types studied exhibit more or less of the characteristics of the two extremes mentioned above and correspondingly has a different value of $C(\theta,\phi)$.

5.3.2 Latitudinal Differences in σ^o Over Similar Vegetation Types

Figures (5.16) through (5.21) show the results of the latitudinal difference study. Each vegetation region shows an expected result. As the region moves farther from the equator, there is less moisture in the area. This is shown in two different ways; either the σ^o/incidence anlge response is altogether lower for a lower latitude or the curve actually changes shape and displays more of a surface scattering characteristic than a region of the same vegetation type that lies closer to the equator. For example, Figure (5.17) show the latitudinal study for decidual forest. At -15°latitude, the curve follows that of the response at -5°latitude but the response is anywhere from 1 to 2 dB lower. Figure (5.21) shows the response for sparsely wooded savana. The response at -6°latitude shows much more of a volume scattering response than the response at -16°latitude. This indicates a higher fraction of wooded cover which implies more moisture in the area.

5.4 Conclusions

TRMM PR data was extracted over several different regions, each representing a different tropical vegetation type. This data was examined as to their σ^o versus incidence angle relationships and it was discovered that each vegetation type exhibited a different characteristic. After a review of the characteristics of surface scattering and volume scattering, is it proposed that TRMM PR data exhibits a distinct combination of surface scattering and volume scattering signatures according to vegetation type. This study has also compared similar vegatation types at different latitudes and has discovered differences in the incidence angle dependence of σ^o that can only be accounted for by the amount of moisture in the area. TRMM PR data might also prove useful in the study of soil/vegetation moisture content given these results.
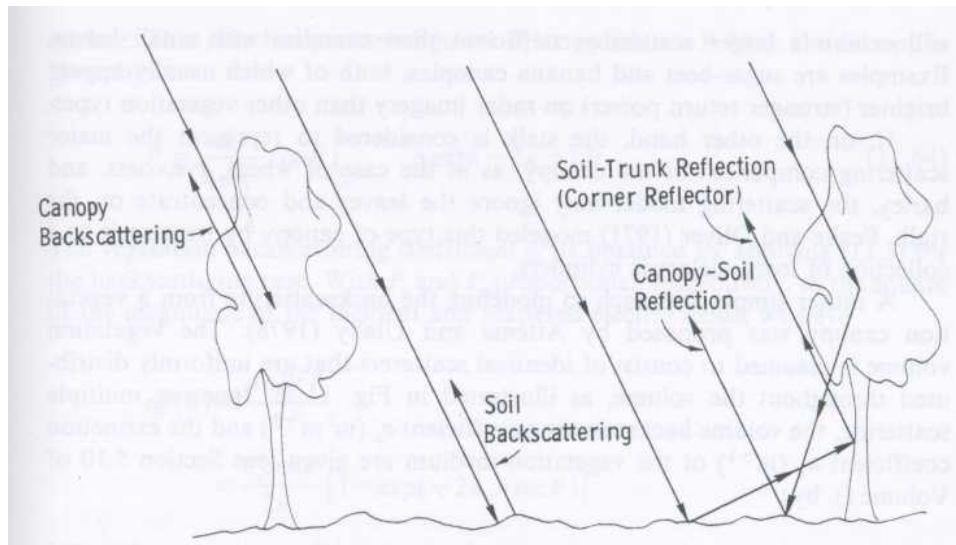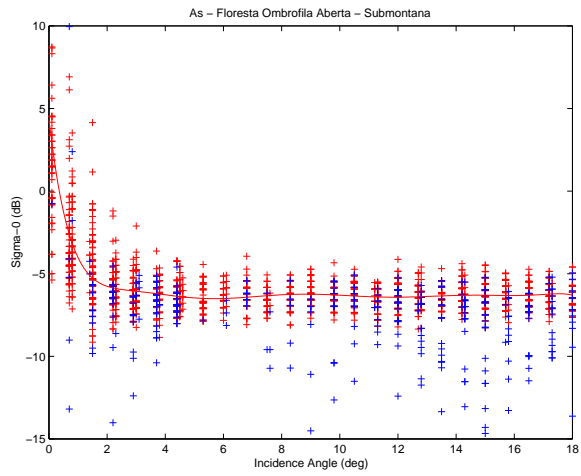
Figure 5.1: Three components of backscatter

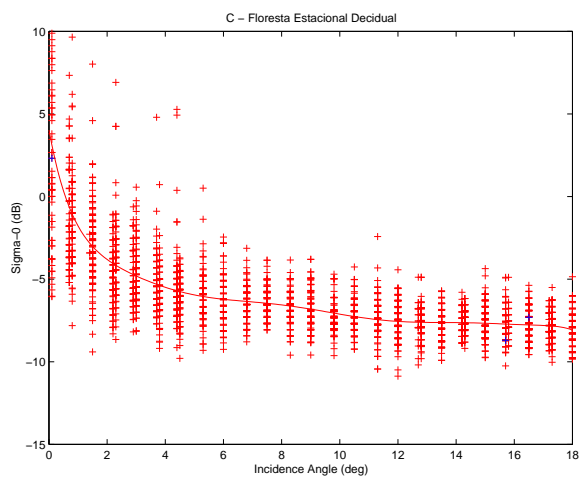Figure 5.2: Sigma-0 vs incidence angle for Floresta Ombrofila Aberta

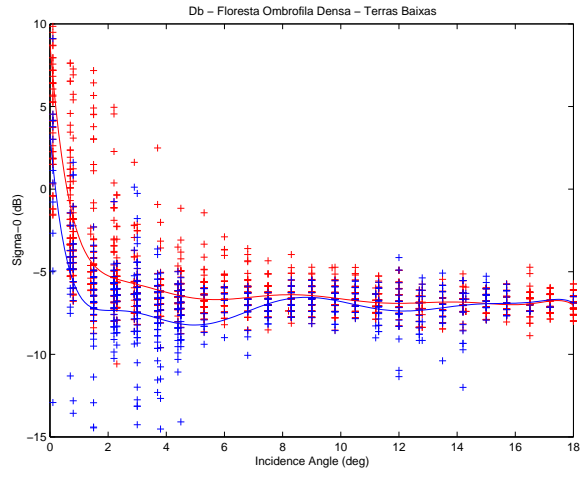Figure 5.3: Sigma-0 vs incidence angle for Floresta Estacional Decidual

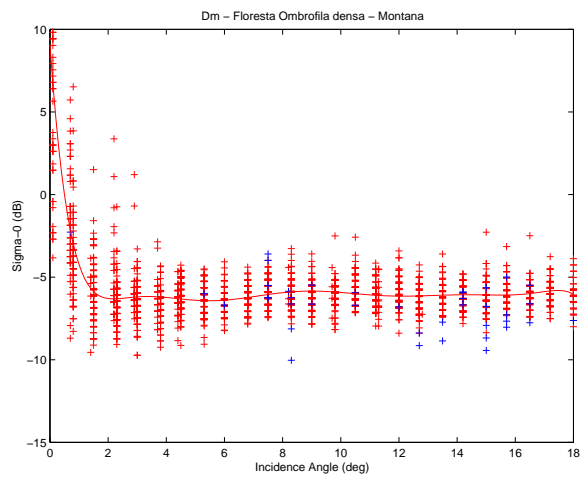Figure 5.4: Sigma-0 vs incidence angle for Floresta Ombrofila Densa - Terra Biaxis

Figure 5.5: Sigma-0 vs incidence angle for Floresta Ombrofila Densa - Montana
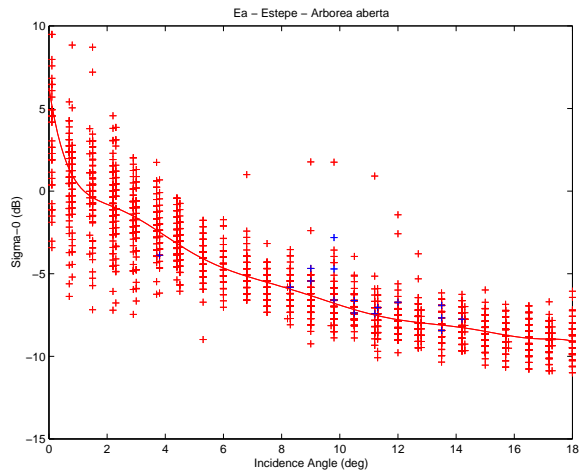
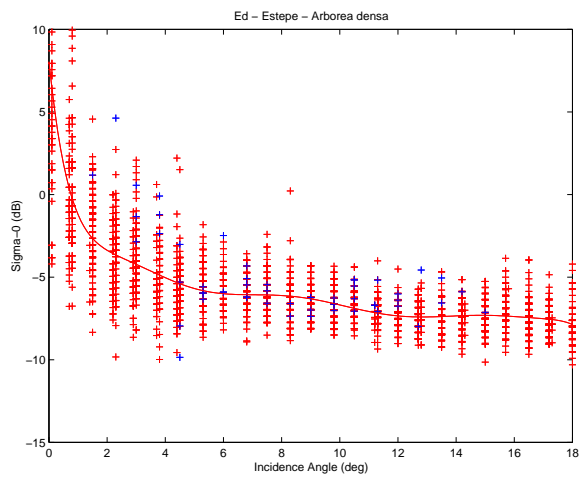Figure 5.6: Sigma-0 vs incidence angle for Estepe -Arborea Aberta

Figure 5.7: Sigma-0 vs incidence angle for Estepe - Arborea Densa
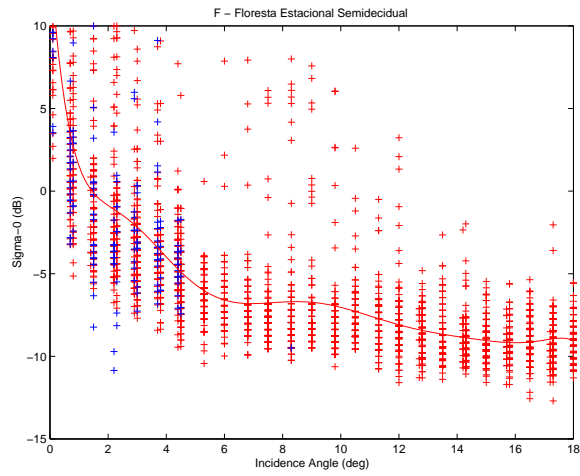
Figure 5.8: Sigma-0 vs incidence angle for Floresta Estacional Semidecidual
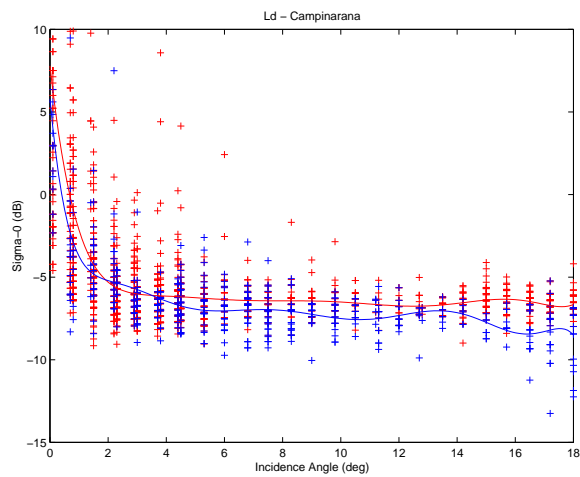
Figure 5.9: Sigma-0 vs incidence angle for Vegetacao Lenhosa
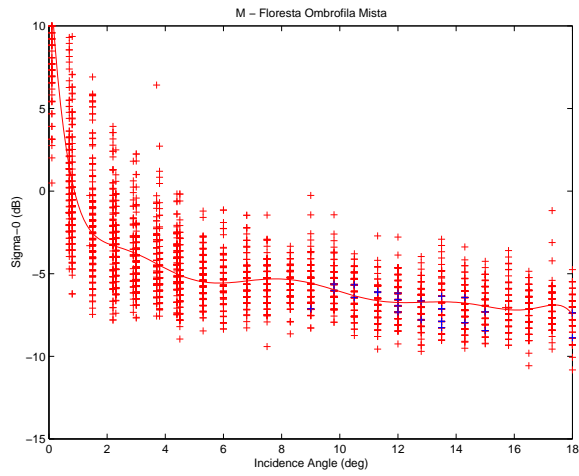
Figure 5.10: Sigma-0 vs incidence angle for Floresta Ombrofila Mista
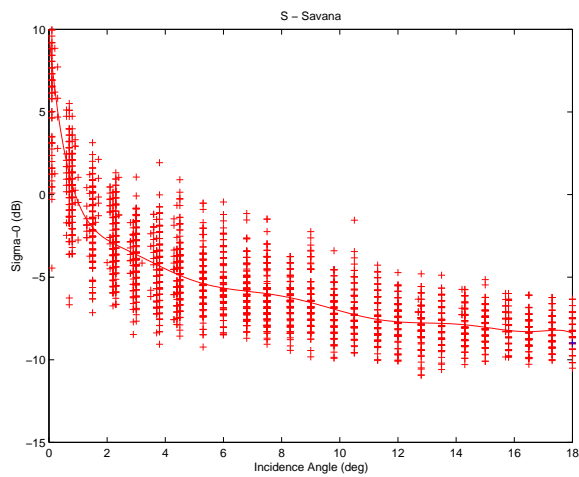
Figure 5.11: Sigma-0 vs incidence angle for Savana
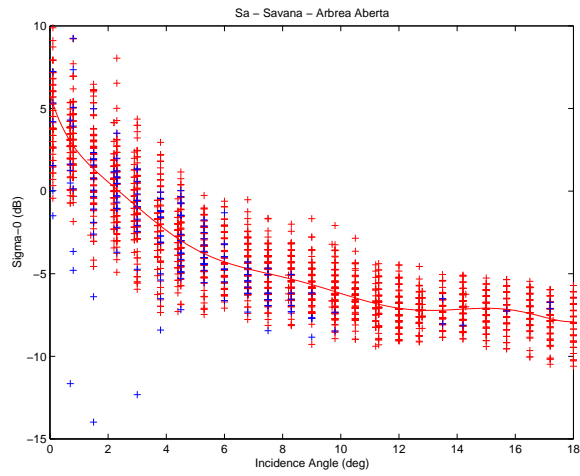
Figure 5.12: Sigma-0 vs incidence angle for Savana - Arborea Aberta
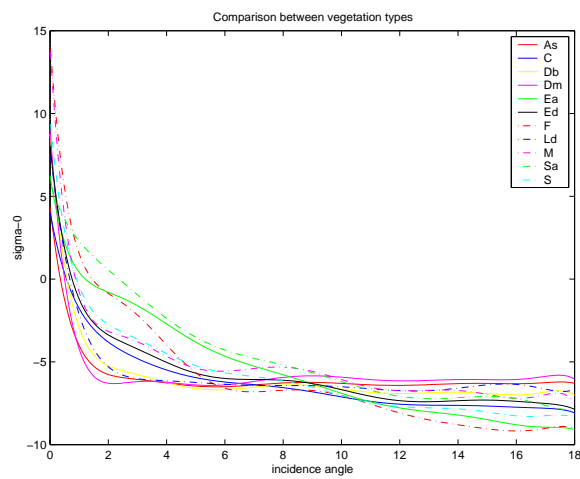
Figure 5.13: Sigma-0 vs incidence angle for different tropical vegetation types.
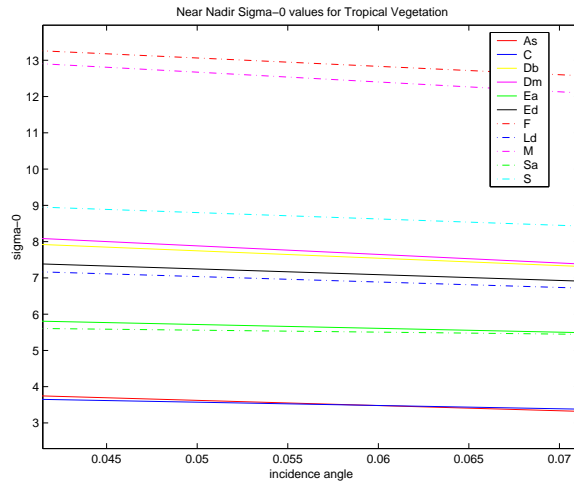
Figure 5.14: Near-nadir sigma-0 measurements for different vegetation types.
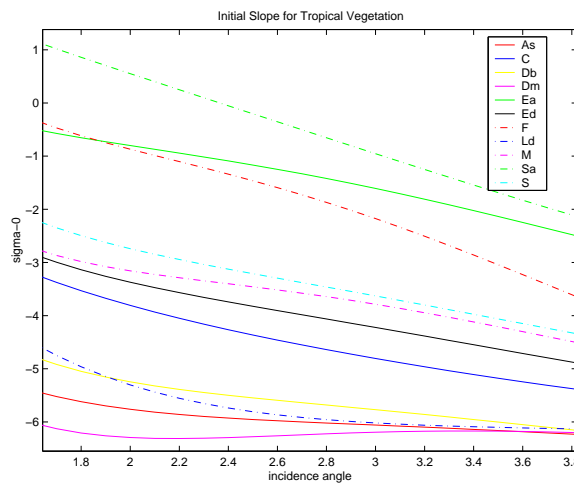
Figure 5.15: Low incidence angle sigma-0 measurements for different vegetation types

Figure 5.16: Sigma-0 vs incidence angle for different latitudes:Floresta Ombrofila Densa - Aberta

Figure 5.17: Sigma-0 vs incidence angle for different latitudes: Floresta Estacional Decidual
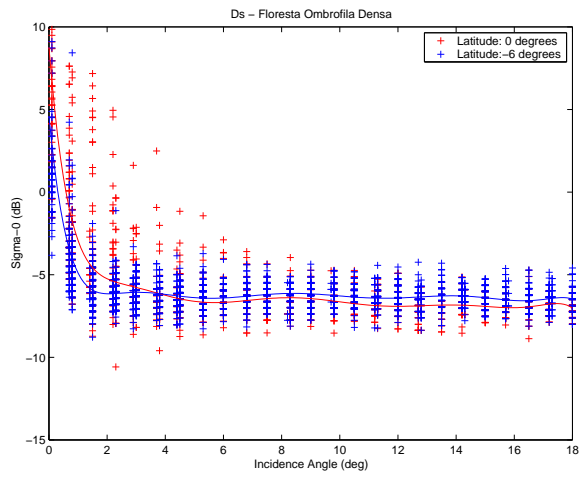
Figure 5.18: Sigma-0 vs incidence angle for different latitudes: Floresta Ombrofila Densa
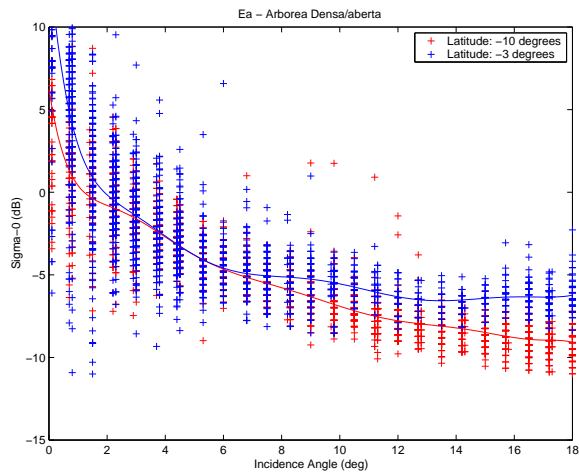
Figure 5.19: Sigma-0 vs incidence angle for different latitudes: Estepe - Arborea Aberta
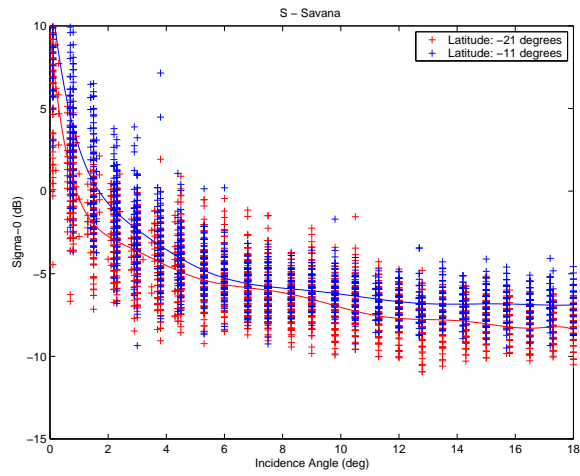
Figure 5.20: Sigma-0 vs incidence angle for different latitudes: Savana

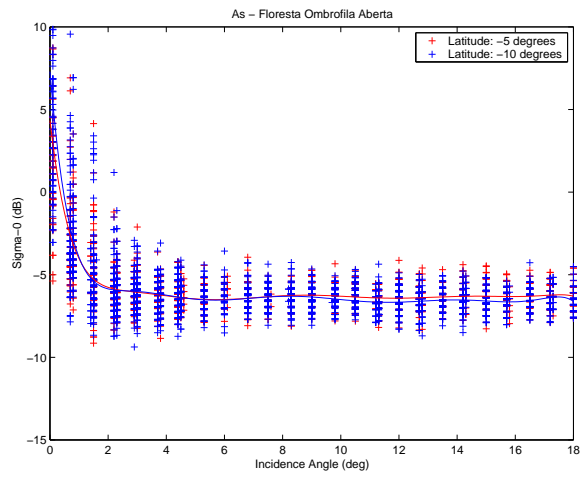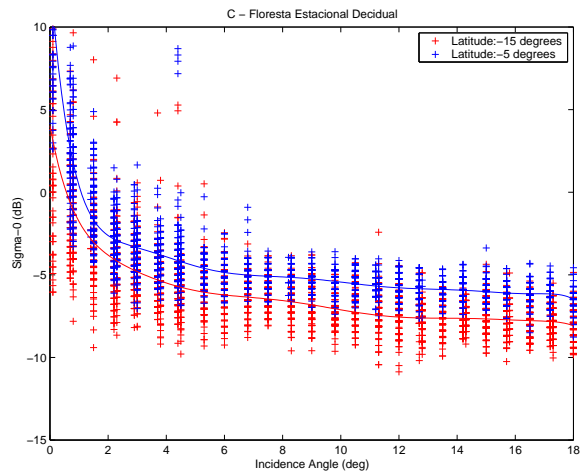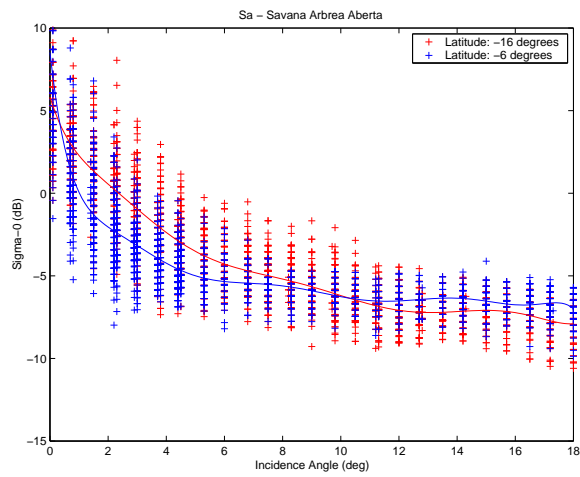

Figure 5.21: Sigma-0 vs incidence angle for different latitudes: Savana - Arborea Aberta

Chapter 6

Effects of Time of Day on σ^o Measurements of Tropical Vegetation

The study of vegetation over the earth, esspecially over the equatorial regions, is important to global weather and climate models. Areas such as vast as the equatorial rain forests greatly affect the weather in the tropics, the amount of moisture in the air and the amount of oxygen produced. These factors have an effect on the global climate and weather models.

Backscatter measurements collected by the Tropical Rain Mapping Mission Precipitation Radar(TRMM PR) are used in this chapter to explore the effects the time of day has on σ^o measurements. TRMM PR is used because of it's high nominal resolution (4 km) and low incidence angle range (nadir to 17°). The low incidence angle range makes this study interesting as data of this type had not been available before the launch of TRMM. Chapter 2 describes TRMM and TRMM PR in greater detail.

This chapter initially gives some background on vegetation and scattering theory and then examines the procedure of this study. TRMM PR data is extracted for twelve different areas that correspond to twelve different tropical vegetation types over the month of April, 1999. This data is used to compare the σ^o vs. incidence angle relationships for different time blocks during a 24 hour period. Lastly, the results of this study are examined in detail.

6.1 Vegetation and Backscatter

This chapter examines the dependence (or independence) of the σ^o/incidence angle relationship for various tropical vegetation types on time of day. Radar backscatter from vegetation is a function of several variables but can be expressed as a function of just three: surface scattering, volume scattering and interaction scattering.

$$\sigma^o(\theta, \phi) = [1 - C(\theta, \phi)] * \sigma^o_{bare} + C(\theta, \phi) * \sigma^o_{can} + [1 - C(\theta, \phi)] * \sigma^o_{int}(\theta, \phi) \qquad (6.1)$$

In the above equation, $C(\theta, \phi)$ is the fraction of the illuminated area that is vegetation covered. When this fraction approaches unity, the measured σ^o approaches σ^o_{can}. The σ^o_{bare} and σ^o_{int} represent the backscatter coefficient of the exposed surface and that of the interaction between vegeation and the surface. Figure (5.1) demonstrates these three components. The latter ofthese components, interaction scattering, is difficult to quantize and not essential to the present discussion so will be ignored. This chapter deals with the possible difference in backscatter that might exist at different times throughout a given 24 hour period. These differences would have to be a function of both surface scattering and volume scattering and can be explained with naturally occuring phenomena that would affect one or both of these components. Volume scattering is caused mainly by dielectric discontinuities within a volume, such as leaves, branches and other plant growth. The backscatter measurement is also affected by the effective dielectric constant of the medium, which is directly associated with the amount of moisture in the medium. Surface scattering has a similar relationship between the amount of moisture in the soil and the σ^o measurement. It is possible that these factors do have a dependence on time of day and therefore the possibility exists that σ^o has a dependence on what time of day the measurement is taken.

6.2 Procedure

The intent of this study was to compare the σ^o/incidence angle relationship for different times during a 24 hour period over several different vegetation types. TRMM PR 2A21 data was extracted over the month of April, 1999 from 12 different

regions, each region corresponding to different vegetation type. These regions were chosen from a high resolution vegetation map created in 1993 by the Republic of Brazil. The decision to use this map limits the study to the vegetation types found within the boundaries of Brazil but lends greater confidence to the accuracy of the data and therefore, the study.

6.2.1 Vegetation Types and Regions

Using the vegetation map provided by the country of Brazil, twelve dominant vegetation types were chosen for this study. Although the map used 24 different classifications for vegetation, those that aren't included in this chapter were either outside the range of coverage of TRMM or were so sparsely represented on the map that comparison of these areas with TRMM data seemed pointless. The twelve different vegetation types are listed below in Portuguese with rough English translations in parentheses.

- As - Floresta Ombrofila Aberta - Submontana

- C - Floresta Estacional Decidual

- Db - Floresta Ombrofila Densa - Terra Biaxis

- Dm - Floresta Ombrofila Densa - Montana

- Ds - Floresta Ombrofila Densa - Submontana

- Ea - Estepe - Arborea Aberta

- Ed - Estepe - Arborea Densa

- F - Floresta Estacional Semidecidual

- Ld - Vegetacao Lenhosa Oligotrofica

- M - Floresta Ombrofila Mista

- S - Savana

- Sa - Savana - Arborea Aberta

The coordinates for the regions chosen from the vegetation map are given in Table (6.1).

6.2.2 TRMM PR Data and Scan Time

TRMM PR 2A21 data provides six different measurements for each record, including time, sigma-0, incidence angle, latitude and longitude. It also includes a rain flag that is determined by all five instruments on board TRMM. For the purposes of this study, the rain flag is used to identify which records might be tainted so they can be ignored. This study primarily uses the σ^o, incidence angle(θ) data and scan time and plots the two values σ^o and θ against each other for each record in the data set. These records are divided into three hour blocks according to the scan time, which is measured in UTC seconds. In order to determine local time, it is necessary to shift the UTC time three or four hours, depending on the longitudinal location of the region. Using all the data extracted for a region, a relationship between σ^o and incidence angle for a particular three hour period is determined.

6.3 Results

The results for this study are shown in Figures (6.1) through (6.12). Each figure show the results for a different vegetation type and is divided into two subfigures. The upper subfigure shows the results for each three hour block of time. The individual data points are plotted, as well as a best-fit approximation to the data. The lower subfigures show a comparison between the different time blocks. Figures (6.13) through (6.23) show a second order least squares fit to the data above 5°for each vegetation type. These plots are informative as they allow an examination of the time-of-day responses of each vegetation type at incidence angles away from nadir.

Figures (6.1), (6.3), (6.4), (6.5), (6.10) and (6.9) show the results for vegetation types that have a dense canopy, such as tropical rain forest. The results for this type of vegetation show relatively little variation except for incidence angles near nadir. What variation exists can be ignored because of the the lack of a trend in

84

the differences between time blocks; the variation is not a function of time. Results for other vegetation types, however, do exhibit a smallish trend. Figure (6.11) and (6.12) show the results for regions covered by Savana. The coolest part of the 24 hour cycle (3AM-6AM), the time when the most moisture would present on the surface (dew), is characterized by the lowest σ^o measurements at low incidence angles; while the hottest part of the day (12PM-3PM) is characterized by the highest σ^o return. This phenomenon, however, is observed only at near-nadir incidence angles. An examination of Figures (6.22) and (6.23) show that the σ^o response from angles above 5°exhibit similar tendencies as the response observed from dense canopy. There isn't any particular order or pattern to the response and the results can be ignored. The following discussion attempts to explain these results.

It has been shown that only the areas of Savana show any conclusive results in the time-of-day study; and these at near-nadir incidence angles. These areas of Savana are characterized by a good deal of moisture and vegetation, but not much of a vegetation canopy. In contrast, Estepe has vegetation but is a drier area and the other areas examined in this study have a dense canopy layer.

As shown in Equation (6.1), the backscatter measurement will have a volume scattering component and a surface scattering component. In regions that are dominated by a thick vegetation canopy high above the surface, the surface scattering component is extremely small. At 13.8 GHz, the wavelength of the TRMM PR signal is 2.17 cm; at this length, given the moisture content of most of the forest cover in the Amazon basin, it is doubtful that the penetration depth into the canopy is even a meter. The dense vegetation canopy is "seen" as a solid surface since the backscatter measurement is due almost entirely to volume scattering. At that frequency, the signal do not have occasion to interact with the moisture that collects in the lower levels of the canopy or on the surface below. In areas such as Savana, however, there is a greater surface scattering component to the σ^o measurement and therefore a greater temporal variance is seen. Because of the greater surface scattering component, measurements at near-nadir incidence angles are affected by a collection of moisture, such

as dew, and the backscatter measurement would reflect that temporal change. Although Estepe also has a higher surface scattering component than vegetation types that are dominated by canopy, these areas lack the moisture needed to observe a time-of-day change in σ^o.

6.4 Conclusion

A month's worth of TRMM PR data was extracted over several different regions, each representing a different tropical vegetation type. These data sets were examined as to their σ^o versus incidence angle relationship and its dependence on the time of day. Given the results of this study, it is concluded that for vegetation types that exhibit a large volume scattering component, low incidence angle Ku-band backscatter is almost completely independent of the time of day that the measurement is taken. For vegetation types that exhibit more of a surface scatting component, a small temporal dependence exists.

| Vegetation Type	Symbol	Region Latitude	Region Longitude
Floresta Ombrofila Aberta	**As**	-5.0	-56.0
Floresta Estacional Decidual	**C**	-15.0	-42.0
Floresta Ombrofila Densa - Terras Baixas	**Db**	-8.0	-68.0
Floresta Ombrofila Densa - Montana	**Dm**	3.0	-64.0
Floresta Ombrofila Densa - SubMontana	**Ds**	0.0	-47.0
Estepe Densa	**Ea**	-10.0	-40.0
Estepe Aberta	**Ed**	-8.0	-41.0
Floresta Estacional Semidecidual	**F**	-23.0	-52.0
Vegetacao Lenhosa	**Ld**	0.0	-69.0
Floresta Ombrofila Mista	**M**	-27.0	-53.0
Savana	**S**	-21.0	-56.0
Savana - Arbrea Aberta	**Sa**	-16.0	-47.0

Table 6.1: Vegetation region coordinates.
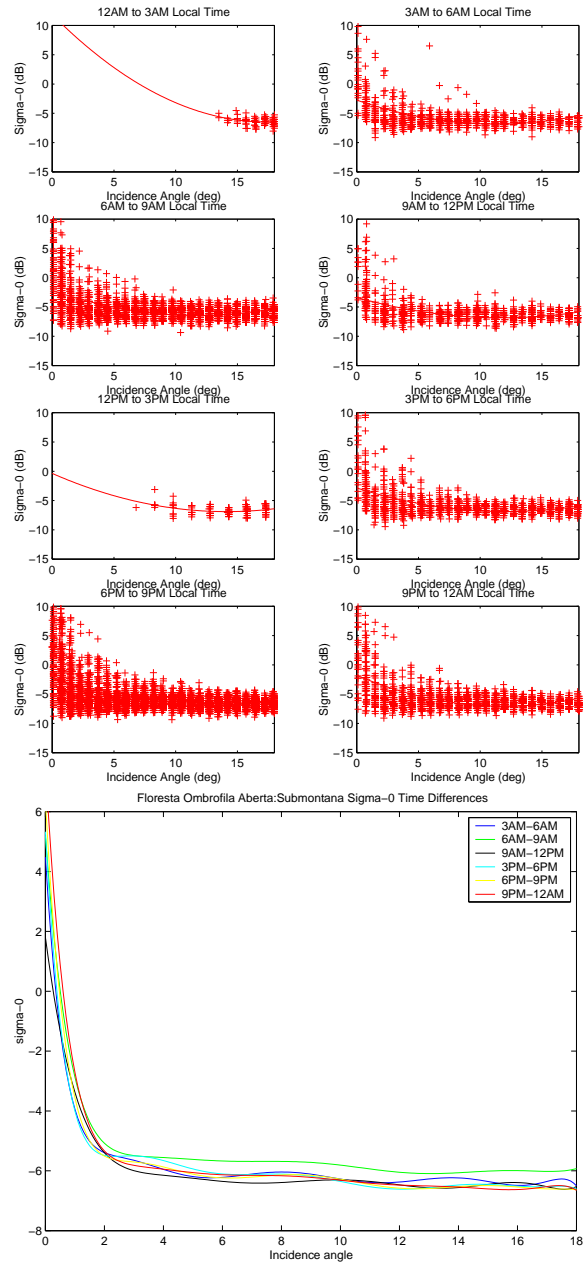
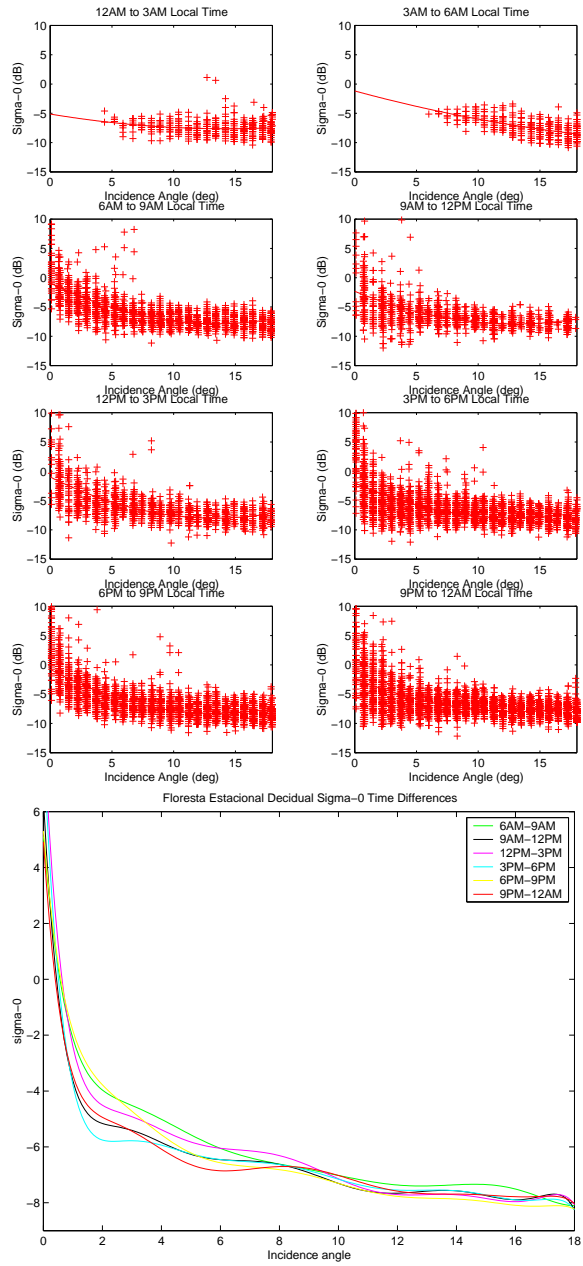Figure 6.1: Sigma-0 vs incidence angle for Floresta Ombrofila Aberta

Figure 6.2: Sigma-0 vs incidence angle for Floresta Estacional Decidual
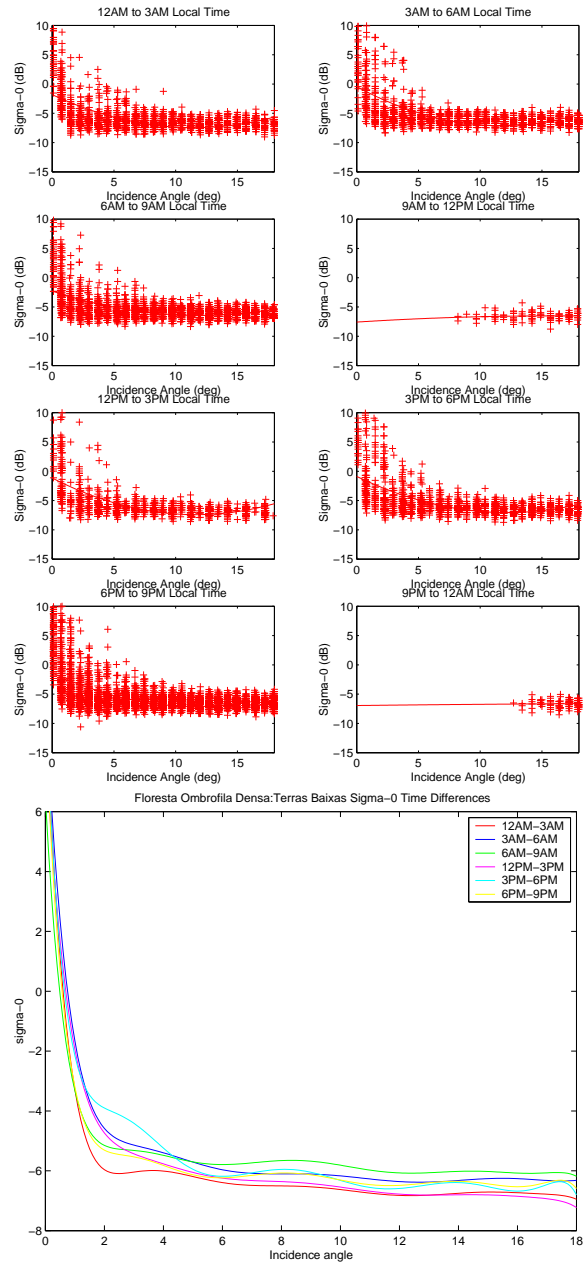
Figure 6.3: Sigma-0 vs incidence angle for Floresta Ombrofila Densa - Terra Biaxis
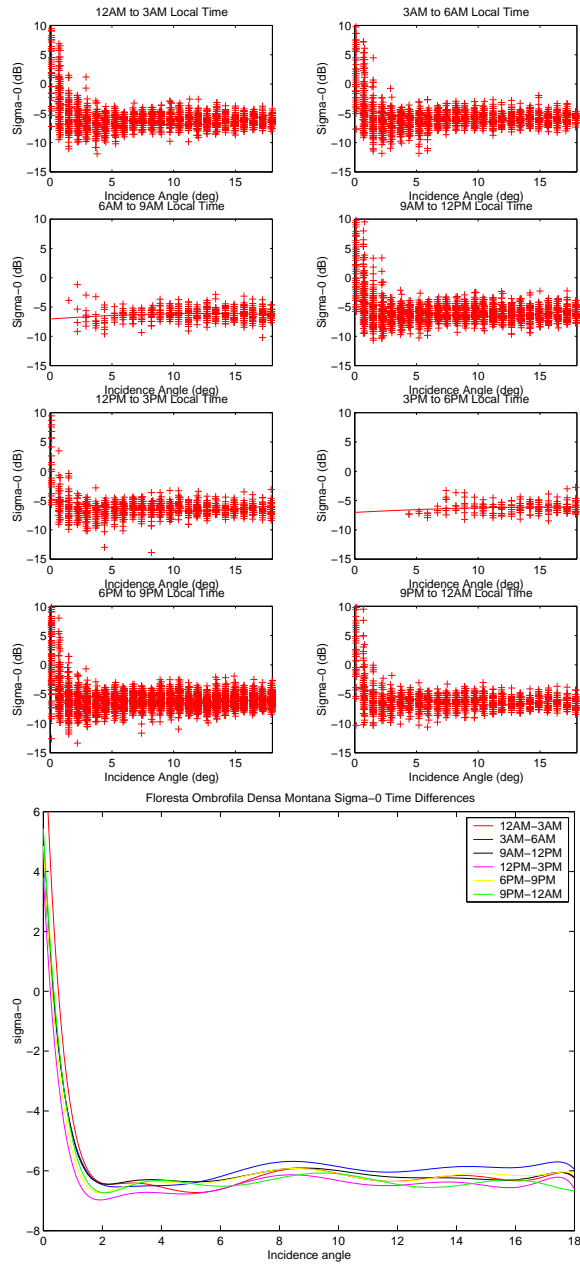
Figure 6.4: Sigma-0 vs incidence angle for Floresta Ombrofila Densa - Montana
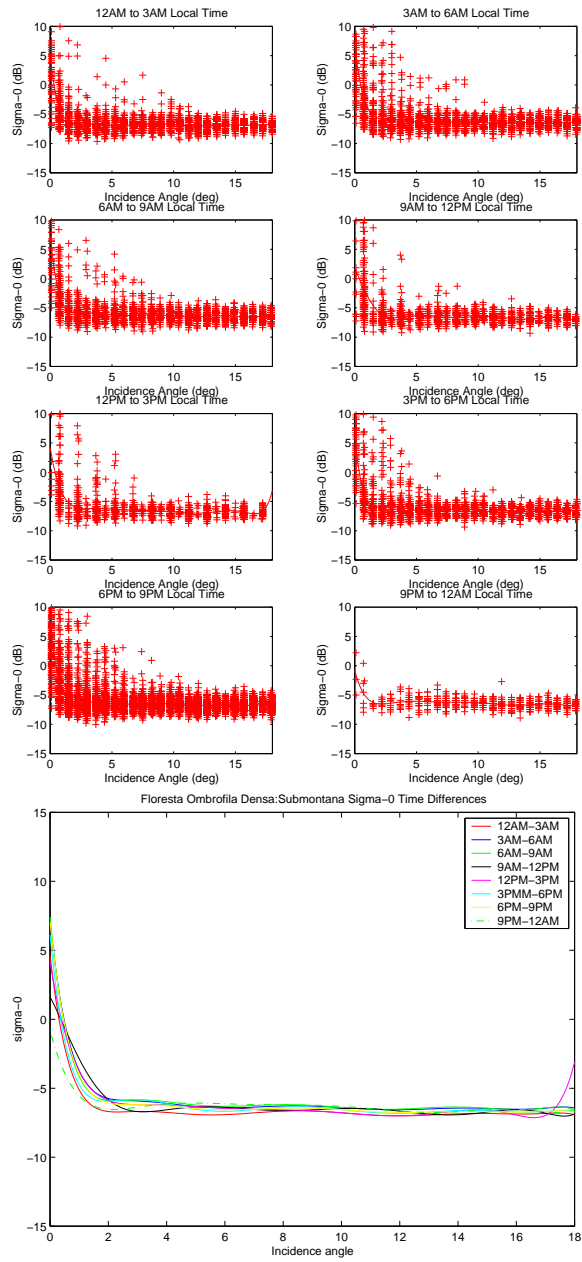
Figure 6.5: Sigma-0 vs incidence angle for Floresta Ombrofila Densa - Submontana
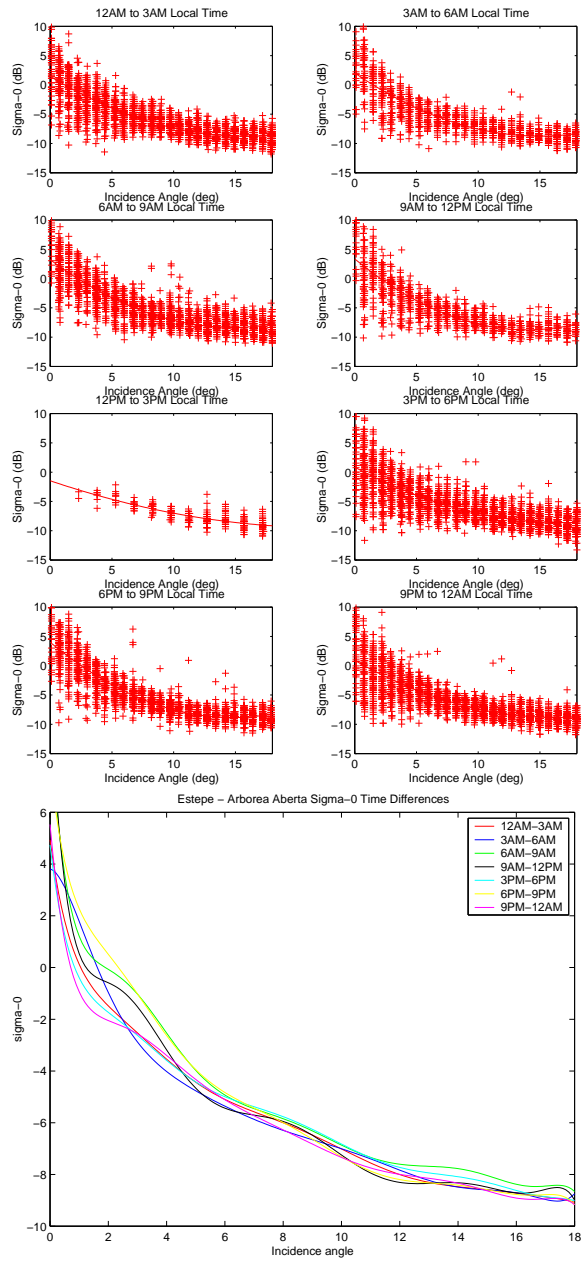
Figure 6.6: Sigma-0 vs incidence angle for Estepe -Arborea Aberta
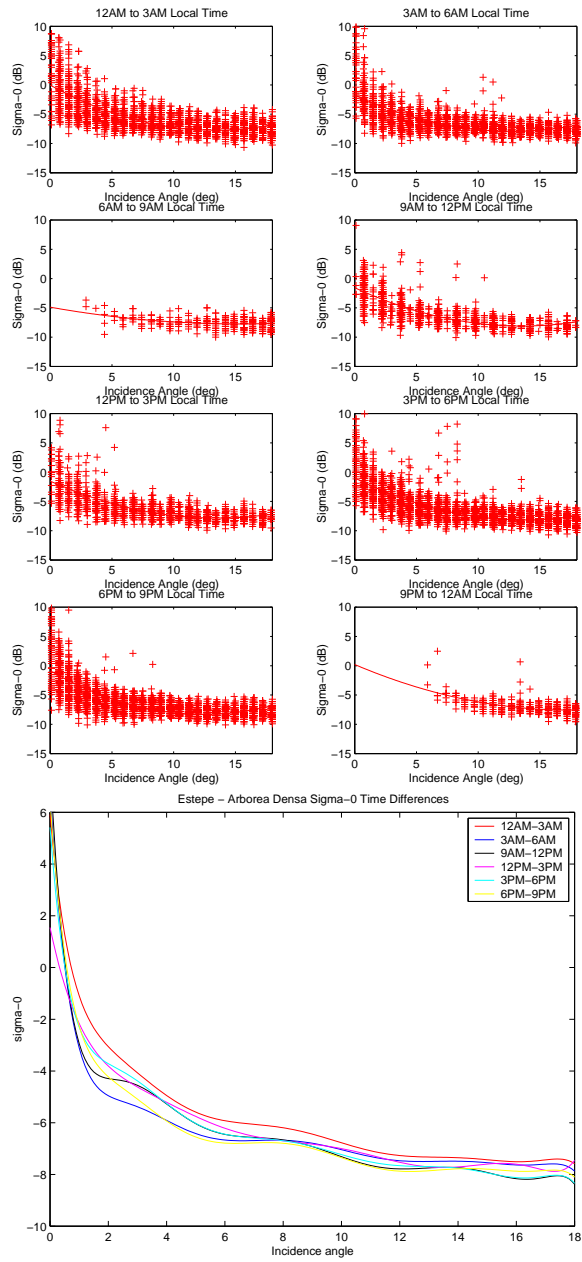
Figure 6.7: Sigma-0 vs incidence angle for Estepe - Arborea Densa
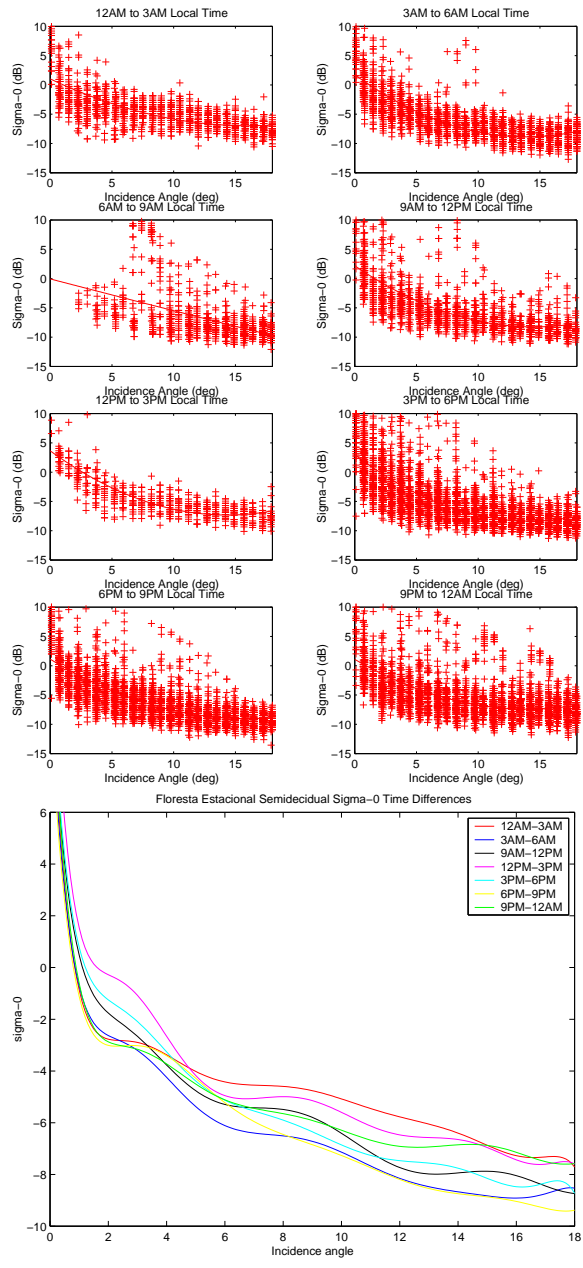
Figure 6.8: Sigma-0 vs incidence angle for Floresta Estacional Semidecidual
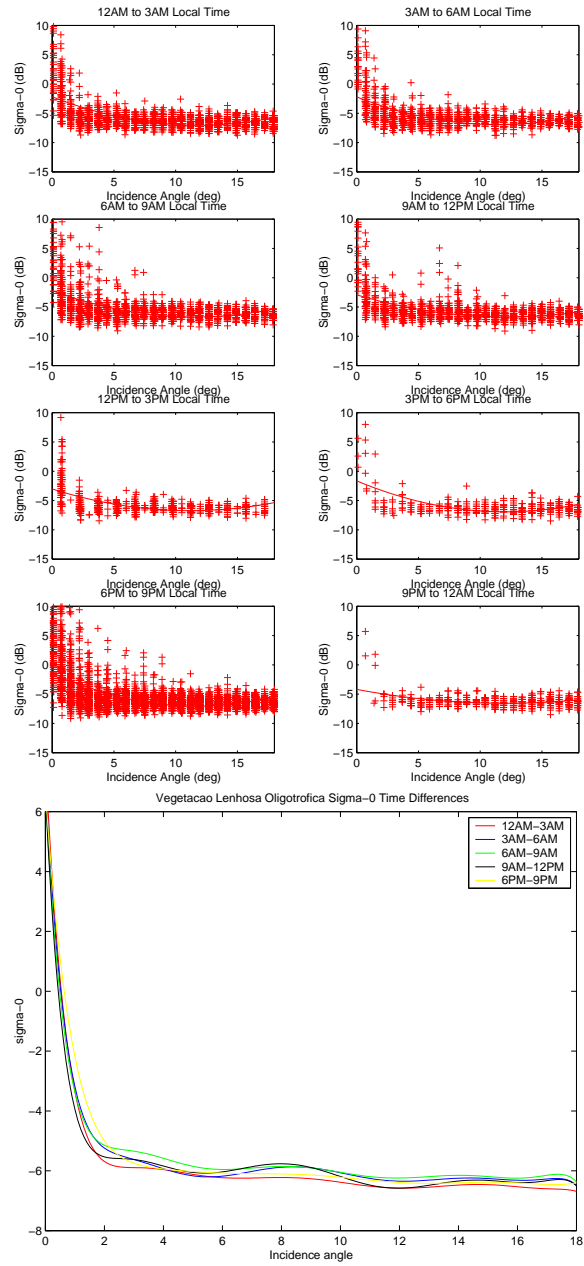
Figure 6.9: Sigma-0 vs incidence angle for Vegetacao Lenhosa
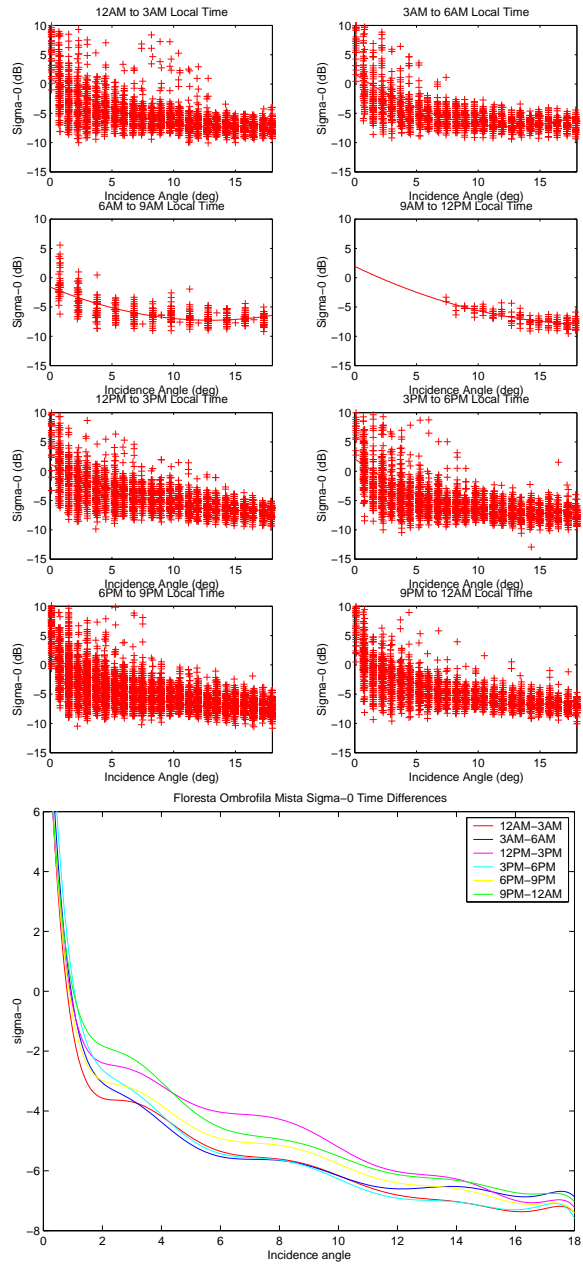
Figure 6.10: Sigma-0 vs incidence angle for Floresta Ombrofila Mista
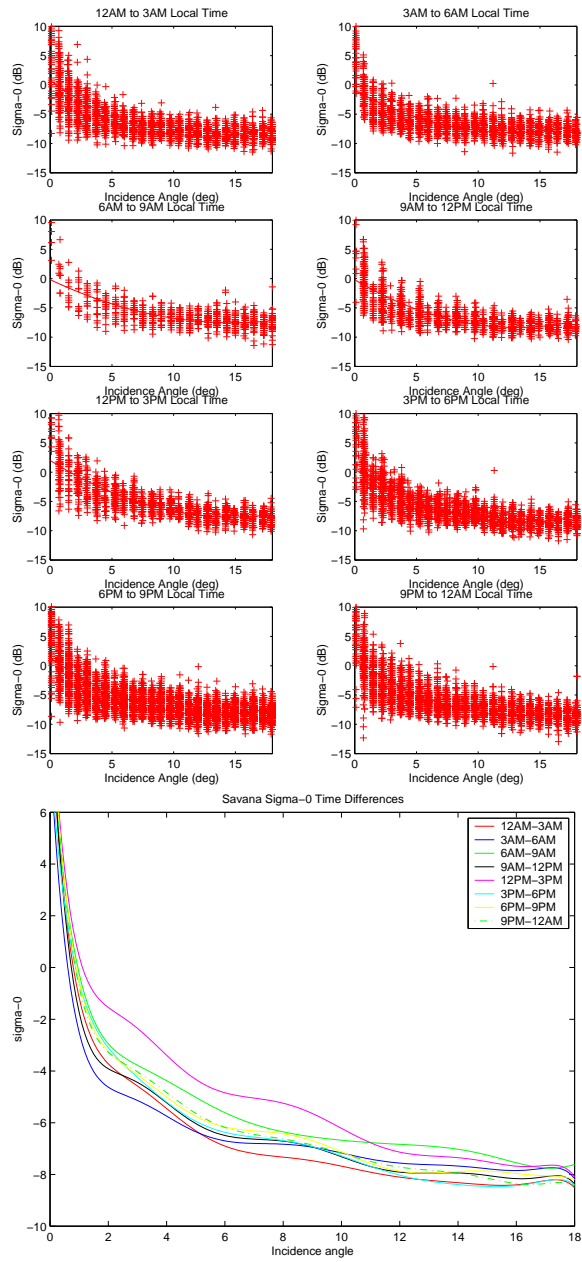
Figure 6.11: Sigma-0 vs incidence angle for Savana
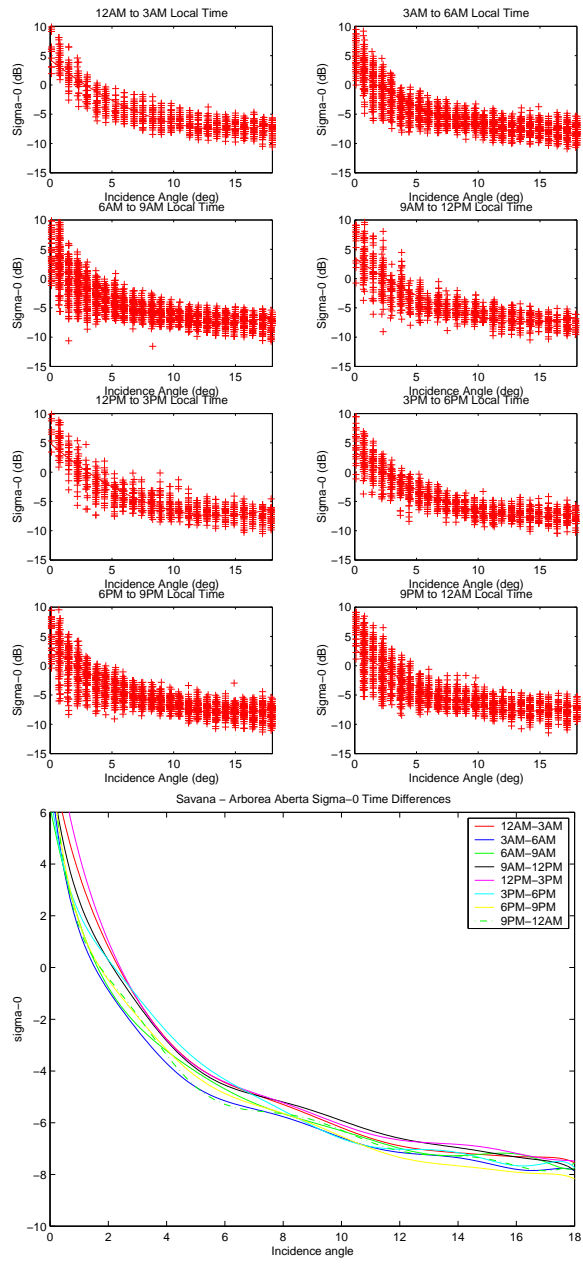
Figure 6.12: Sigma-0 vs incidence angle for Savana - Arborea Aberta

Figure 6.13: Sigma-0 vs incidence angle for Floresta Ombrofila Aberta: a second order least squares fit for data with incidence angle greater than 5 degrees
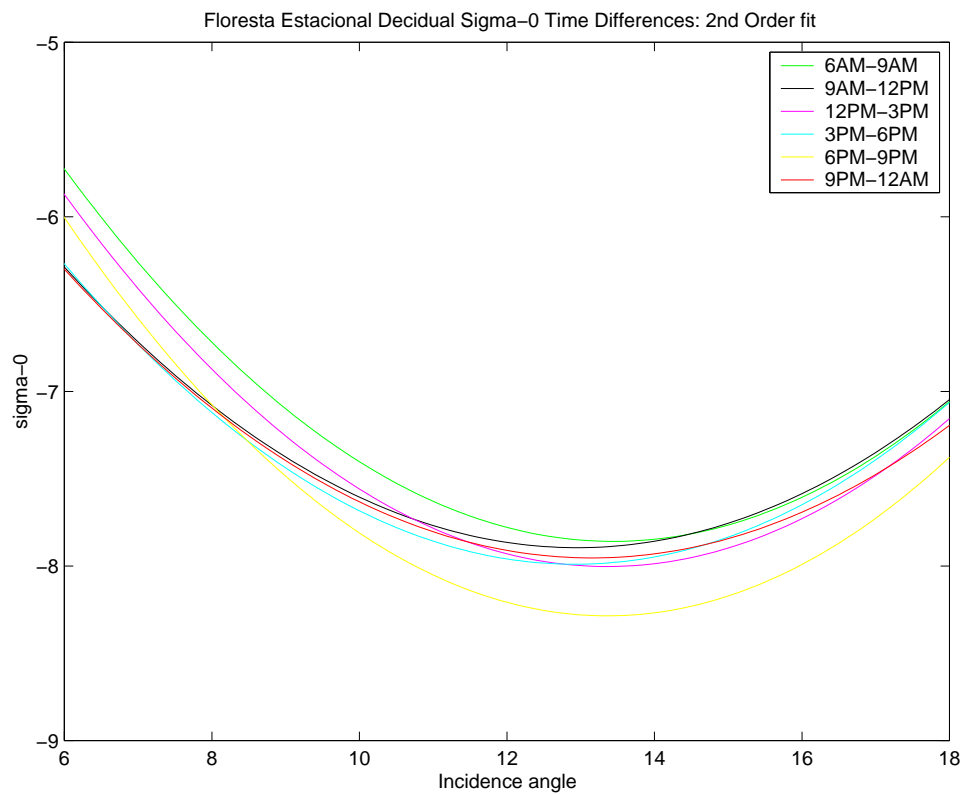
Figure 6.14: Sigma-0 vs incidence angle for Floresta Estacional Decidual: a second order least squares fit for data with incidence angle greater than 5 degrees
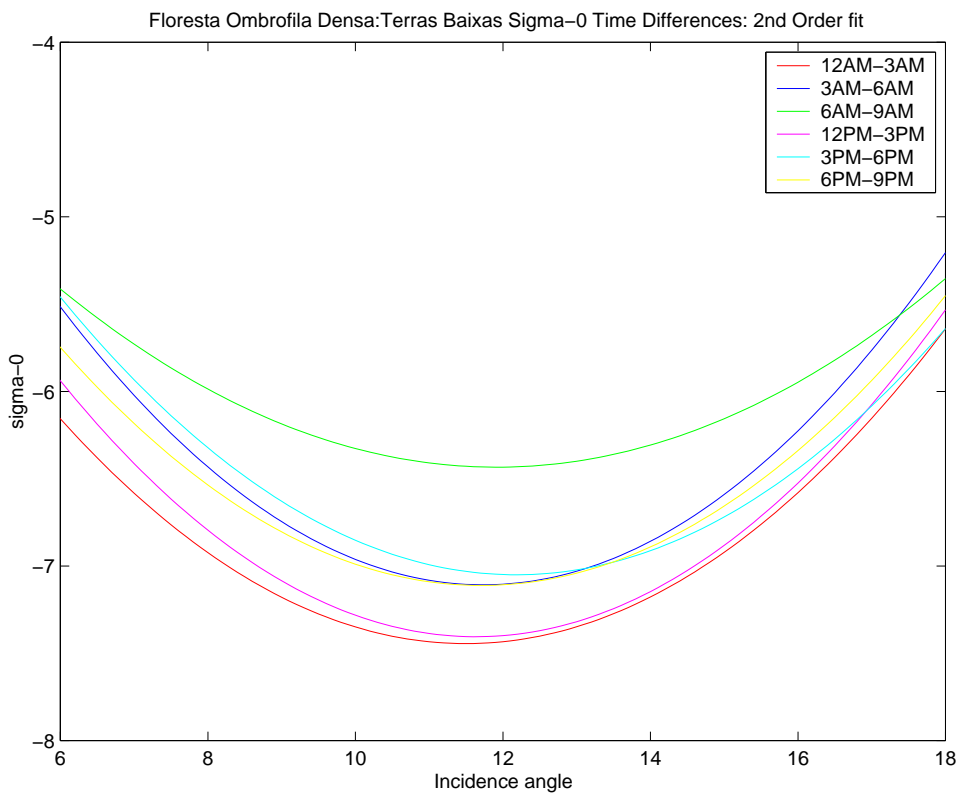
Figure 6.15: Sigma-0 vs incidence angle for Floresta Ombrofila Densa - Terra Biaxis: a second order least squares fit for data with incidence angle greater than 5 degrees
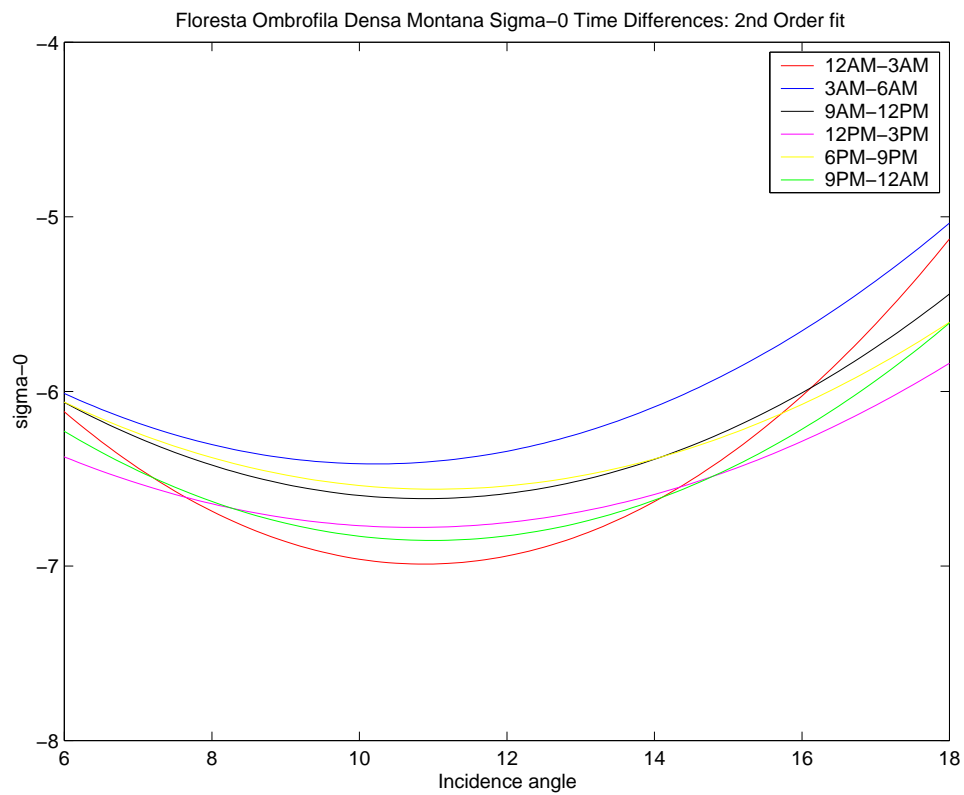
Figure 6.16: Sigma-0 vs incidence angle for Floresta Ombrofila Densa - Montana: a second order least squares fit for data with incidence angle greater than 5 degrees
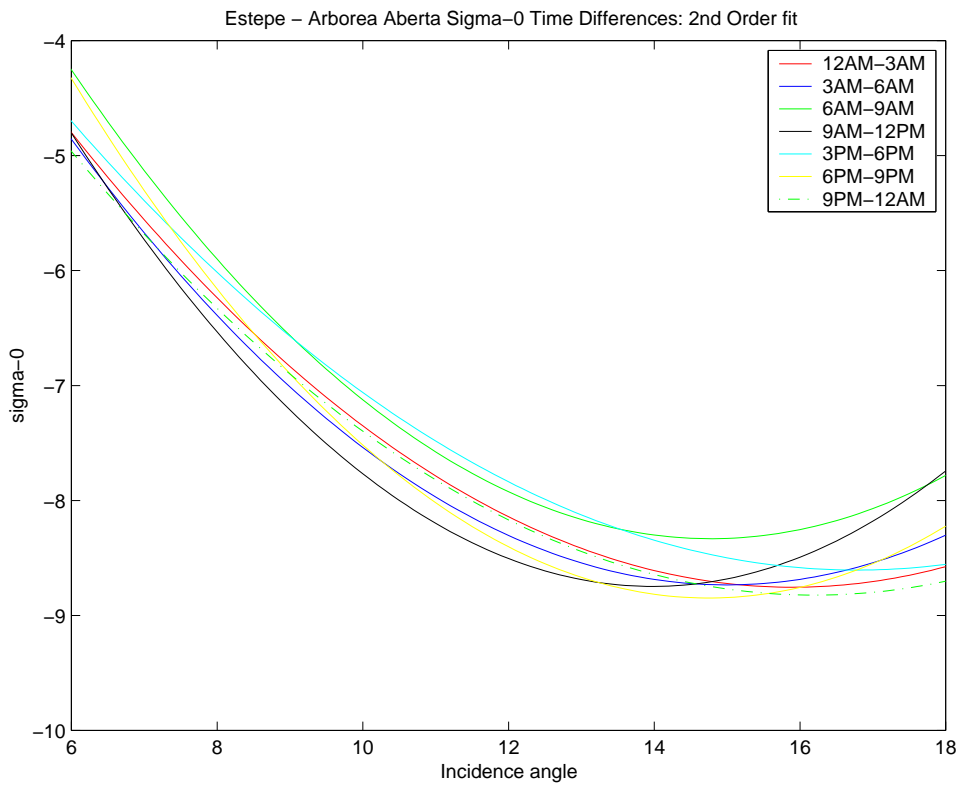
Figure 6.17: Sigma-0 vs incidence angle for Estepe -Arborea Aberta: a second order least squares fit for data with incidence angle greater than 5 degrees
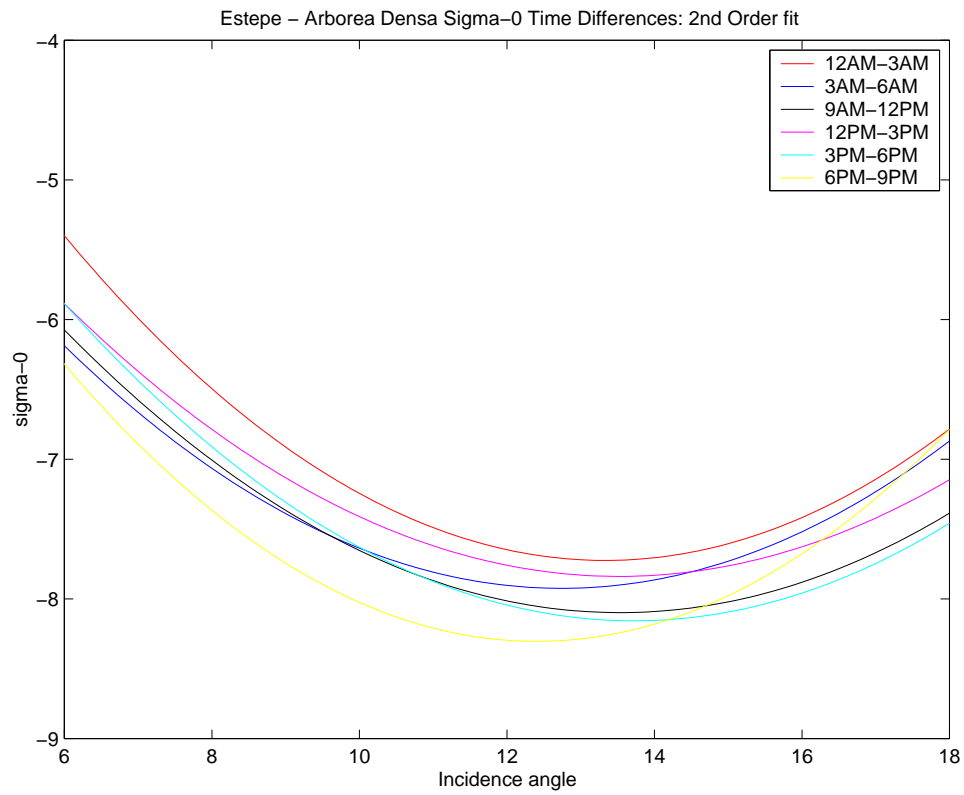
Figure 6.18: Sigma-0 vs incidence angle for Estepe - Arborea Densa: a second order least squares fit for data with incidence angle greater than 5 degrees
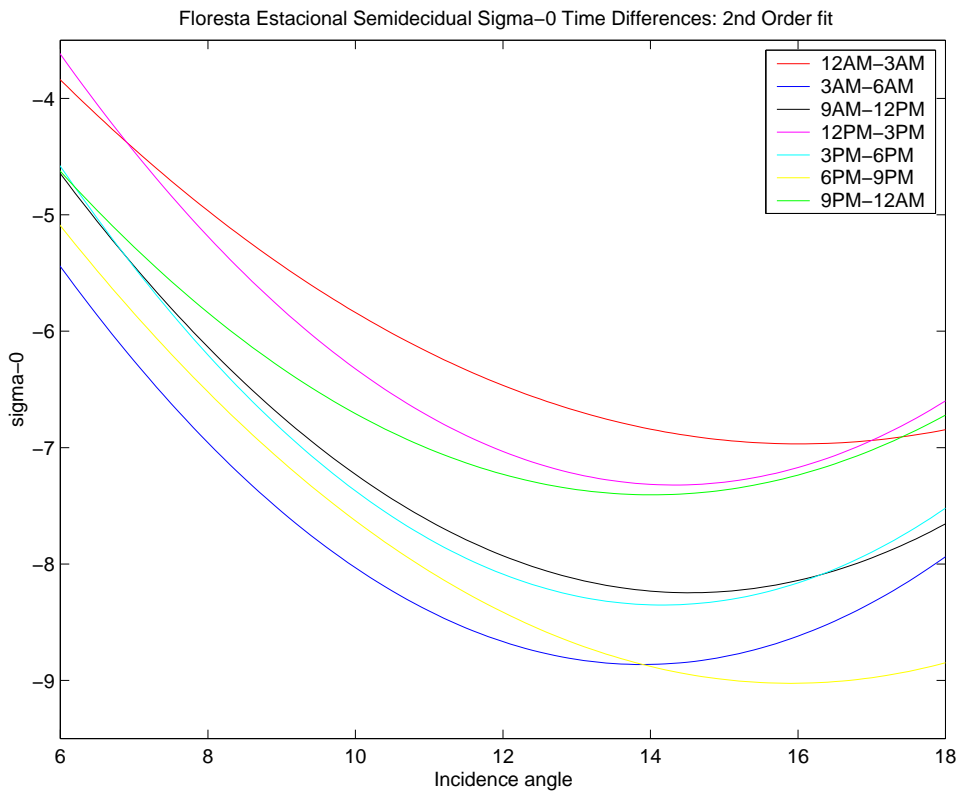
Figure 6.19: Sigma-0 vs incidence angle for Floresta Estacional Semidecidual: a second order least squares fit for data with incidence angle greater than 5 degrees
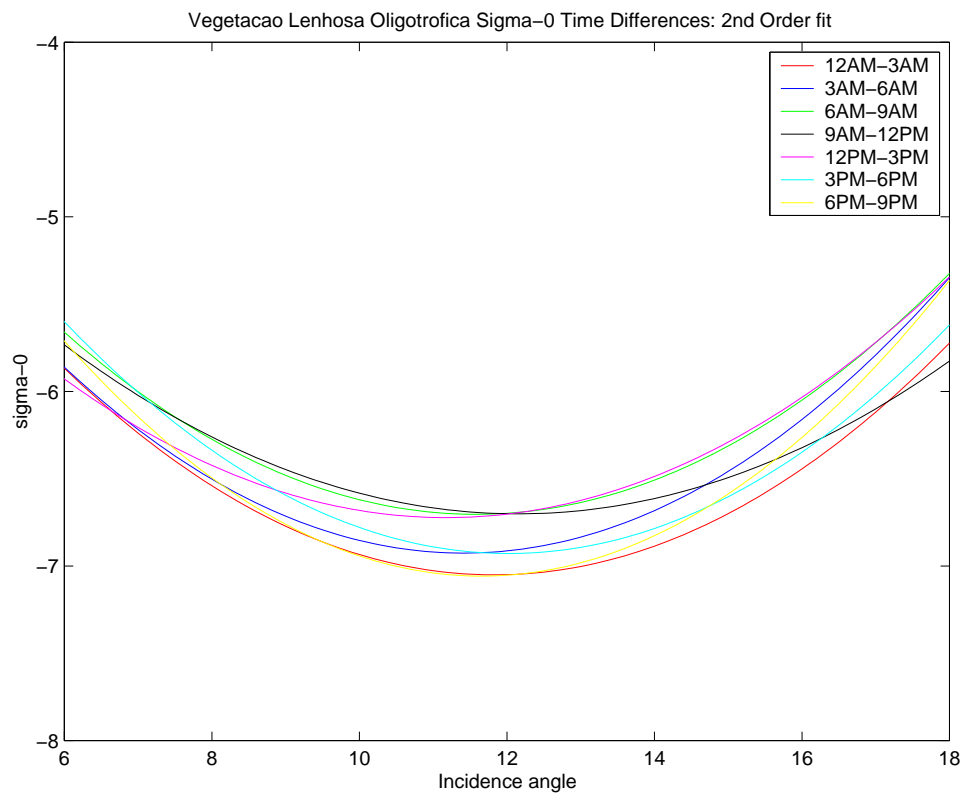
Figure 6.20: Sigma-0 vs incidence angle for Vegetacao Lenhosa: a second order least squares fit for data with incidence angle greater than 5 degrees
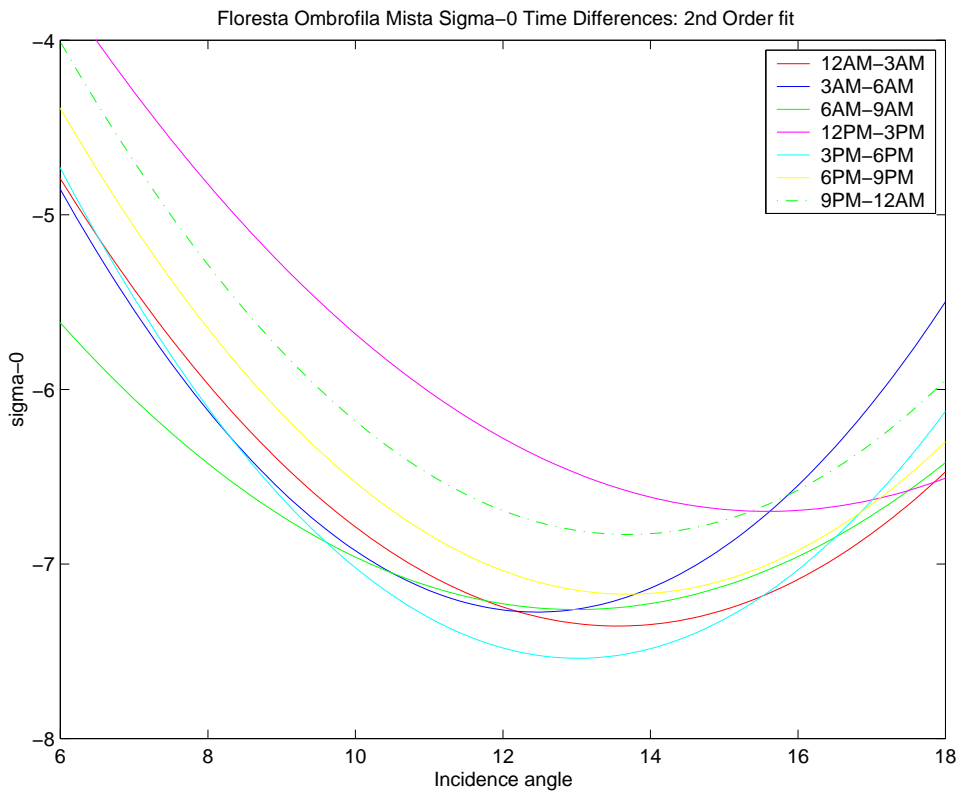
Figure 6.21: Sigma-0 vs incidence angle for Floresta Ombrofila Mista: a second order least squares fit for data with incidence angle greater than 5 degrees
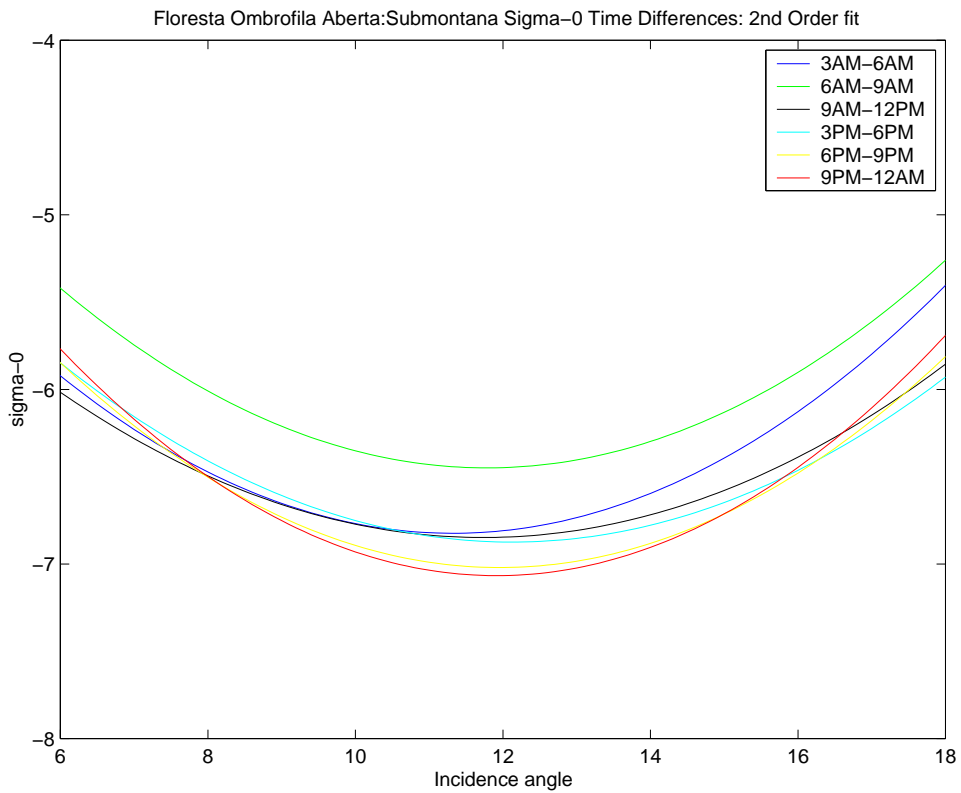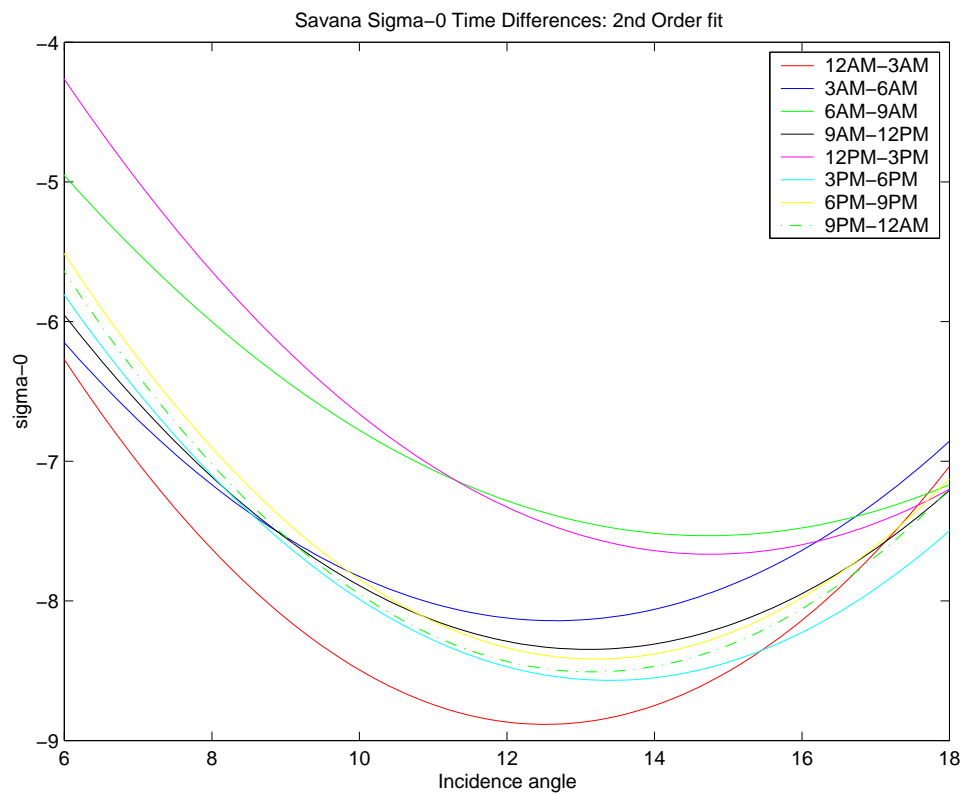
Figure 6.22: Sigma-0 vs incidence angle for Savana: a second order least squares fit for data with incidence angle greater than 5 degrees
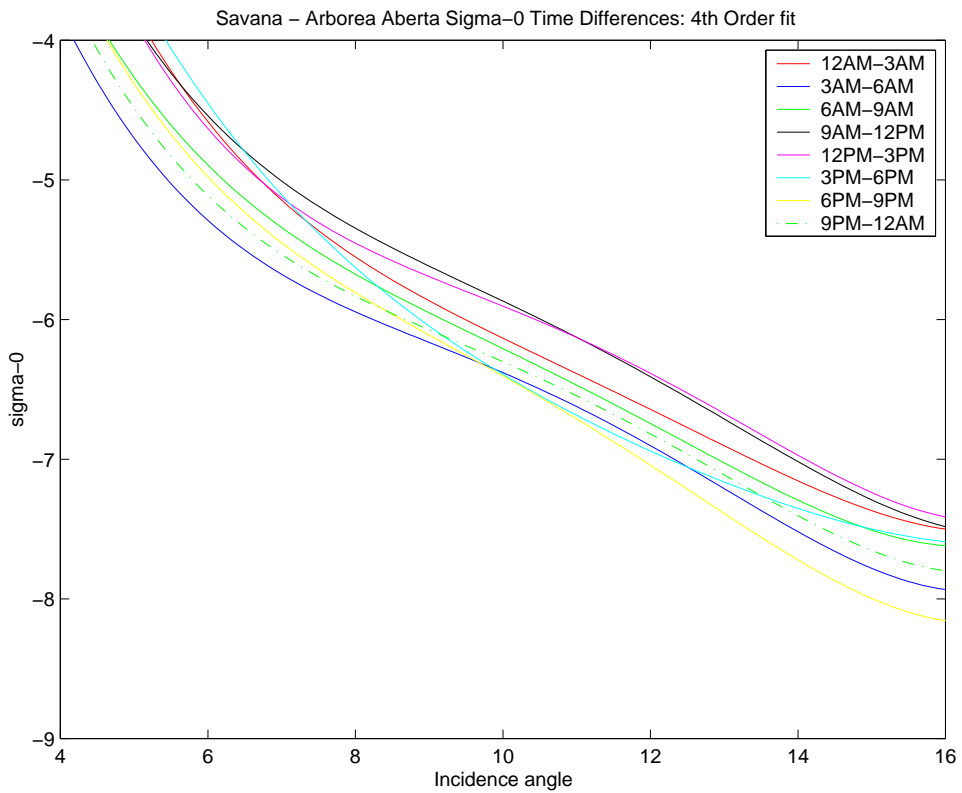
Figure 6.23: Sigma-0 vs incidence angle for Savana - Arborea Aberta: a second order least squares fit for data with incidence angle greater than 5 degrees

Chapter 7

## Monitoring of Urban Growth in the Tropics using TRMM SIRF

There is a growing concern for the depletion of the world's tropical rain forests. Forests in the Pacific islands, in Africa and in South-East Asia have been clear but or burnt at an alarming rate. The largest remaining tropical rain forest is presently located in the Amazon basin of Brazil and there is a large movement to protect that resource. Intimately tied to the mining, ranching and logging that would destroy this forest is the amount of urbanization that occurs in the country. As the cities in Brazil grow; resources are used, land is cleared for the use of man, and the demand on the land for financial venture increases. This chapter evaluates the use of data collected by the Tropical Rain Mapping Mission (TRMM) can be used to determine the extent of urban growth of Brazilian cities and the extent of damage to the forest in other areas. This study uses backscatter data collected by the Tropical Rain Mapping Mission Pricipitation Radar (TRMM PR). TRMM PR was originally design for the creation of 3 dimensional rain images but using the Scatterometer Image Reconstruction with Filtering (SIRF) algorithm, high resolution surface images are created that allow land studies. Chapter 2 of this thesis gives a detailed background on both the SIRF algorithm and the TRMM Precipitation Radar. Sample TRMM SIRF A and B images are shown in figures (**??**)and (**??**). Using TRMM PR data, TRMM SIRF is used to create images of several major Brazilian cities over two different time periods: April 1998 and April 1999. These two different time periods were chosen in order to determine if short-term urban growth could be monitored using TRMM PR
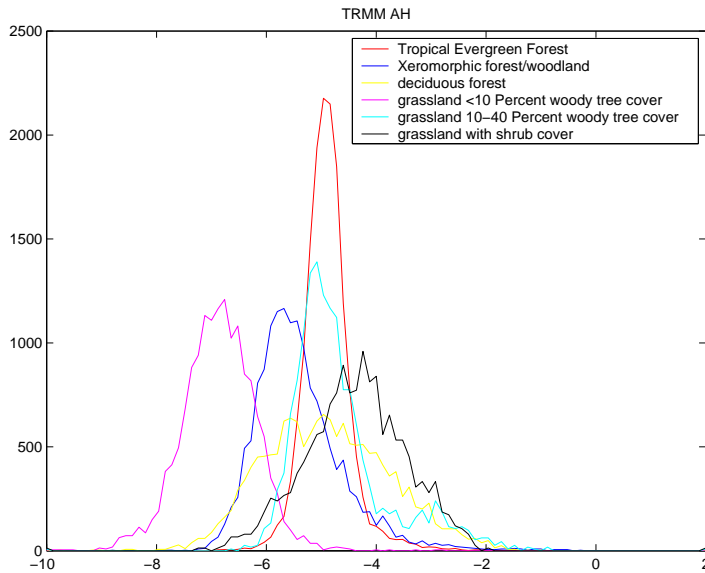
Figure 7.1: TRMM $\mathcal{A}$ values for different vegetation types

data. Changes were noticed in the images of several cities. This chapter discusses the changes noticed in Brasilia, Manaus, and Porto Vehlo over this time period. A control set of images were also created over a homogeneous region of tropical rain forest. These images were used to evaluate the effects of noise in the backscatter measurements on SIRF images.

7.1 Testing regions and Procedure

Six different cities in Brazil were chosen for this study. Each of these six cities have been listed in the top 10 cities in Brazil with the greatest population growth during the 1990's. These cities are tabulated in Table (7.1) with their latitude and longitude coordinates as well as the surrounding vegetation type. Vegetation type is important in this analysis as each vegetation has a different backscatter signature. Figure (7.1) shows the backscatter signatures for different vegetation types over the Amazon normalized to 11 °incidence angle $(\mathcal{A})$. Urban growth is detected by noticing a change in the backscatter measurements over time.

112

City	Latitude	Longitude	Vegetation Type
Manaus	-3°	-60°	Tropical Evergreen Forest
Sao Paulo	-23.5°	-46.5°	Deciduous Forest
Belo Horizonte	-19.7°	-44.0°	Grassland
Fortaleza	-3.6°	-38.5°	Xeromorphic Forest
Brasilia	-16.0°	-48.0°	Grassland
Porto Vehlo	-9.0°	-64.0°	Tropical Evergreen Forest
Homogeneous Rain Forest area	-15.0	-48.0	———

Table 7.1: City coordinates and surrounding vegetation types

7.1.1 Procedure

Data was collected for each of the regions listed above over two different time periods. The first time period, April of 1998, serves as a control set for this study, as the data collected during the second time period (April 1999) is compared against it. This particular time period was chosen as to avoid the affect of seasonal variation and also to allow ample time for change to occur. Data from the two time periods was used to create two different sets of SIRF images for each region. Using SIRF allows us to take advantage of the resolution enhancement to compare the $\mathcal{A}$ values of the surrounding landcover with the data shown in Figure (7.1). In order to verify that the observed change in the $\mathcal{A}$ values around some cities aren't a result of the noisy TRMM PR σ^o measurement, the changes in each city are compared to the observed change between 1998 and 1999 in a homogeneous region of rain forest. It is assumed that the temporal variability of this region is extremely small and that any change that is observed in this area is a result of noise. This regions coordinates are also listed in Table (??). Although differences in $\mathcal{B}$ were examined for each region, the results of this comparison are not discussed in this chapter.

7.2 Results

The results from this study are shown in Figures (7.2) through (7.8). Figure (7.8) shows the rainforest images discussed above. These two images are used in this

study as a control and are discussed in greater detail below. Many of the cities don't appear to have significant change. However, Manaus, Porto Vehlo and Brasilia do show some interesting changes and their results are discussed below.

7.2.1 Manaus

Located on the Black River and less than five miles from the Amazon River, Manaus sits in the heart of the Tropical Rain Forest. It is the capital of the state of Amazonas, Brazil and is one of the fastest growing areas of Brazil. As of 1996, Manaus had a population of 1.17 million people and it is estimated to have a current population of 1.43 million people (1998). Manaus is ideal for this type of study because backscatter from urban growth should have a much higher measurement value than backscatter from the surrounding rainforest. The results from the comparison can be seen in Figure (7.2). At first glance, it appears that there has been considerable growth along the northeast and southwest sides of the city. By 1999 the city appears to have taken on a much more rounded look which seems consistant with a natural pattern of urban growth. The difference image, also shown in Figure (7.2), shows that there are areas of higher σ^o values and also areas of lower measurements between 1998 and 1999. The greatest difference in σ^o measurement between the two years is +1/-2 dB.

7.2.2 Porto Vehlo

Porto Vehlo was chosen for this study for many of the same reasons that Manaus was chosen. Besides being one of the fastest growing cities in Brazil and the capital of the state of Rodonia, Porto Vehlo straddles the Madeira River and lies in the heart of the Amazon rain forest. Any urban growth requies the replacing of rain forest with city streets and buildings which act very much like corner reflectors to radar pulses. These σ^o measurements of the forest and urban areas are very different. Figure (7.7) shows the different response between 1998 and 1999 for this area. This comparison suggests growth to the north of the city and towards the northeastern corner of the image. The difference image doesn't show much else except that there

114

seems to be a darker response in 1999 just to the west of the city. The greatest difference in σ^o measurement between the two years for this region is +2/-4 dB.

7.2.3 Brasilia

In 1956, the Brasilian government moved the capital of Brasil from Rio de Janiero to a planned city that was named Brasilia. Brasilia is singular among the cities of Brazil because it is the only city in Brasil that was planned out by the government. It has since become one of the faster growing cities in the country. It was chosen for this study based on it's potential for visible growth. Looking at figure(7.6), the only growth seems to be within the existing city boundaries. According to the 1998 and 1999 SIRF images of Brasilia and the difference image shown in Figure(7.6), the city extent hasn't changed much but the backscatter measurements within the boundaries of the city seem to be higher in 1999. Just as in the other two cities discussed, the greatest positive measurement difference in the region is around +2dB.

7.2.4 Discussion of results

The differences noted between 1998 and 1999 in the cities mentioned above can easily be explained with a rudimentary understanding of radar backscatter. Urban areas have features such as paved roads, buildings and sidewalks; which often exhibit corners. These right angles act almost as corner reflectors and the backscatter measurement over these areas will be quite high. Most of the natural land cover in the surrounding areas will exhibit volume scattering to some degree or another. While volume scattering will yield a higher backscatter measurement at an arbitrary incidence angle than surface scattering (water, dry ground), it will still be considerably lower than a measurement from an urban area. The differences between 1998 and 1999 can be explained by the urbanization and clearing of the land. Lower measurements are a result of removing the vegetation that causes volume scattering; more surface scattering results and the backscatter measurement is lower.

These results, however, are meaningless without a comparison that examines the difference in measurements that are due primarily to noise. Figure (7.8) shows the

difference between 1998 and 1999 for a homogeneous rain forest region. Noise should be the primary reason for measurement differences in this region as neither image was created with rain tainted data and as the region is located in the heart of the rain forest. As can be seen from the difference image in Figure (7.8), the comparison shows differences in excess of +/- 1.5 dB in a region that should show almost no difference.

7.3   Conclusions

Although TRMM SIRF images have the resolution necessary to observe some changes in σ^o of large cities; this study has shown that because of the noisy TRMM σ^o measurements, results from this type of study are unreliable. Many of the larger cities in Brasil appeared to exhibit growth in a comparison of SIRF images made in 1998 and in 1999. The greatest positive difference in the $\mathcal{A}$ images for these cities was +2 dB. It was shown, however, that that the noise in the TRMM σ^o measurements yielded differences in $\mathcal{A}$ that were in excess of +1.5 dB. TRMM SIRF cannot be reliably used to monitor urban growth.

116

Figure 7.2: Manaus SIRF images: 1998, 1999 and difference images.

Figure 7.3: Sao Paulo SIRF images: 1998, 1999 and difference images.

Figure 7.4: Belo Horizonte SIRF images: 1998, 1999 and difference images.

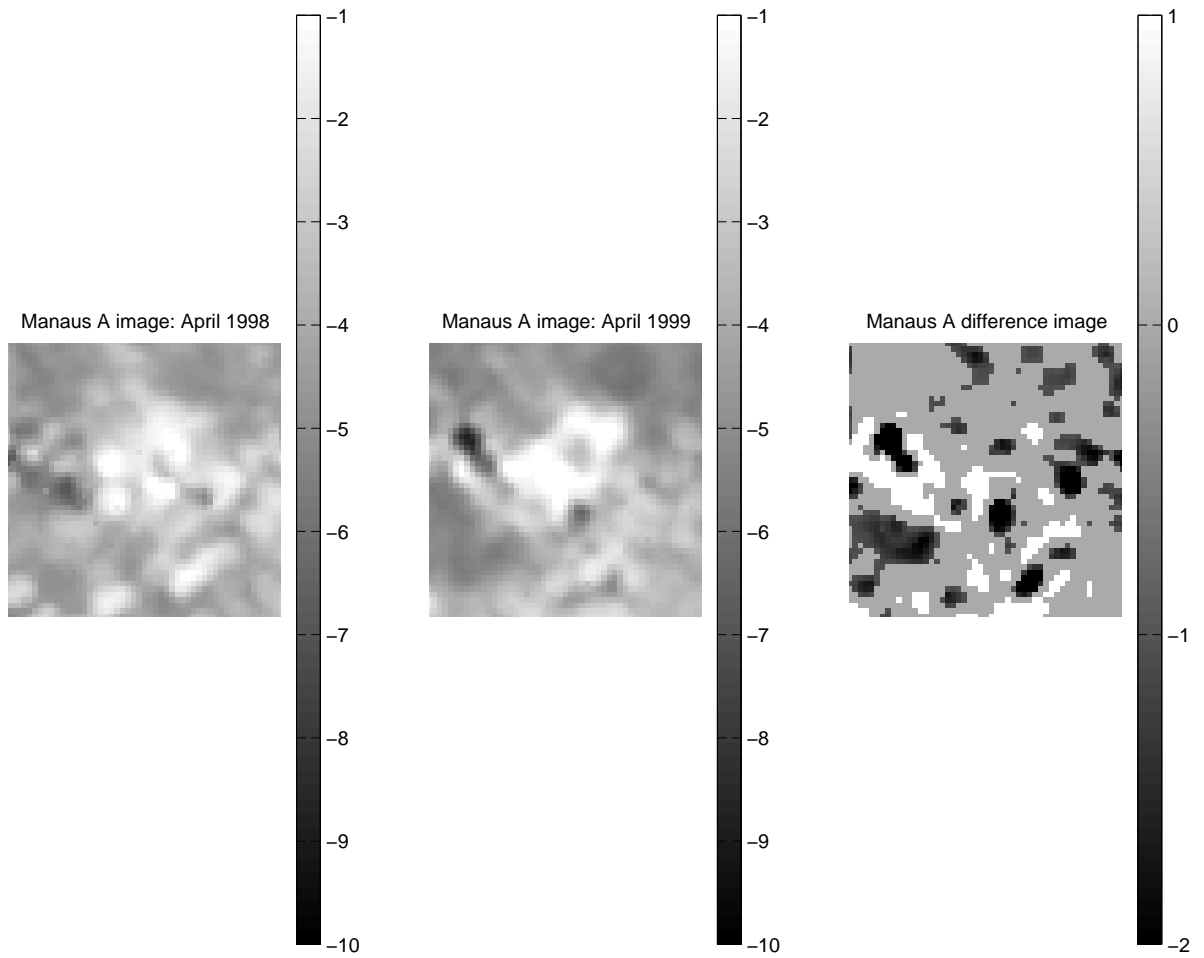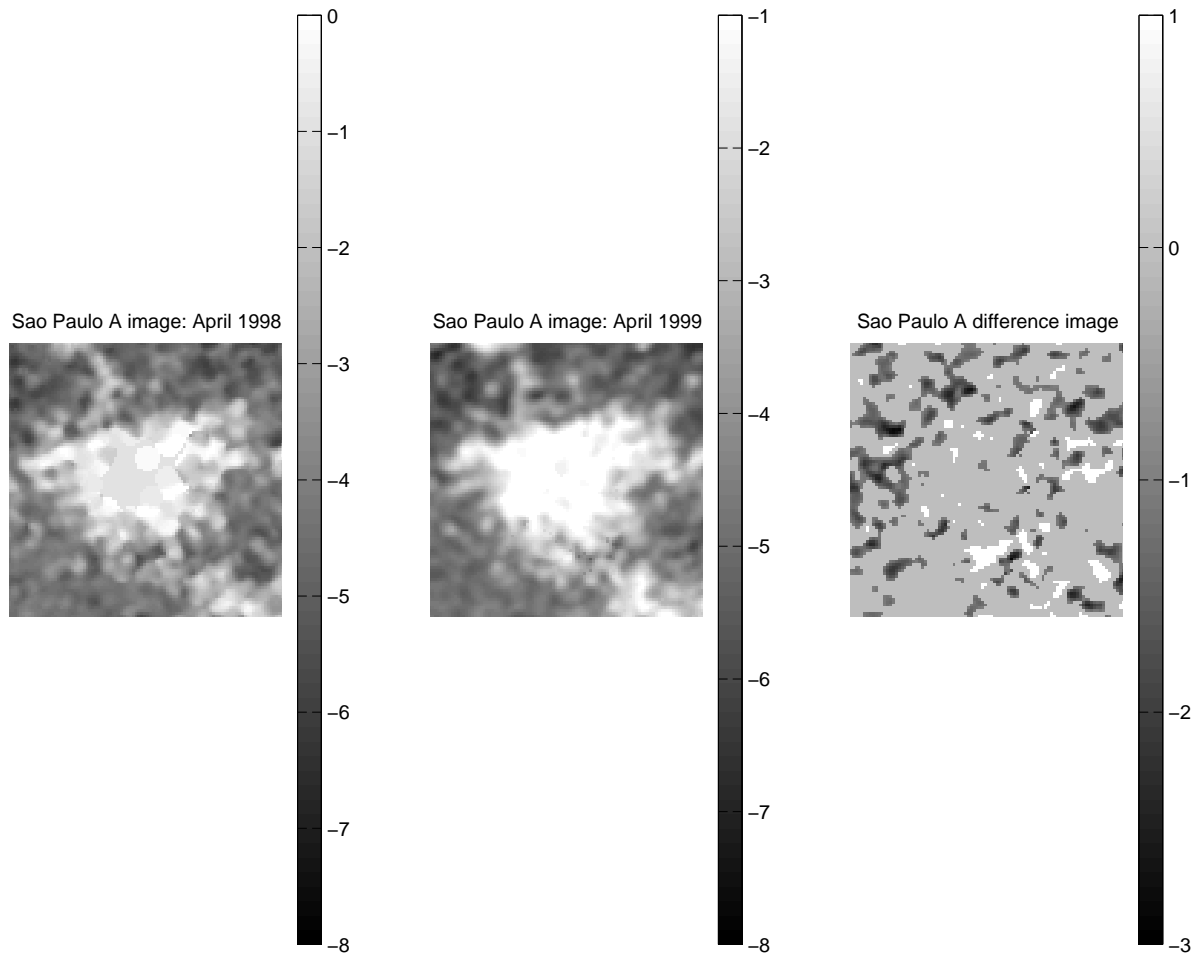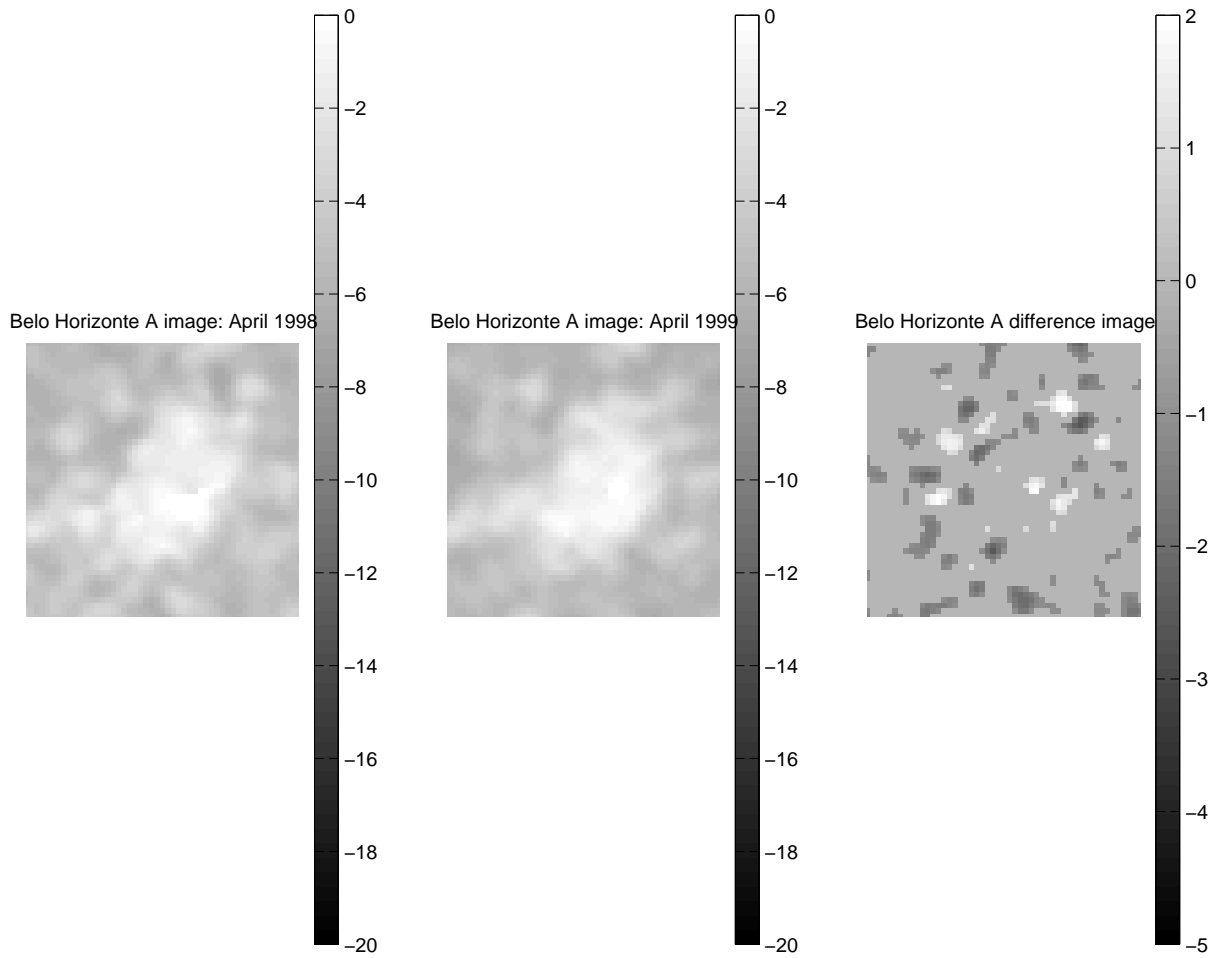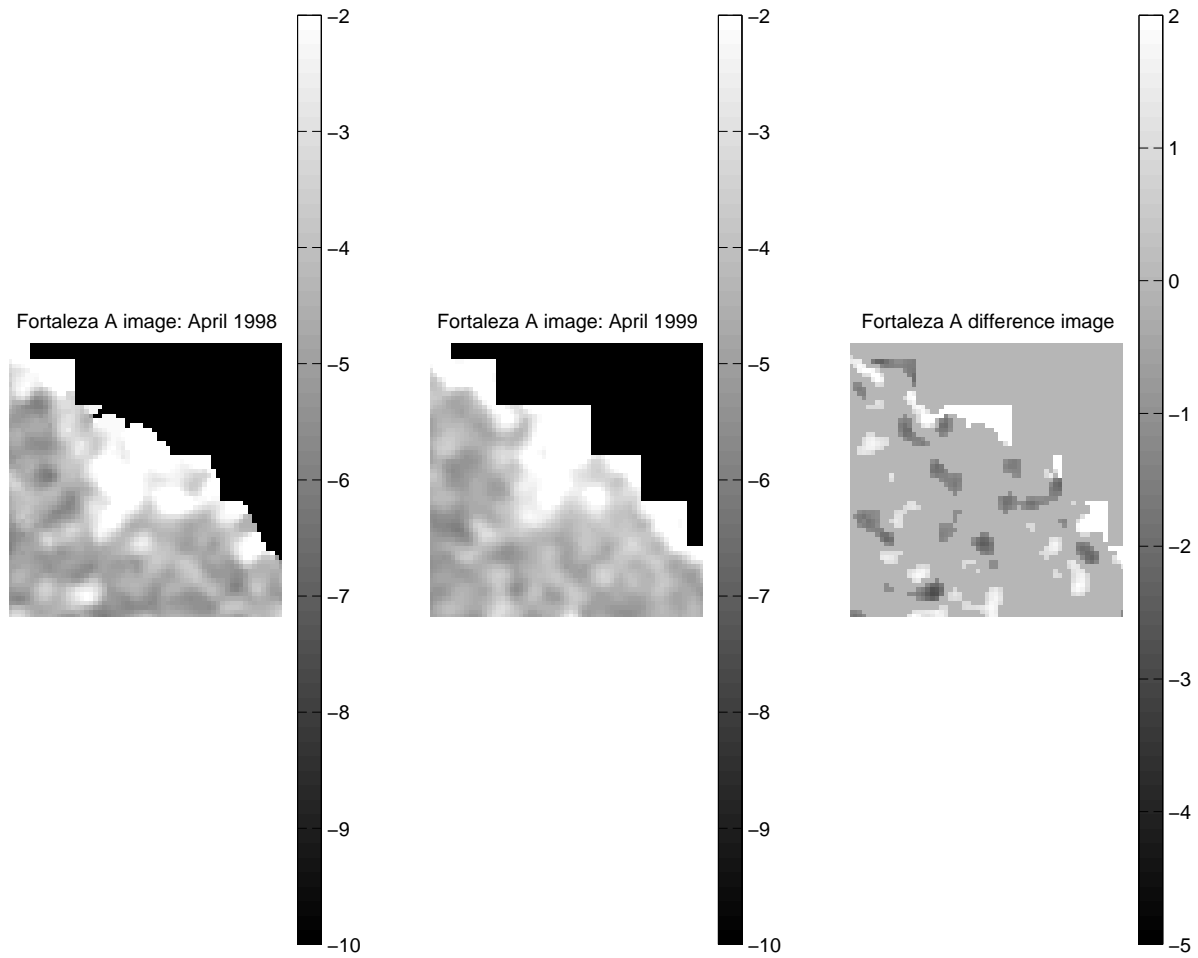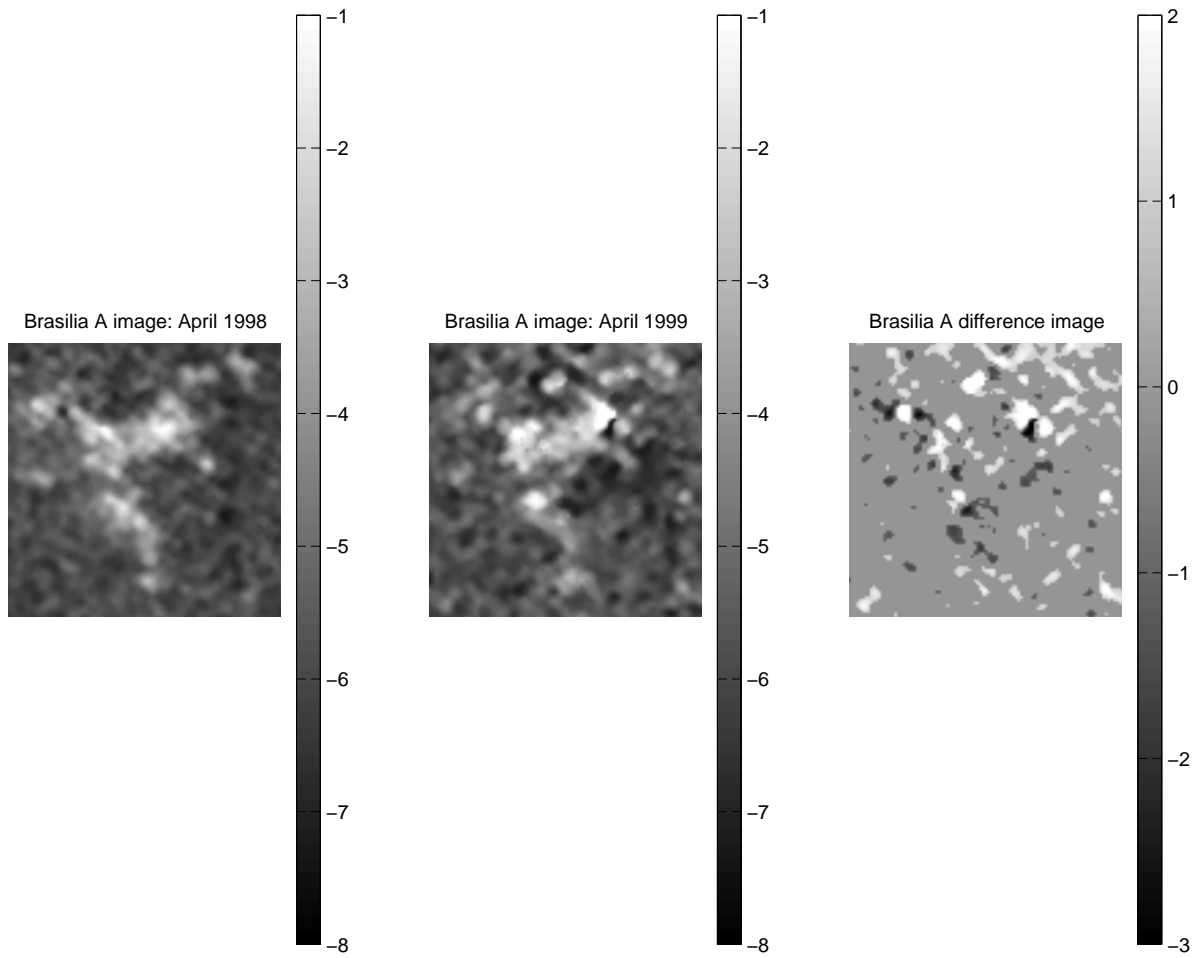Figure 7.5: Fortaleza SIRF images: 1998, 1999 and difference images.

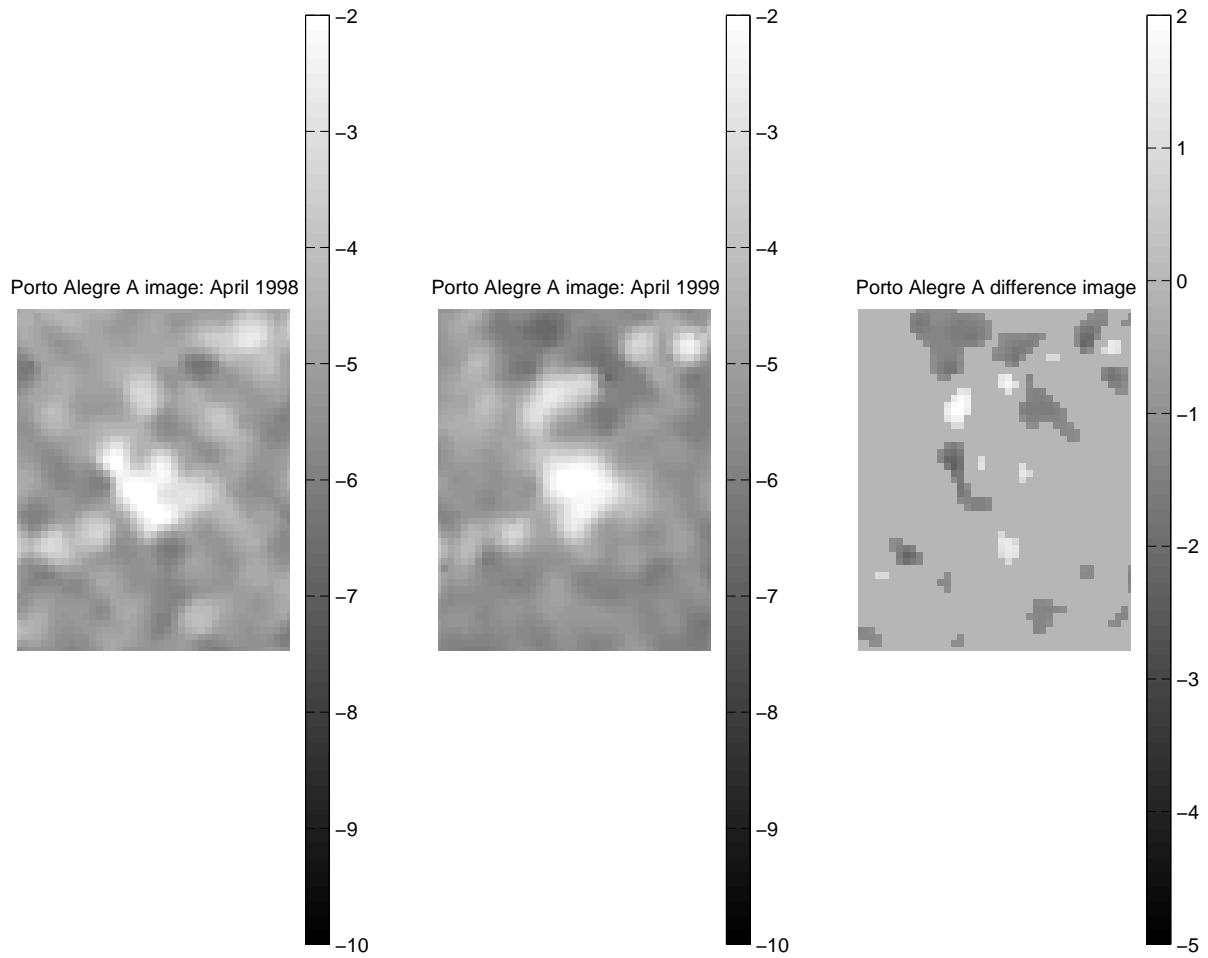Figure 7.6: Brasilia SIRF images: 1998, 1999 and difference images

Figure 7.7: Porto Vehlo SIRF images: 1998, 1999 and difference images.
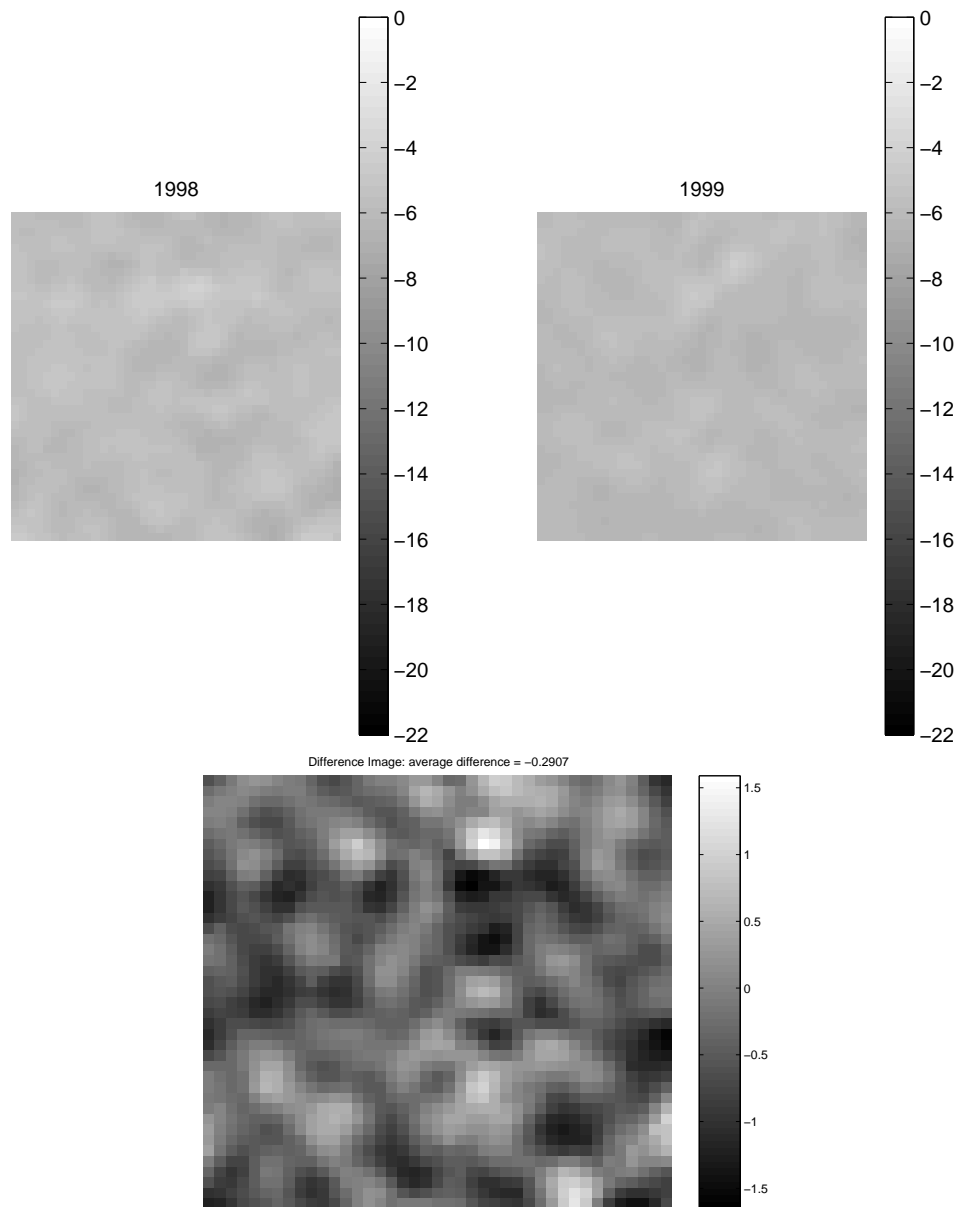
Figure 7.8: Homogeneous tropical rain forest SIRF images: 1998, 1999 and difference images. Standard Devation for the difference image was determined to be .102

Chapter 8

Conclusion

This final chapter gives a summary of the results obtained and discusses the contributions this thesis has made to the fields of scatterometery and of earth remote sensing. This chapter ends with a discussion of future work that can be done in this area.

8.1   Summary

This thesis has presented an almost complete analysis of low incidence Ku-band radar interaction with tropical vegetation types. This type of analysis has never been done before as low incidence angle σ^o has only been made available on a global scale since the launch of the Tropical Rain Mapping Mission (TRMM). The TRMM Precipitation Radar (TRMM PR) has been the central source of data for this thesis and has been the focus of all connected studies.

An optimization study was first performed using TRMM data. The Scatterometer Image Reconstruction with Filtering (SIRF) algorithm was developed to use backscatter measurements taken over land regions and create higher resolution radar images. This algorithm had been successful with several scatterometers prior to TRMM; data collected by NSCAT, ERS1 and ERS2 has been used to create regional images from all over the world. TRMM PR, however, was designed with a different intention and so SIRF needed to be optimized for use with TRMM PR data. This optimization study was successful and TRMM PR images can be created with an image resolution of 1.1 km.

Secondly, TRMM PR σ^o was completely analyzed as it relates to tropical vegetation types. The scope of the vegetation types was limited due to the equatorial orbit of TRMM (35°to -35°latitude). TRMM PR backscatter measurements were compared to NSCAT measurements by taking the normalized SIRF parameters $\mathcal{A}$ and $\mathcal{B}$ for each instrument and comparing them over several different vegetation types. It was found that the results using higher incidence angle σ^o measurements (NSCAT data) had a greater spread between vegetation types; low incidence angle data had an interesting spread between some vegetation types, but not to the extent that NSCAT data did.

TRMM PR σ^o) measurements were also examined as to their relationship with incidence angle (θ) over different vegetation types. An interesting relationship was discovered between canopy density and the σ^o/θ curve. This relationship was determined simply to be different combinations of volume scattering and surface scattering components for different vegetation types. A latitude study was also completed, showing the different responses for similar vegetation types at different latitudes. The differences observed in this study were assumed to be functions of the amount of moisture in a particular area.

Lastly, a study was completed that attempted to show that TRMM PR backscatter measurements could be used to show short term urban development in a region. SIRF images were created over several of the largest cities in Brazil for both 1998 and 1999. While changes were observed in each of the cities over this time period, it is unsure how much of the observed change in merely a function of noisy backscatter measurements and how much accurately depicts urban growth.

8.2 Contributions

The purpose of this thesis was to make a complete study of the interaction between tropical vegetation types and low incidence Ku-band radar. This study was made using TRMM PR raw data and land images created using an resolution enhancing imaging algorithm known as the Scatterometer Image Reconstruction (SIR) algorithm. Outlined below are the contribution made by this thesis.

126

The first contribution is an optimization of the SIRF algorithm for use with TRMM PR data. TRMM PR has the highest nominal resolution of any data set that has been used with the SIRF algorithm, which allows SIRF to reconstruct extremely accurate land images using TRMM data. TRMM PR however, is not a scatterometer, has a different illumination pattern and much noisier σ^o measurements than prior data sets. For this purpose, SIRF is optimized in order to assure the greatest accuracy possible in the images and consequently the highest possible accuracy in the studies using the images.

The next contribution uses the SIRF algorithm to compare several different parameters over different vegetation types between TRMM PR data and NSCAT data. TRMM PR and NSCAT are complementary instruments as they operate using the same frequency (Ku-band) but totally different incidence angles: NSCAT using the upper incidence angles (20°- 70°) and TRMM PR using the lower angles (0°- 17°). This comparison showed that TRMM PR SIRF parameters have less instantaneous information about vegetatation than NSCAT SIRF parameters. However, this study provides a basis where a seasonal study of TRMM SIRF parameters could be made for each tropical vegetation type. Using this information, vegetation classification using high resolution TRMM PR SIRF images may be possible.

This thesis also provides an accurate characterization of the low incidence angle relationship between incidence angle and σ^o for different vegetation types. It explores the relationship between surface scattering and volume scattering as a function of canopy density. The results enclosed also provide data on the σ^o/incidence angle relationship for similar vegetation types at different latitudes. These contributions open the possibility to a moisture study using scatterometer backscatter measurements.

Lastly, a time study is completed to show the σ^o dependence on the local time of day at low incidence angle. This study is valuable for scatterometer calibration and interesting for the effects of moisture(dew) on the σ^o measurements. This study also offers insight in vegetation scattering theory.

8.3 Future Work

As this thesis progressed, a number of areas of future research and study were identified; either as an unfinished part of the current research or as an additional study that is made possible by the results of this thesis.

This thesis has presented an almost complete analysis of low incidence Ku-band radar interaction with tropical vegetation types. A study that would make this analysis complete would be a seasonal study of TRMM PR σ^o for each vegetation type. Information of this kind could be the foundation of a vegetation classification algorithm using high resolution TRMM SIRF images. This study was not completed as part of this thesis due to time considerations.

Seawinds on Quickscat was launched in June of 1999 as the most advanced scatterometer to date. Although designed for near surface oceanic wind retrieval, Quickscat also collects backscatter measurements over land that will allow SIRF to create yet another set of radar images. Because TRMM PR SIRF images have much higher resolution, they can serve as reference images for validation of Quikscat images. Although the images will have been created using measurements of different incidence angle ranges, the validation of the edges of land masses, rivers, and other stationary land features will be possible using TRMM PR SIRF images.

Lastly, the analysis completed in this thesis showed a difference in the σ^o/incidence angle realationships between similar vegetation types at different latitude coordinates. It has been postulated that this difference is due to a difference in moisture; both soil moisture and the moisture conatined in the vegetation canopy. it would be an interesting study to dtermine if Ku-band scatterometry data could be used for moisture studies over the amazon. This thesis provides information on the behavior of σ^o with different vegetation types and could be used as a foundation for that study.

Bibliography

[1] *Land Applications of ERS-1 Wind Scatterometer in Boreal Forest Zone*, 4-8 August 1997.

[2] Gardner Watt, "Vegetation classification using seasonal variations of scatterometer data at c-band and ku-band", Tech. Rep., 1999.

[3] D. G. Long and P. Hardin, "Vegetation studies of the amazon basin using enhanced resolution seasat scatterometer data", *IEEE Transactions on Geoscience and Remote Sensing*, vol. 32, no. 2, pp. 449–460, May 1994.

[4] *Analysis of the Canadian Boreal Forest using Enhanced Resolution ERS-1 Scatterometer Imagery*, 27-31 May 1996.

[5] D. G. Long and M. R. Drinkwater, "Greenland observed at high resolution by the Seasat-A scatterometer", *Journal of Glaciology*, vol. 32, no. 2, pp. 213–230, 1994.

[6] A. K. Fung F.T. Ulaby, R. K. Moore, *Microwave Remote Sensing - Active and Passive*, vol. 1 and 2, Artech House, 1986.

[7] F. M. Naderi, M. H. Freilich, and D. G. Long, "Spaceborne radar measurement of wind velocity over the ocean– an overview of the NSCAT scatterometer system", *Proceedings of the IEEE*, vol. 79, no. 6, pp. 850–866, June 1991.

[8] Q. P. Remund and D. G. Long, "Polar sea ice extent detection using ku-band scatterometer data", Microwave earth remote sensing technical report, Brigham Young University, 1998.

[9] Q. P. Remund and D. G. Long, "An iterative approach to multisensor sea ice classification", Microwave earth remote sensing technical report, Brigham Young University, 1999.

[10] Q. P. Remund and D. G. Long, "Optimization of sirf for nscat", Microwave Earth Remote Sensing technical report MERS Report 97-03, Brigham Young University, July 1997.

[11] D. G. Long, P. Hardin, and P. Whiting, "Resolution enhancement of spaceborne scatterometer data", *IEEE Transactions on Geoscience and Remote Sensing*, vol. 31, no. 3, pp. 700–714, May 1993.

[12] *Azimuthal Modulation of C-Band Scatterometer σ^o Over Southern Ocean Sea Ice*, July 1998.

[13] E. Matthews, "Global vegetation and land use: New high resolution data bases for climate studies", *Journal of Climatology and Applied Meteorology*, vol. 22, pp. 474–487, 1983.